Atomic-scale characterization of structural distortions in perovskite oxide thin films

Bernat Mundet Bolós

Atomic-scale characterization of structural distortions in perovskite oxide thin films

Bernat Mundet Bolós

Institut de Ciència de Materials de Barcelona (ICMAB-CSIC)
Departament de Materials Superconductors i Nanoestrucuració a Gran Escala

Supervisor:

Dr. Jaume Gázquez Alabart

Tutor

Prof. Àlvar Sánchez Moreno

A thesis submitted for the degree of
Doctor of Philosophy in Material Science

Universitat Autònoma de Barcelona
Departament de Física, Facultat de Ciències

Bellaterra, Juliol 2018

Dr. Jaume Gázquez Alabart, Investigador a l'Insitut de Ciència de Materials de Barcelona, i **Prof. Àlvar Sánchez Moreno**, Professor Titular de la Universitat Autònoma de Barcelona

CERTIFIQUEN

que en Bernat Mundet Bolos, Llicenciat en Física, ha dut a terme sota la seva direcció el treball que porta per títol **"Atomic-scale characterization of structural distortions in perovskite oxide thin films"** i queda recollit en aquesta memòria per optar al Grau de Doctor en Ciència de Materials.

I per a que així consti, signen el present certificat.

Dr. Jaume Gázquez Alabart

Prof. Àlvar Sánchez Moreno

Bellaterra, July 2018

Acknowledgements

Amb aquestes paraules vull agrair l'ajuda de tota aquella gent que d'una manera o altra ha contribuït en la realització d'aquesta tesis doctoral.

En primer lloc agrair el gran suport per part d'en Jaume i en Roger. Ha estat un plaer fer un petit equip de micròspia amb vosaltres dos durant aquests anys! A tu Jaume per confiar en mi des del primer moment i permetre que pogués aterrar al ICMAB. Evidentment també per tots els coneixements que m'has transmès, tant a nivell de ciència i de laboratori com gastronòmics, i per dirigir i corregir aquesta tesis. Però especialment, per haver sabut ser un bon amic a la vegada que el meu director. A tu Roger per haver-me ensenyat tots els secrets del TITAN i ajudar-me sempre amb tots els dubtes que m'han anat sorgint. A veure si no perdem la tradició de retrobar-nos i fer uns bons "callos" de tant en tant.

En segon lloc vull donar les gracies a la Prof. Teresa Puig i al Prof. Xavier Obradors, per donar-me la oportunitat de pertànyer al grup de Superconductors, per tots els coneixements que he pogut aprendre de vosaltres i per tot el vostre suport durant aquests 4 anys. També m'agradaria agrair l'esforç de tots els membres del grup de Superconductors amb qui he estat treballat colze a colze durant aquest període. Ha estat un gran plaer treballar amb tots vosaltres, aquesta feina és fruit també del vostre treball. En particular, vull donar les gracies a en Ferrán Vallès, Juri Banchewski, Dr. Anna Palau, Dr. Ziliang Li, Dr. Mariona Coll, Dr. Pablo Cayado, Dr. Cornelia Pop, Bohores Villarejo, Dr. Flavio Pino i Julia Jareño, ja que molts dels resultats descrits en aquesta tesis són derivats de la seva feina.

This work would have not been possible without the collaboration of other scientific experts. Particularly, I would like to express my very great gratitude to Prof. Rohan Mishra, Dr. Guangfu Luo and the PhD student Steven Hartman from the Materials, from the Institute of Materials Science and Engineering, Washington University in St. Louis, U.S.A., for their deep implication in the DFT-calculations appearing in this work. I would like

to thank Prof. Marek Wojcik and Prof. Ewa Jedryka, from the Institute of Physics, Polish Academy of Sciences, Warszawa, Poland, for the NMR experiments.

Vull agrair també tota la inesgotable ajuda del personal d'administració del ICMAB i la dels tècnics, tant del ICMAB com del ICN2. En especial a en Francisco Belarre, per ensenyar-me tots els secrets referents al procés de fabricació de mostres, per ser una font inesgotable de cafeïna i per aportar sempre bon humor i optimisme al laboratori; i al Marcos Rosado, per estar sempre disponible per ajudar-te. A tota aquella gent del ICMAB i del ICN2 amb qui no he tingut el plaer de col·laborar científicament, però sí personalment.

Mis más profundos agradecimientos a toda la gente del Laboratorio de Microscopias Avanzadas de Zaragoza, por confiar en mí y dejarme usar autónomamente sus equipos. Especial mención para César Magén, Alfonso Ibarra y Rodrigo Pacheco, puesto que siempre me han ayudado cuando han habido problemas con el Microscopio. I would also like to thank the people from the Centro Nacional de Microscopía Electrónica, in Spain, and Oak Ridge National Laboratory, in U.S.A., for allowing us to use their microscopes.

I would like to thank the Spanish Ministry of Economy and Competitiveness, the Generalitat de Catalunya and the European Union for the financial support through several research projects: "Severo Ochoa" Programme for Centres of Excellence in R&D (SEV-2015-0496), Consolider NANOSELECT (CSD 2007-00041), SENY (MAT 2011-28874-C02-01), Pla de Recerca (2009-SGR-770 & 2017-SGR-1519), European development of Superconducting Tapes (EUROTAPES,FP7-NMP-Large-2011-280432), CoachSuperenery (MAT2014-51778-C2-1-R, co-financed by the European Regional Development Fund) and "ayudas para contratos predoctorales para la formación de doctores" fellowship programme (BES-2015-072749).

Fora del mon acadèmic, vull agraïr el suport i els moments de desconnexió viscuts amb els meus amics Girers i Escaladors Guais, amb qui he compartit i comparteixo pràcticament tots els caps de setmana. A tu Ana per re-aparèixer a la meva vida i recarregar-la de bon humor, i per apuntar-te gairebé sempre

a tots els meus plans. Per fer d'aquest darrer any de tesis, que teòricament és el més feixuc, el més senzill de tots.

Finalment agrair el suport incondicional de la meva família. Xavier, Montserrat, Albert, Anna i Marc gracies per estar sempre al meu costat i fer que aquesta vida sigui més fàcil.

List of acronyms

ABF	Annular Bright-Field
AFD	Antiferrodistortive
AFM	Atomic Force Microscopy
BCO	$BaCeO_3$
BHO	$BaHrO_3$
BYTO	Ba_2YTaO_6
BZO	$BaZrO_3$
CSD	Chemical Solution Deposition
CZO	$Ce_{0.9}Zr_{0.1}O_2$
DE	Double-Exchange
EELS	Electron Energy Loss Spectroscopy
EELS-SI	Electron Energy Loss Spectroscopy-Spectrum Image
ELNES	Energy-Loss Near-Edge Structure
FEG	Field Emission Gun
FFT	Fast Fourier Transform
FH	Flash Heating
GAADS	General Area Detector Diffraction System
GPA	Geometrical Phase Analysis
HAADF	High-Angle Annular Dark-Field
LAADF	Low-Angle Annular Dark-Field
LAO	$LaAlO_3$
LSAT	$(LaAlO_3)_{0.3}(Sr_2TaAlO_6)_{0.7}$
LSMO	$La_{0.7}Sr_{0.3}MnO_3$
LNO	$LaNiO_3$
MIT	Metal-Insulator Transition
MOD	Metal-organic Decomposition
NC	Nanocomposite
NMR	Nuclear Magnetic Resonance
NNO	$NdNiO_3$
NP	Nanoparticle

PCA	Principal Component Analysis
PLD	Pulsed Laser Deposition
pn-NC	preformed nanoparticle Nanocomposite
RNO	$ReNiO_3$
RPF	Ruddlesden-Popper Fault
ss-NC	spontaneously segregated Nanocomposite
STEM	Scanning Transmission Electron Microscopy
STO	$SrTiO_3$
TMO	Transition Metal Oxides
TFA	Trifluoracetate
XRD	X-Ray Diffraction
2D-XRD	Two-dimensional X-Ray Diffraction
YBCO	$YBa_2Cu_3O_7$
YO	Y_2O_3
YSZ	Zr-stablized Y_2O_3

Contents

Chapter 1

Motivation and outline

1.1 Motivation

Transition metal oxides (TMO) are a group of crystalline materials characterized by a strong hybridization between the transition metal *d*- and oxygen *2p*-bands. [1–5]. This coordination leads to a particular electronic configuration, where electrons present three degrees of freedom (charge, spin and orbit), resulting in a sort of fascinating properties such as superconductivity [6], colossal magnetoresistivity [7, 8], ferroelectricity [9], ferromagentism [10], metal-insulator transition [11], etc. These huge range of physical properties make these materials suitable for a lot of applications in the world of electronics, spintronics, energy harvesting, memories, photovoltaics, mechanical actuators and so on.

Many TMOs present a perovskite structure with the characteristic chemical formula ABO_3. As shown in Fig.1.1 (a), the idealistic perovskite structure is cubic and belongs to the *Pm-3m* space group. Four divalent or trivalent cations (A) sit at the cube corner positions. The transition metal cation (B), placed at the body center position, is coordinated with six oxygen anions, located at the face centered positions, forming a BO_6 octahedral unit.

Those electrons lying into the transition metal five-fold degenerated *d*-orbital have five distinct wave-functions, as sketched in Fig.1.1 (b). The internal crystal field, emerging from the octahedral coordination, splits the 5-fold degenerated *d*-orbital into two new energetic bands: the 3-fold degenerated t_{2g} and the 2-fold degenerated e_g bands. As shown in Fig.1.1 (b), the wave functions belonging to the e_g orbital ($x^2 - y^2$, $z^2 - r^2$) point towards the oxygen sites and are more energetic than those belonging to the t_{2g} orbital (xy, yz and xz), which point towards the space between oxygen

sites. Besides, as these energetic levels are located close to the Fermi level, the TMO physical properties can drastically change when their electronic configuration slightly varies. This is the reason why these materials exhibit very rich and complex phase diagrams composed by several electric and magnetic phases.

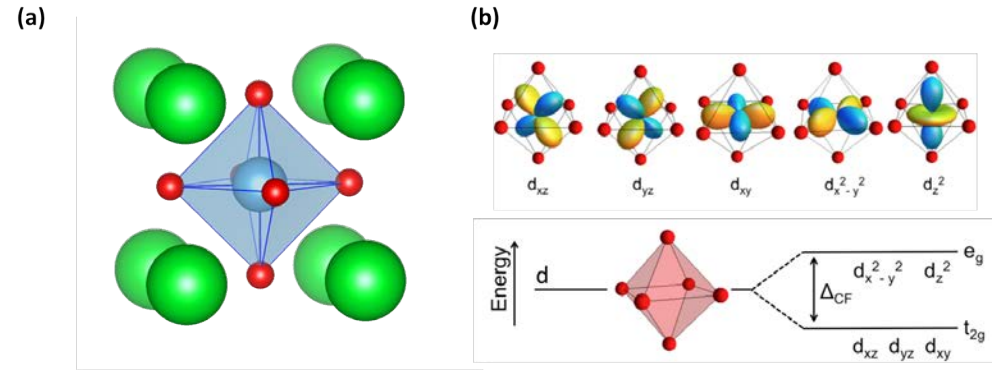

Figure 1.1: (a) Idealistic ABO_3 perovskite structure. A sites in green, B sites in blue and O anions in red. (b) Electron wave-functions associated to the transition metal d-orbital when it is octahedrally coordinated with 6 oxygens. The d-band splits into the e_g and t_{2g} bands as a result of the internal crystal field emerging from this octahedral coordination. This figure is extracted and adapted from Ref. [11].

The stability of each perovskite oxide compound can be estimated using the tolerance factor parameter (t), an empirical geometric measure of the relative ionic volume fraction, which is described as:

$$t = \frac{(r_A + r_O)}{\sqrt{2}(r_B + r_O)} \tag{1.1}$$

where r_i are the radii of the atoms present within the structure. Those perovskite oxides that have a tolerance factor value equal to 1 are predicted to have the canonic cubic perovskite structure. However, as t separates from 1, the structure starts to be instable and some structural distortions might arise, thus lowering the system symmetry. Typically, when $t < 1$, the oxygen octahedra rotate around the crystallographic axes (antiferrodistortive tilts). On the other hand, when $t > 1$, polar (or ferroelectric) distortions are predicted to occur, being the atoms shifted from its expected positions. This is what happens in

prototypical ferroelectric oxides as $BaTiO_3$ or $PbTiO_3$. The physical properties of perovskite oxides are observed to be very sensitive to these structural distortions, thus modifying or generating new electric and magnetic behaviors such as metal-insulator transitions, ferromagnetism, ferroelectricity, etc. Moreover, the intrinsic properties of each TMO compound can be tailored by distorting the BO_6 unit in purpose, which can be achieved by applying external fields or hydrostatic pressures, changing the oxygen concentration, straining the material, or by many other strategies. This opens a wide playground towards the fabrication of novel oxide-based materials and heterostructures that offer a wide-range of tunable properties.

In this thesis we have studied three paradigmatic examples of structural distortions that are driven by the strain. Besides, each strain-relief mechanism have been generated within different perovskite oxides, which have been grown as epitaxial films following a chemical solution deposition (CSD) methodology. This fabrication process constitutes a low-cost, versatile and easily scalable method to the fabrication of high quality epitaxial oxide-based heterostructures. In an attempt to build bridges between the atomic and macroscopic worlds, we have also tried to correlate the observed structural modifications with the changes of the film physical properties. First, we have analyzed the challenging microstructure of $YBa_2Cu_3O_7$ (YBCO) nanocomposite films, containing randomly oriented and homogeneously dispersed nanoparticles that are trapped within the YBCO host matrix. Second, we have investigated the effect of imposing a biaxial strain (either tensile- or compressive-strain) in $LaNiO_3$ (LNO) and $NdNiO_3$ (NNO) films by growing them onto different single crystal substrates. Finally, we have addressed the effect of reducing the film thickness of biaxially strained $La_{0.7}Sr_{0.3}MnO_3$ (LSMO) films down to few nanometers.

We have exploited the analytical capabilities offered by the aberration-corrected scanning transmission electron microscopy (STEM), in combination with the electron energy lost spectroscopy (EELS), to characterize the structure and chemistry of the fabricated films. We have used STEM-EELS to challenge our investigation as it is a very versatile and powerful technique that enables to locally probe the atomic structure (image), chemistry and electronic configuration (EELS) of any crystalline material in the real space

with subatomic resolution [12].

1.2 Thesis outline

This thesis is divided into six separated chapters. This first chapter introduces the importance of the studied materials and the motivation of the thesis. The second chapter is a brief description of all the experimental techniques that have been used in this work, taking special attention to the basics of the STEM-EELS technique and to the used post-processing tools for the image processing as well. Three chapters describe the obtained results, which are classified as a function of the studied material. Finally, we wrap up our results with a summary of the performed work and its main derived conclusions. Two final annexes encloses this manuscript. The first one contains a detailed explanation about the calculation of the density of strained areas in YBCO. In the second one, it is enumerated all the published publications, conference contributions and workshops/summer schools attendances that are derived from this work during these four years as a PhD student.

The three chapters that describe the obtained results are briefly summarized below:

In **Chapter 3** we have studied the challenging microstructure of YBCO thin films, which is one of the superconducting materials with a largest critical temperature. The performance of this compound is strongly linked to its capacity to pin quantized magnetic vortices, which like to remain within the nanosized and non-superconucting areas such as crystalline defects. Therefore, it is mandatory to correlate the superconducting properties, measured in each film, with its corresponding YBCO defect landscape, to be then capable of engineering the optimal YBCO microstructure that offers the best performances. This chapter is divided into two blocks, each one comprising different scales. In the first part, we have investigated how the defect landscape of YBCO nanocomposite films varies when oxide-based nanoparticles (NPs) are introduced within the YBCO host matrix following different approaches. In the second block, we have moved towards the atomic-scale by investigating

all the emerging distortions around the most common defect found in YBCO nanocomposites, the Y124 intergrowth.

In **Chapter 4** we have investigated how the $LaNiO_3$ (LNO) and $NdNiO_3$ (NNO) thin films accommodate the strain imposed by different single crystal substrates. $RENiO_3$ compounds, where RE refers to a rare-earth element, have been widely studied during the last decades as they exhibit a tunable metal-insulator transition and a resistive-switching behavior that make them very promising as elements for adaptive electronics. However, it still remains unclear which structural distortions are responsible of the change on their physical properties and how these compounds accommodate the epitaxial strain. In this chapter we have given new insights into the strain accommodation mechanisms arising at both tensile- and compressive-strained LNO and NNO films, grown onto $LaAlO_3$ (compressive) or LSAT (tensile) single crystal substrates, and into the structural distortions emerging around the generated defects as well.

In **Chapter 5** we have evaluated $La_{0.7}Sr_{0.3}MnO_3$ (LSMO) thin film samples with different nominal thicknesses. Our samples transit from a ferromagnetic-metallic behavior, typically observed in bulk LSMO crystals, towards a ferromagnetic-insulating regime when the film thickness is reduced down to two nanometers. The appearance of this insulating-ferromagnetic behavior is very interesting as it contradicts the double-exchange transport mechanism that governs the electrical conduction in LSMO. We investigate the structural modifications occurring within our LSMO films due to the strain (substrate structure) and spatial confinement (film thickness) effects, which might explain the observed changes in their physical properties.

Chapter 2

Experimental methodologies

This chapter is devoted to briefly describe all the experimental methodologies that have been used in this thesis for the growth and characterization of the studied epitaxial films. Mainly, we have used the scanning transmission electron microscope in combination with the Electron Energy Loss Spectrometer (STEM-EELS) in order to have access into the atomic, chemical and electronic structure at specific crystal positions of the studied films. Here, we describe the fundamental aspects behind this technology that are needed to understand the results that are herein described. Further information about the STEM-EELS technique can be obtained from references [12–16].

2.1 Aberration-corrected Transmission Electron Microscope

Among all the available techniques and equipments that are used to characterize crystalline materials, STEM-EELS stands out as a very versatile and powerful approach because it allows to directly visualize the atomic structure of crystals in real space with sub-atomic resolution. Besides, these microscopes allows the simultaneous acquisition of complementary signals from the same crystal position, thus providing structural (imaging), chemical and electronic information (EELS) from specific crystallographic sites. In the scope of our investigation, we consider that STEM-EELS is the most appropriate technique to study the structural modifications arising around the non-periodical structures, such as point defects or interfaces, as it permits to obtain incoherent images directly in the real space, which avoids the appearance of image artifacts generated by changes in the electron beam phase [12, 14]. Fig. 2.1 shows an schematic illustration of the STEM.

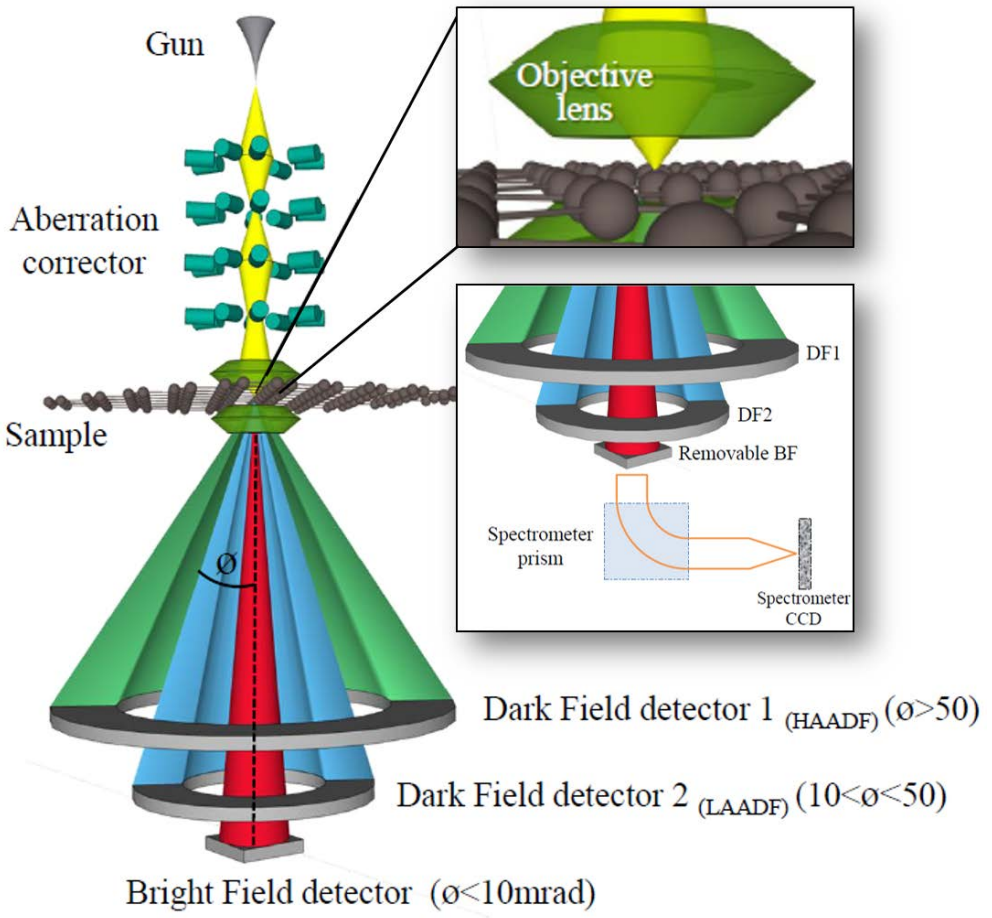

Figure 2.1: Illustration of the STEM. The insets show sketches of the electron probe and the EEL spectrometer set-up.

The main idea behind an electron microscope is to take profit of the lower wavelength of highly accelerated electrons (60-300 KeV) to reduce as much as possible the Rayleigh resolution limitation. In the STEM configuration, an electron beam is extracted from an electron gun, which is then focused into the crystal sample by the use of electromagnetic coils. The image resolution depends on the electron probe diameter, which can be reduced down to hun-

dreds of picometers when the electron beam aberrations are cleaned with the use of an aberration-corrector [17, 18]. The aberration corrector is composed by a set of multipole lenses that generate additional magnetic fields whose strength varies with the off-axis position. Thanks to that, all the electrons are focused at the very same focal plane independently of its traveling path.

Once the tinny electron probe impinge into the crystal sample, the electrons interact with the crystal atoms and their associated fields, being scattered at different angles while crossing the sample specimen. All the transmitted electrons are gathered by either the use of a circular or annular detectors, each one providing complementary information. Besides, an EEL spectrometer can be placed within the central position of the column, thus collecting those electrons that have lost some energy as a result of scattering inelastically with the sample, which are typically deviated at low angles. This spectrometer is composed by an electromagnetic prism that classify each electron as a function of its kinetic energy and a Charge Couple Device (CCD) camera that records the resulting spectrum, which contains information about the chemistry and electronic configuration from where the electron probe is sitting. The STEM images are formed by scanning the electron beam through a crystal region, thus obtaining complementary signals from each specific probe position (or image pixels). The imaging modes that have been used in this thesis are briefly described below.

2.1.1 Z-contrast or High-Angle Annular Dark-Field imaging mode

The High-Angle Annular Dark-Field (HAADF) imaging mode raised the popularity of this technology as it is the only approach that performs incoherent imaging at the atomic scale, making the image interpretation straightforward without the need of simulations. This property is of particular interest for the study of non-periodic structures such as defects or interfaces. The incoherent imaging is achieved by using an annular detector with very large inner and outer angles (100-200 mrad), this is the HAADF detector (DF1 in Fig. 2.1), which collect those electrons undergoing Rutherford scattering with the atomic nuclei of the crystal. Besides, the brightness of each atomic column barely scales with

the Z^2 (atomic number) in this kind of images, being this imaging mode also referred to as Z-contrast mode [14]. Fig. 2.2 displays a Z-contrast image of the $YBa_2Cu_3O_7$ (YBCO) crystal structure when it is viewed along the <100> zone axis.

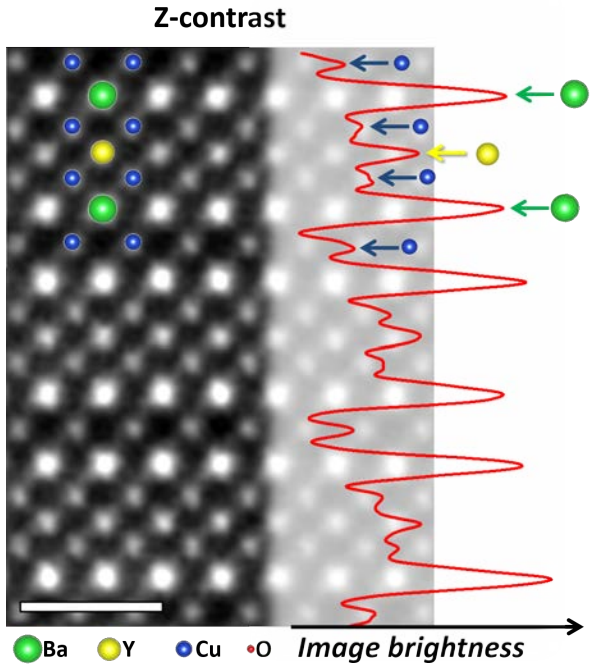

Figure 2.2: High magnification Z-contrast image of a YBCO crystal, viewed along the <100> zone axis. The superimposed red line represents the averaged intensity depth-profile of the image. The Ba, Y and Cu cations are represented with green, yellow and blue circles. Scale bar: 1 nm

The heavier cations (Ba, Y and Cu) are directly distinguished, without the need of spectroscopic techniques, by simply looking at the brightness of each atomic column. Thanks to the Z-contrast property, the brightest columns correspond to Ba cations (green circles), followed by the Y ones (yellow circles) and finally by the Cu ones (blue circles). This is further confirmed when we trace an intensity profile along the c-axis direction, which is displayed as a red line that is superimposed onto the Z-contrast image of Fig. 2.2.

The main drawback of this imaging mode is that light elements can not be imaged when they are located close to heavier atoms, as it occurs in the oxide materials that are studied in this thesis.

2.1.2 Low-Angle Annular Dark-Field imaging mode

The Low Angle Annular Dark Field (LAADF) mode (DF2 in Fig. 2.1) is performed by using an annular detector with lower inner and outer collecting angles. Even though LAADF images are not purely incoherent, their pixel brightness still scales with Z. However, the lower inner angle enables to collect those electrons deviated at lower angles due to the dechanneling effects generated by the distortions of the crystal lattice. This particularity permits to better identify the nanoscale lattice deformations within the studied crystals [19–22]. An illustrative example is shown in Fig. 2.3 (a) and (b) where a HAADF and LAADF images of a YBCO crystal region containing a planar defect are displayed, respectively.

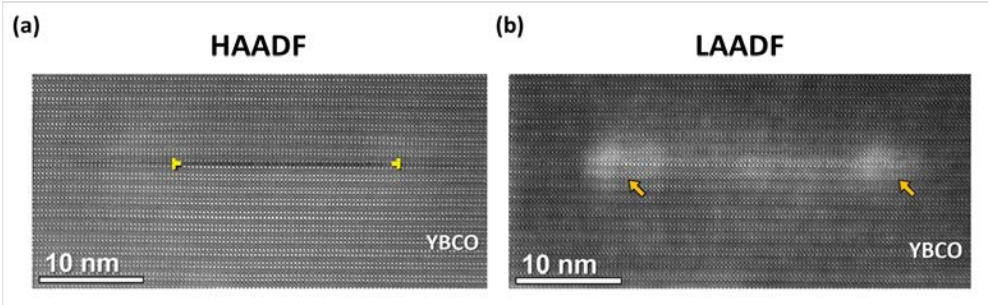

Figure 2.3: (a) HAADF and (b) LAADF images of a YBCO crystal region containing a planar defect. Crosses and arrows point to the edges of this defect. These figures are extracted from Ref. [22].

A contrast enhancement is identified around the edges of the planar defect (orange arrows) in the LAADF image, see Fig. 2.3 (b), which is attributed to the appearance of strain fields.

2.1.3 Annular Bright Field imaging mode

The main drawback of the Z-contrast imaging mode is that the heavier and lighter elements can not be imaged together. However, the use of an Annular Bright Field (ABF) detector permits to image all the atomic sub-lattices that are present within any crystal structure [23, 24]. A simplified version of how the ABF images are generated is that, those electrons interacting with the oxygen columns cross the central detector hole because of the channeling effects. On the other hand, those electrons that are scattered at the heavier atomic columns

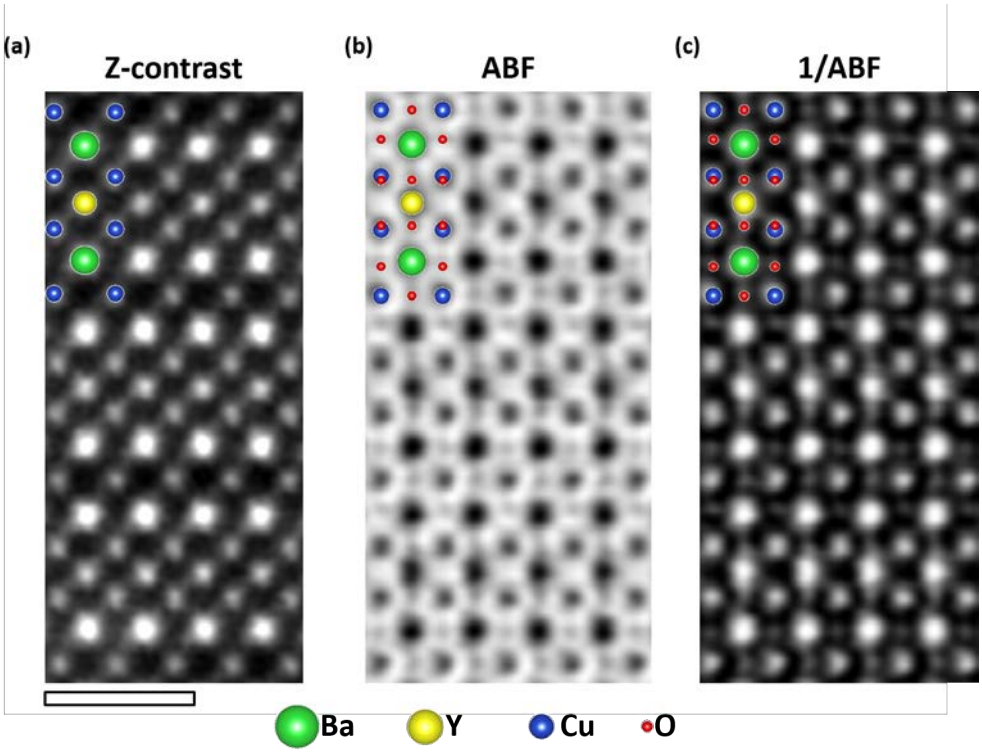

Figure 2.4: (a) Z-contrast, (b) ABF and (c) contrast-inverted ABF images of a YBCO crystal area viewed along the <100> zone-axis. The atomic columns are viewed as dark spots surrounded by a bright background in the ABF images. Ba, Y, Cu and O atoms are represented with green, yellow, blue and red circles, respectively. Scale bar: 1 nm.

are also excluded, as they are deviated at larger angles. When the electron probe is sitting at the void, the ABF detector collects the transmitted cone beam. The ABF images are coherent, thus presenting reversal-contrast features when the phase of the electron probe changes. Therefore, the viewed contrast features might not represent the real crystal structure, which leads to the need of theoretical simulations in some cases. Fig. 2.4 (a) and (b) show a Z-contrast and ABF images, respectively, of a YBCO crystal region viewed along the [100] direction as zone axis. Notice that if we invert the contrast of the ABF image, see Fig. 2.4 (c), the atomic columns appear as bright dots surrounded by a dark environment, as in the Z-contrast images. Although the image brightness of the contrast-inverted ABF image, the one shown in Fig. 2.4 (c), does not scale with Z, the oxygen sub-lattice can be clearly identified (red circles) there.

2.1.4 Electron Energy Lost Spectroscopy

Electrons also undergo inelastic scattering while traveling through the crystal specimen. These electrons loose some of their kinetic energy as they

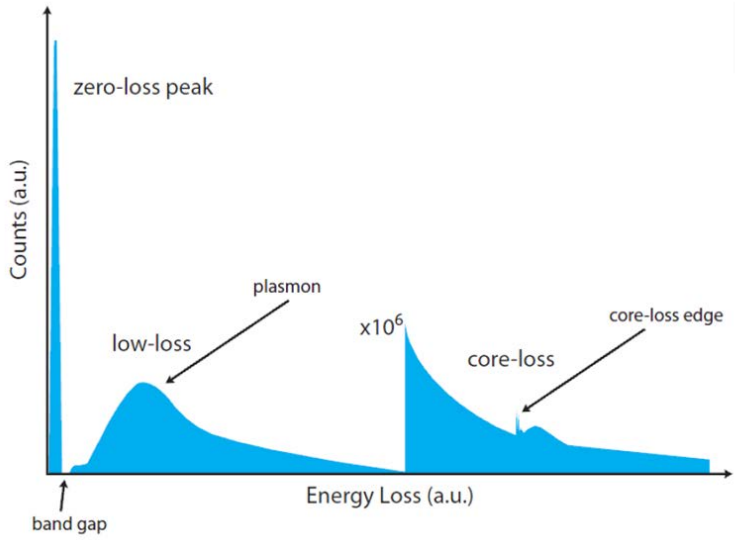

Figure 2.5: Illustration of an EEL spectrum example. Figure extracted from [25].

excite the less bonded crystal electrons towards the available energetic levels. By using the EEL spectrometer we are able to classify the transmitted electrons as a function of their kinetic energy [15]. Fig. 2.5 displays an schematic view of the EEL spectrum.

The zero-loss peak is the most intense signal of the spectrum and corresponds to those electrons that preserve their initial kinetic energy. The lower energetic spectrum region (low-loss) contains information about the

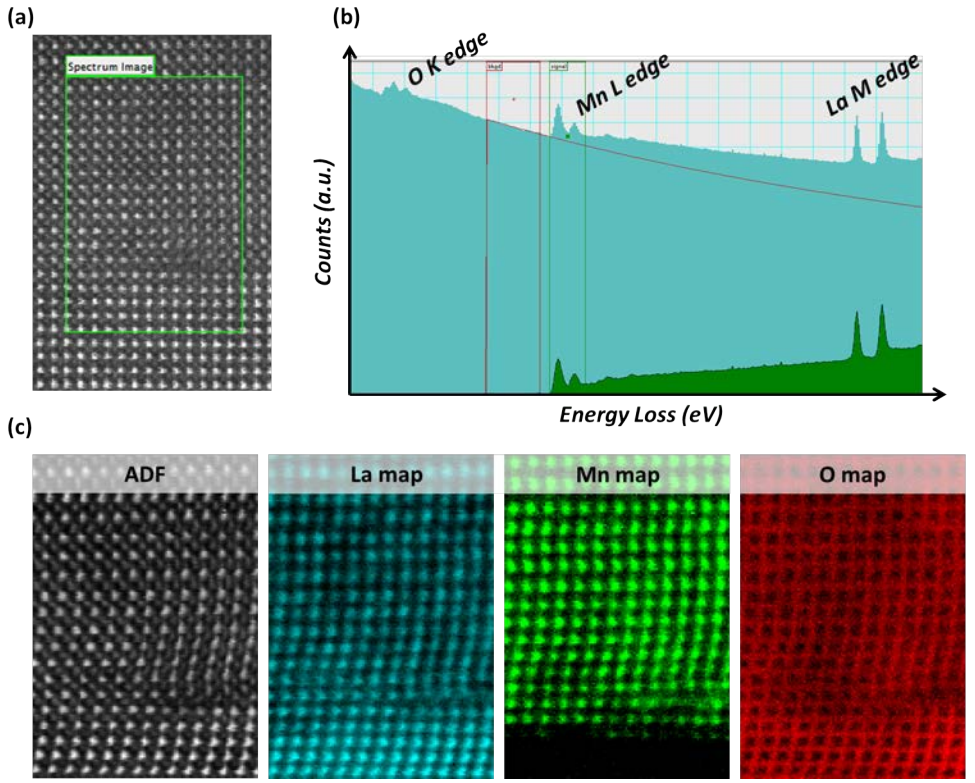

Figure 2.6: (a) Z-contrast image of a LAO/LSMO heterostructure with the green squared region from where an EELS-SI has been acquired. (b) EEL spectrum obtained from one pixel of the ADF simultaneous image shown in (c). (c) From left to right it is displayed the ADF simultaneous image and the La, Mn and O compositional maps.

less-energetic interactions, such as plasmonic oscillations or optical absorption properties, while the core-loss region provides information about the highest-energy electron excitations from the valence to the conduction bands. As electrons can transit towards a plenty amount of available levels, the spectral features located in this region are not Gaussian peaks but edges with particular geometries that are extended through hundreds of eV. The characteristic geometry of the STEM enables to acquire an EEL spectrum at each image pixel, thus obtaining a 3D-dataset referred to as EELS-spectrum image (EELS-SI). This allows to map the spectral variations appearing within different crystallographic positions and then correlate these spectral changes with modifications of either the chemical structure or electronic configuration, as shown in Fig. 2.6.

Fig. 2.6 (a) is a Z-contrast image of a LSMO film grown onto a LAO single crystal substrate. The image contains a green squared region from where the EELS-SI is acquired. A representative EEL spectrum of this region is displayed in Fig. 2.6 (b). The obtained ADF simultaneous image of the 3D dataset (EELS-SI) from this region is shown in the left-side of Fig. 2.6 (c), where each image pixel contains an EEL spectrum. By integrating the EEL spectrum signal beneath the La M, Mn L and O K edges, we can map the elemental composition of the imaged region, as shown in the blue (La), green (Mn) and red (O) compositional maps, respectively. In each case, the background signal have to be subtracted by fitting a power law dependency the EEL spectrum before each particular edge.

Principal component analysis

Most of the EEL spectra that have been analyzed in this work have been filtered using the Principal Component Analysis (PCA) script for Digital Micrograph, written by Masashi Watanabe [26], in order to reduce as maximum as possible the statistical noise associated to the experimental measurement. It consists of a multivariate statistical analysis [27] that evaluates the EELS-SI dataset, giving a weight to each appearing spectral feature. PCA decomposes the whole EELS-SI dataset into a number of components that describe the original data without losing significant information. This is accomplished by generating a two-dimensional matrix where all the image pixels are settled in

the matrix columns and the rows represent the appearing uncorrelated spectral features. The principal components are obtained by multiplying each row and column.

After running the PCA, the principal components are plotted as a function of their statistical variance, being the relevant components placed close to the origin whereas the ones associated to the statistical noise appearing in a straight line at the end of the plot. Finally, the EELS-SI can be re-generated by only using those components containing the relevant information, and excluding those ones related to the spectral noise, which substantially improves the signal-to-noise ratio of the spectra.

2.1.5 Microscopes used in this thesis

The STEM images presented in this work were acquired by using a *FEI Titan* (60-300 kV), equipped with a third order probe-aberration corrector, a monochromator and an X-field emission gun (FEG), located at the *Laboratorio de Microscopías Avanzadas, Instituto de Nanociencia de Aragón, Universidad de Zaragoza*. Two *Nion UltraSTEM* microscopes, one operated at 100 KV and the other one at 200 KV and both equipped with a fifth-order Nion probe-aberration corrector and a cold-FEG emission gun, from the *Materials Science and Technology Division, Oak Ridge National Laboratory, Oak Ridge, USA* was also employed. The microscopes are equipped with a Gatan Enfina and a Gatan Enfinium spectrometers, respectively. A JEOL JEM ARM200CF microscope, operated at 200 KV and equipped with a cFEG emission gun, a *Gatan Quantum* EEL spectrometer and a CEOS spherical aberration corrector, located at the*ICTS Centro nacional de microscopía electronica, Universidad Complutense de Madrid* was also used.

2.2 Specimen preparation

A sample preparation process has to be carried out in the samples under study in order to thin them enough for being almost transparent to the electron beam. Typically, the thickness of a TEM specimen has to be lower than 100 nm. This process is extremely delicate, specially in hard and brittle materials as it is the case of ceramic materials. In this work, we have used two

distinct preparation processes: by polishing them mechanically with the use of mechanical and ionic polishers or by extracting a lamella by the use of a *Focused Ion Beam* (FIB) equipment. Without taking into account the costs associated to each preparation process, those samples prepared manually have a larger observable area, which is randomly selected, than those prepared with the FIB. On the contrary, the FIB permits to precisely select the area under study. Another advantage offered by the FIB is that the specimens tend to have a smoother thickness gradient than those prepared mechanically, which is very useful for those samples having thicker films ($\approx 1\mu m$). Both processes are briefly described in the following text.

2.2.1 Mechanical processes

Depending on the sample orientation (cross sectional or planar view), different fabrication steps have to be carried out:

- **Cross sectional view:** First, we have to cut the sample into two parts by using a diamond wire saw. Then, both pieces are glued one in top of the other (like a sandwich) with the films' surface looking at each other. Second, we make cross sectional and parallel cuts to divide the sample into several small pieces. The orientation of these cuts depend on the desired zone-axis direction that will be used for the sample characterization. Both lateral faces (the ones having the film interface in the middle) of one of these pieces are polished separately by the use of a *Multiprep polishing system of Allied* and polymer disks that have incorporated some diamond grains. In order to minimize the surface roughness, we have to progressively reduce the grain-size of the diamonds that are present in the disks. This step ends when both lateral faces are flat enough and the TEM specimen has an approximate thickness of 20 μm. Finally, a ion polishing process is carried out by the use of the *Precise Ion Polishing System of Gatan, Inc.* (PIPS). In this process, the sample is loaded within a vacuum chamber and it is milled with charged ions that impinge onto both lateral faces simultaneously. The process ends when a tinny hole is formed at the sandwich interface, being the edges of the hole thin enough for the electron beam.

- **Planar view:** First, we divide the sample into squared small pieces with the diamond wire saw. The substrate surface of one of these pieces is polished, by using the *Multiprep polishing system* and the polymer diamond grinding disks, until the specimen has an approximate thickness of 20 μm. Then, we protect the film surface with a glass layer and we use the PIPS to mill the substrate surface with charged ions. In this set-up, the ions only impinge onto the substrate surface, as both ion guns are placed above it. The process ends when several small holes are created in the sample.

2.2.2 FIB lamella

Similarly than in the STEM microscope, the sample surface is scanned with an electron probe in a FIB equipment. However, the images are formed by collecting the reflected electrons instead of the transmitted ones. In the FIB, the samples are loaded within a high-vacuum chamber that contains several ion guns, ion evaporators and a platinum probe. All of these accessories permit to etch and deposit material and therefore build complex nanostructures. This is of great interest for the preparation of TEM specimens, as the FIB can be used to extract a lamella from a specific position of the sample.

In order to do so, we firstly deposit a squared-like protective layer of Pt onto the sample surface region that we want to study. Second, we etch both sides of the square, making two trenches, and the underlying crystal substrate forming a bridge. Afterwards, we cut one of its lateral edges and we glue the Pt probe, with the deposition of Pt, onto the remaining contact. Then, we cut this bridge connection and we transfer the lamella from the sample to a special holder, where it is glued by the deposition of Pt. Finally, the edge of this Pt probe is cut and both lateral faces of the lamella are thinned by the use of charged ions. The process ends when the specimen thickness is thin enough or when the Pt protective layer is fully destroyed.

2.3 Advanced imaging techniques

The changes on the physical properties of perovskite oxides are strongly influenced by the structural modifications occurring at their unit cell structure. For this reason, we have to study in detail those distortions appearing in the crystal structure of our films. This is evaluated by analyzing the obtained images with specific softwares and scripts that enables us to extract this kind of structural information. The data presented in this thesis has been processed using the *Digital Micrograph* software from *Gatan, Inc.* , which is the most common software that is used for analyzing the TEM images. Digital Micrograph also permits to install or program customized scripts to further extract a particular information from the images. In this thesis, we have used two scripts to evaluate the structural deformations occurring in our films. For low magnification images, we have used the *Geometrical Phase Analysis* (GPA) plug-in to map the unit cell deformations of the crystals. In addition, a center-of-mass refinement method has been also used to study distinct structural features such as octahedral tilts, oxygen-metal spacings or atomic shifts. This script is used to identify the central position of all the atomic columns that are present in a STEM image.

2.3.1 Geometrical Phase Analysis

The GPA permits to obtain the cell deformation maps from a low magnification image. In particular, this script maps how a particular Bragg reflection, selected from the Fast-Fourier Transform (FFT) pattern associated to each image, varies through the image. Two specific Bragg reflections are selected by using aperture masks in the image FFT pattern, as shown in Fig. 4.12 (a). The position and diameter of the used apertures are further edited by using the GPA panel that is displayed in Fig. 4.12 (b). Once the aperture settings are defined, the software calculates the strain tensor matrix at each image pixel, taking a strain-free area as a reference, which are displayed as colored maps (depicted with a temperature scale). Fig. 4.12 (d) and (e) show an example of the obtained in-plane (e_{xx}) and out-of-plane (e_{yy}) deformation maps, calculated from the Z-contrast image of a LAO/NNO heterostructure displayed in Fig. 4.12 (d).

The observed color changes in the e_{xx} or e_{yy} maps represent an enlarge-

ment (hot colors) or shrinkage (cold colors) of the in-plane or out-of-plane cell parameters, respectively, respect the reference substrate crystal. In this case, no color depth-wise variations are observed within the e_{xx} map, signaling a compression of the in-plane NNO parameter. On the other hand, the region of the e_{yy} map associated to the NNO film become red, which indicates that the out-of-plane parameter is larger in the NNO film than in the LAO substrate. The slight green and red fringes observed in both maps within the substrate region are generated by the statistical error, which fluctuates between $\pm 0.5\%$.

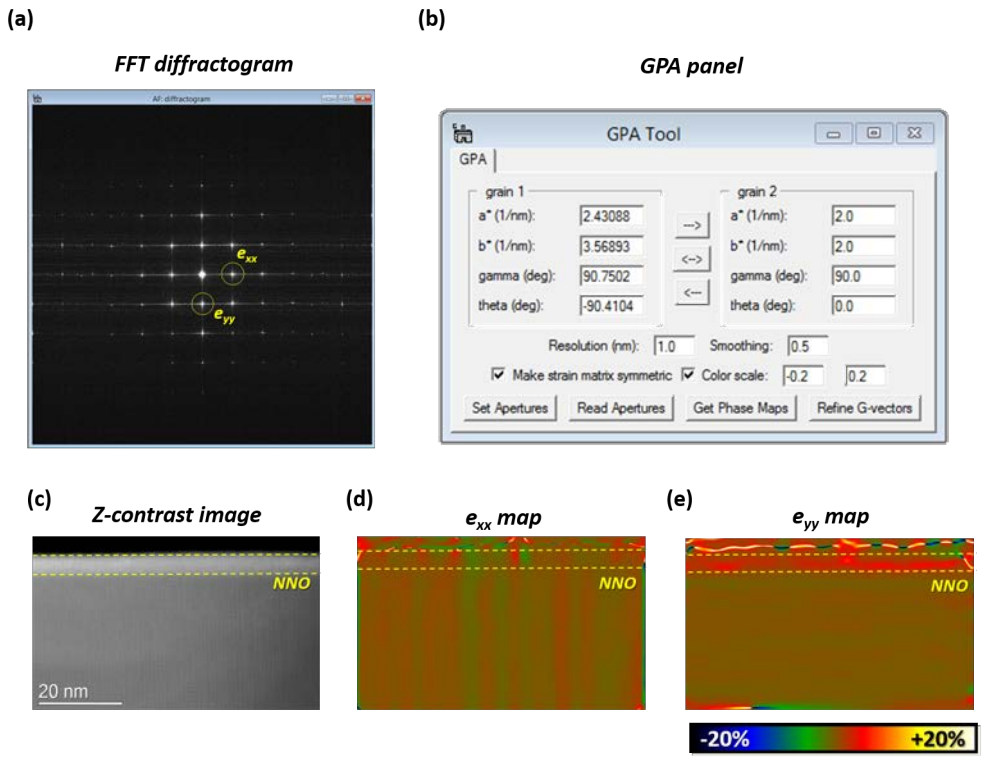

Figure 2.7: GPA analysis software. (a) FFT diffractogram with the two apertures (yellow circles). (b) GPA panel where the aperture settings are configured. (c) Z-contrast image of a LAO/NNO heterostructure. (d) e_{xx} and (e) e_{yy} deformation maps.

2.3.2 Atomic column identification

The low amount of unit cells that are viewed in high resolution images increases the uncertainty of the GPA maps. For this reason, other scripts that work directly in the real space are preferred for tracing the structural distortions of the crystal lattice in this kind of images.

In this thesis, we have used an iterative routine, written by *Dr. Andy Lupini* from the *Oak Ridge National Laboratory*, that identifies the center-of-mass position of all the imaged atomic columns. After getting a set of coordinates associated to each atomic sub-lattice, we can directly calculate any interatomic spacing or atomic shift that are present within our images. Depending on the image quality, some FFT mask filters have to be priorly applied to reduce the image noise and facilitate the identification of the central positions. This center-of-mass script works in the following manner:

- First, we have to select the atomic columns that are located at the vertices of a squared region. A first mesh of coordinates is generated by indicating the amount of atomic rows and columns that are present within the squared region.

- Second, the coordinates of each atomic column are re-adjusted by using a refinement iterative process. In particular, at each iteration, the coordinates of an individual column $(x, y)_i$ are re-calculated following the next formula:

$$(x, y)_i = \frac{(\sum_{j=i-r}^{i+r} x_j I_j, \sum_{j=i-r}^{i+r} y_j I_j)}{\sum_{j=i-r}^{i+r} I_j}. \tag{2.1}$$

  where (I_i) is the intensity of the pixel located at the $(x,y)_i$ image position. This summation includes all the pixels that are present within a circle centered at the atomic position $(x,y)_i$ with a fixed radius (r) that is defined by the user.

- This iteration is repeated several times until all the coordinates of a specific atomic sub-lattice converge into their corresponding central positions. The radius value has to be progressively decreased in order to minimize the error of the calculation.

- Once we get a set of coordinates for each atomic sub-lattice, we can map any desired structural information such as interatomic spacings or atomic shifts. It is worth including a reference area, such as the crystal substrate, within the set of coordinates for calibration purposes.

Fig. 2.8 (a) shows a high magnification contrast-inverted ABF image of a 3 unit-cell-thick LSMO film. The La, Mn and O atomic columns are sketched with green, blue and red circles, respectively. The coordinates of the Mn and O sub-lattices are identified by using the described center-of-mass refinement process. The central positions of the Mn and O atomic columns that are viewed in Fig. 2.8 (a) are superimposed with red and blue crosses in Fig. 2.8 (b), respectively.

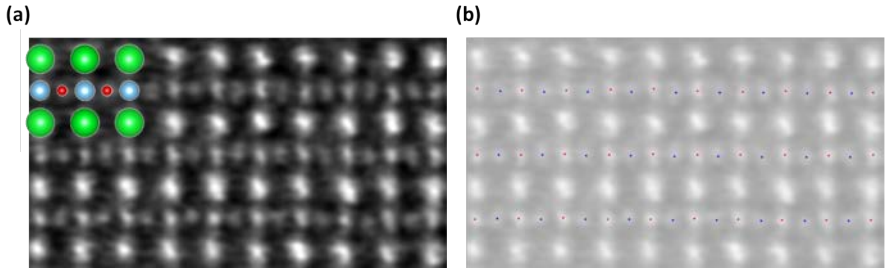

Figure 2.8: (a) Contrast-inverted ABF image of a LSMO film. La, Mn and O atoms are represented with green, blue and red circles, respectively. (b) The calculated coordinates of the Mn and O sub-lattices are drawn with red and blue crosses, respectively, onto the previously contrast-inverted ABF image.

2.4 Chemical-solution deposition fabrication process

All the studied samples in this thesis have been fabricated following a chemical-solution deposition (CSD) approach. This fabrication process stands out as a very versatile, low-cost and fast growing route towards the fabrication of high-quality oxide-based epitaxial heterostructures. Besides, it is a competitive and alternative route to those techniques that require high-vacuum chambers, which have associated high fabrication costs.

The CSD fabrication process starts from a solution composed by the

precursor metallorganic salts that are dissolved within an organic solvent. A portion of this solution is deposited onto a single crystal substrate following a spin-coating process. This deposition method consist of holding the sample onto a rotatory hot-plate evaporator that turns at a specific temperature. The solution is pushed out during this spin coating process, while some of the organics are evaporated. The rheological properties of the used solutions have to be controlled to ensure a homogeneous solution deposition and a good control on the film thicknesses. The solution viscosity is determined by a *HAAKE RheoStress R600 rheometer* from *Thermo Electron Corporation* and the surface tension and contact angles are measured with a *DSA 100 analyzer* from *KÜSS*. Fig. 2.9 shows a representative image of the surface tension set-up and a cross sectional view of one droplet of the RNO precursor solution. In this particular case, the contact angle is observed to be very low, $\theta \approx 9°$, meaning that the solution has a good wettability onto the used substrate. In addition, an interfacial tension (IFT) value of 31.4 mN/m and a viscosity of $2.9 \cdot 10^{-3}$ mPa·s were obtained, being these values acceptable for a spin coating deposition.

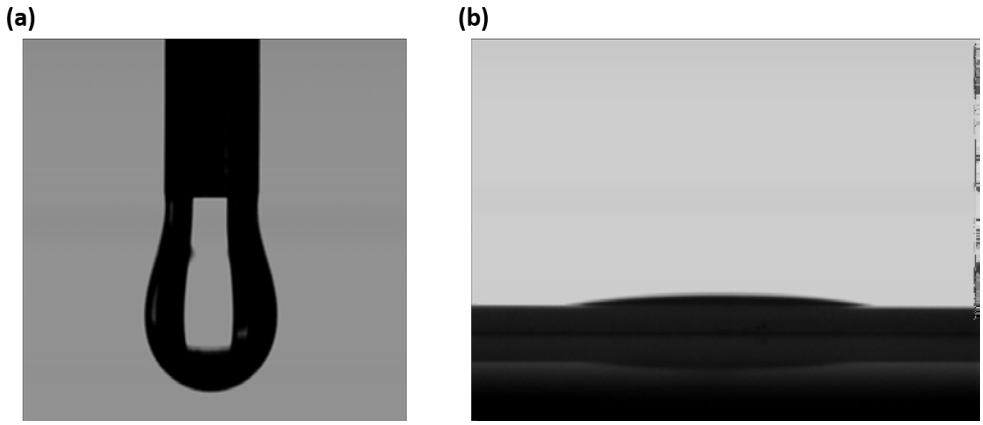

Figure 2.9: (a) Surface tension set-up. (b) Cross sectional view of a precursor solution droplet

A homogeneous and porous sol-gel phase is formed at the end of this stage. Afterwards, the remaining phases are loaded into a tubular furnace that has

controlled temperature, pressure and gas flow conditions. Samples undergo specific heat and pressure treatments that evaporate all the remaining organic precursors while the film crystal nucleates and grows with the desired texture.

The specific growing conditions of each studied compound (YBCO, RNO and LSMO) are described at the introduction section of each chapter. YBCO samples were fabricated by the Dr. Pablo Cayado and the PhD student Ziliang Li, both supervised by the Dr. Mariona Coll and by the Dr. Cornelia Pop and the PhD student Bohores Villarejo. The RNO films were fabricated by the PhD student Julia Jareño, supervised by the Prof. Teresa Puig. The LSMO films were fabricated by the Dr. Jone Zabaleta and the Dr. Mariona Coll.

2.5 X-ray diffraction

X-ray diffraction techniques are widely used in the material science community for the characterization of crystalline materials, as they provide precise information about their characteristic interatomic spacings. When a coherent and monochromatic X-ray Bloch wave impinges onto a crystalline sample, with an incident angle θ respect the normal vector of the surface, a fraction of the X-rays undergo elastic scattering at each crystal plane, being them reflected without modifying the initial wavelength λ. All the reflected X-rays beams interfere between them, presenting a constructive interference those beams going through equivalent paths, which accomplish the well-known Bragg formula:

$$n\lambda = 2d_{hkl}sin2\theta \tag{2.2}$$

where (hkl) are the reciprocal vectors of a specific crystallographic family planes, d_{hkl} is their characteristic interplanar spacing and n is the order of reflection. The X-ray beam only diffracts with those family planes whose normal vector is bisecting the angle between the incident and the scattered beam. The number, disposition and intensity of the obtained Bragg peaks (or reflections) in a diffraction pattern depend primarily on the symmetry and size of the unit cell, the arrangement of the atoms within it and the nature and wavelength of the used radiation.

The conventional $\theta/2\theta$ X-ray diffraction measurements have been performed in a *Rigaku Rotaflex RU-200BV* with Cu K radiation (λ=1.5418 Å) located at ICMAB. As this experimental set-up only detects those crystal planes that are oriented parallel to the sample surface ($\chi = 0°$), we have also used the two-dimensional X-ray diffraction (2D-XRD) configuration in order to further evaluate the crystal textures, as it provides an additional dimension to the measurement.

2.5.1 2D-X-ray diffraction: GAADS

The 2D-XRD diffraction experiments have been carried out by using a *Bruker-AXS D8 Advance*, located at ICMAB, which can be operated with Cu K radiation (λ_1=1.5406 Å and λ_2=1.5444 Å). The diffractometer is provided by a *General Area Detector Diffraction System* (GADDS). From now on, this diffractometer will be referred to as GADDS, which operates at 40 kV and 40 mA.

The GADDS diffractometer is composed by four circles, being one of them used as a sample holder and the other three to orient it. The incident X-ray beam lies along the rotation axis of the diffraction cone. The whole apex angle of the cone is twice the 2θ value given by the Bragg law. For a flat 2D detector, the detection surface can be considered as a plane, which intersects the diffraction cone forming a conic section, which is named diffraction ring. Thanks to the use of a large range of 2θ ($\Delta\theta = 30°$) and χ ($\Delta\chi = 70°$) angles, the 2D-XRD pattern contains information about those crystallographic planes oriented parallel and non-parallel to the sample surface. Thanks to that, the 2D-XRD is specially indicated for samples containing both textured and randomly oriented phases. Fig. 2.10 shows a 2D-XRD pattern extracted from a c-axis textured $YBa_2Cu_3O_7$ (YBCO) epitaxial film, which contains randomly oriented Ba_2YTaO_6 (BYTO) nanoparticles, grown onto a $LaAlO_3$ (LAO) single crystal substrate.

Due to the YBCO c-axis texture, only the $(00l)_{YBCO}$ and $(00l)_{LAO}$ reflections are identified, which appear as dot-like shaped features centered at $\chi = 0$. On the contrary, the $(220)_{BYTO}$ reflection is detected as a ring-shaped signal, which covers all the range of measured χ values. This ring-shaped signal

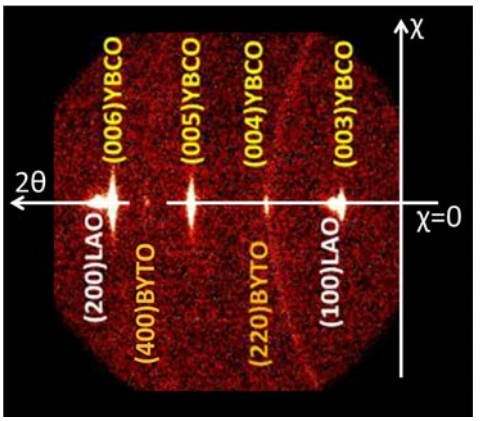

Figure 2.10: 2D-XRD pattern of a YBCO epitaxial film, which contains randomly oriented BYTO nanoparticles, grown onto a LAO single crystal substrate.

indicates that there is not a preferred orientation for the BYTO anoparticles, being most of them randomly oriented respect the YBCO matrix. However, a slight dot-like shaped signal is also identified between the $(005)_{YBCO}$ and $(006)_{YBCO}$ reflections, which is associated to the $(400)_{BYTO}$ reflection, signaling that a fraction of the BYTO nanoparticles present an epitaxial relationship with the YBCO.

All the X-ray diffraction (XRD) measurements were performed by the technicians of the ICMAB.

2.6 Electrical transport measurements

The electrical transport measurements have been carried out by using a *Physical Properties Measurement System* (PPMS) from *Quantum Design* located at the ICMAB. This equipment is composed by a 9T superconducting magnet and a helium cryostat. Precise temperature control can be reached within the range of 1.8-400K. The system also incorporates a nanovoltimeter and an AC/DC current source, which can provide currents from 1 μA to 2 A with a resolution of 0.1 μA.

As YBCO is superconducting, its electrical properties have to be measured with a specific contact configuration. Samples are patterned by using an optical lithography process. First, the Ag contact pads are deposited onto the sample surface and post-annealed. Afterwards, the desired pattern is transferred by covering the whole sample surface with a photosensitive polymer resist, which is then illuminated with optical light at the desired positions. Finally, those exposed regions are etched using a corrosive acid, thus obtaining the YBCO bridges that are used for the transport measurements, with width values ranging between 4-100 μm. This patterning process and the resulting transport measurements of the YBCO samples were carried out by the PhD students Ferrán Vallès and Juri Banchewski, supervised by the Dr. Anna Palau and Prof. Teresa Puig.

In the other studied compounds (RNO and LSMO), the electrical transport properties were obtained by depositing four contacts at the corners of each sample surface with Ag ink, in a Van der Pauw configuration. The transport properties of the RNO samples were performed by the PhD student Julia Jareño, supervised by the Prof. Teresa Puig, while the resistivity measurements of the LSMO samples were performed by the Dr. Anna Palau.

2.7 Magnetic properties

The magnetic properties of the studied samples were extracted by using a *Superconducting Quantum interference Device* (SQUID) magnetometer provided with a 5.5 T and 7 T superconducting coils. The magnetic properties of the YBCO samples were carried out by the phD student Ferrán Vallès and Dr. Anna Palau, whereas the magnetic properties of the LSMO films were measured by Dr. Mariona Coll. The ICMAB technician Bernat Bozzo also contributed to these measurements.

2.8 Magnetic Nuclear Resonator

The Mn oxidation state of LSMO samples was also evaluated by using a *magnetic nuclear resonator* (MNR). In this experiment, the sample is illumi-

nated with electromagnetic radiation, which is absorbed and re-emitted at specific resonant frequencies by the crystal nuclei. The intensity and frequencies of tis re-emitted radiation can be correlated with the magnetoelectronic states of the crystal nuclei. Further information about this technique can be found in Ref. [28]. These experiments were carried out by the Prof. Marek Wojcik and Prof. Ewa Jedryka at the *Institute of Physics, Polish Academy of Sciences, Warszawa, Poland.*

2.9 Density Functional Theory

Density Functional Theory (DFT) is a quantum mechanical modeling method, nowadays used in many disciplines, used to investigate the electronic configuration associated to the ground state of a many-body system. Instead of solving the Schrödinguer equation associated to the many-body system, the electronic configuration is obtained by using *functionals*, which are functions of another function, that depends on the charge density. Therefore, this theory exposes that any many-body system can be described by its corresponding charge density function and external potentials.

DFT is based on describing the energy of an interacting electron system by using the electron density as a key quantity. In the same way that the ground-state electron density of an interacting electron system is derived from the external potentials, a unique external potential can be derived from a certain electron density function. In 1964, Hohenberg and Kohn demonstrated that the ground state energy of any system can be described by using functionals of the charge density (n), $E = E(n)$ [29]. The authors also proved that, for any positive trial density (n_t), such that $\int n_t(r)dr = N$, being N the total amount of electrons in the system, then $E[n] \geq E_0$, where E_0 is the ground state of the system.

In this thesis, we have used DFT theory to study the stability of specific vacancy configurations within the Y123 structure and Y248 intergrowth defect. This is evaluated by comparing their associated formation energies, which are calculated by DFT. The formation energy for a vacancy V_x is calculated by:

$$E_f = E_T(V_x) - E_T(H) + \mu_x \tag{2.3}$$

where $E_T(V_x)$ is the total energy of a supercell with V_x, $E_T(H)$ is the total energy of the host supercell, and μ_x is the chemical potential for the species x (for compound defects a similar term is added for each atom missing from the host supercell). Since doped YBCO is metallic, all supercells are considered charge neutral. The lattice parameter is allowed to change, so that finite size effects are smaller.

The calculations have been performed using the projector augmented wave method [30] and the Perdew-Burke-Ernzerhof (PBE)-GGA exchange-correlation functional [31] as implemented in the VASP code [32–34]. The energy cutoff for the plain-wave basis is 500 eV and a 6x6x1 mesh have been used for the integration in the Brillouin zone. A Hubbard-U correction within the rotationally invariant Duraev implementation [35] has been included, with a value of U_{eff}=8 eV for electrons in the Cu *3d*-orbitals. The structural parameters were relaxed until the Hellmann-Feynman forces were less than 0.01 eV/Å. Spin polarized calculations were employed in all cases.

DFT calculations were performed by Prof. Rohan Mishra, the Dr. Guangfu Luo and the PhD student Steven Hartman, all of them from the *Institute of Materials Science and Engineering, Washington University in St. Louis, EE.UU.*

Chapter 3

The challenging microstructure of YBCO thin films

3.1 Chapter preview

This chapter, which is divided into two blocks, is devoted to the structural characterization of the $YBa_2Cu_3O_7$ (YBCO) superconducting material. In the first block, we focus on the microstructural study of epitaxial nancomposite (NC) YBCO films, where randomly oriented oxide-based nanoparticles are trapped within the YBCO matrix. In the second block, we study all the structural distortions, at the sub-angstrom resolution, that appear around one of the most common defect found in YBCO, this is, the Y124 intergrowth.

In the first block, we first study the possibility of mixing two different kind of oxide-based NPs within the same NC film. In each sample, we evaluate the density and length of the appearing Y124 intergrowths in order to establish correlations between the structural and electrical properties. Secondly, we study the film microstructure of a new family of NC films, the preformed nanoparticle NCs films. The main advantages associated to this new methodology are the better control on the NP properties, the possibility to achieve faster growing rates (via the flash heating process) and larger film thicknesses (up to 1 micrometer).

In the second block, we study the real structure of the Y124 intergrowth defect and all the emerging distortions resulting from point defects located either within the defect itself or at the surrounding YBCO cells. First, we show how the off-stoichiometry issue associated to the generation of the Y124 intergrowth is compensated by the formation of oxygen-decorated pairs of copper vacancies within the very same intergrowths. Secondly, we unveil the presence of addi-

tional oxygen vacancies within the neighboring BaO planes, in a periodical and uneven distribution manner. We also measure all the atomic shifts occurring within the YBCO unit cell. Finally, we discuss the possible implications that all of these observed distortions have in the YBCO physical properties.

3.2 Microstructure of YBCO nanocomposite films

3.2.1 Physical and Structural properties

Superconducting properties

Superconductivity was discovered in 1911 by Heike Kamerlingh Onnes as Hg exhibited an abrupt transition from metallic to a new zero-resistance state when the material was cooled down below a certain temperature. This temperature, that defines the superconducting-normal state transition, is named *critical temperature* (T_C). In 1957, Bardeen, Cooper and Schiffer proposed one explanation for this phenomenon (BCS theory) based on the coupling of pairs of electrons that fall into the ground state, forming a bose condensate [36]. These electron pairs, called Cooper-pairs, can move coherently without the dissipation of energy.

The superconducting state is also characterized by the capacity to expel the magnetic flux from inside the material. This phenomenon is called *Meissner effect* and was discovered by Meissner and Ochsenfield in 1933. This expulsion of the magnetic field is accomplished by the generation of supercurrents circulating on the surface of the material. Indeed, the magnetic flux decrease exponentially in the regions where these supercurrents circulate. The distance defined by this exponential gradient is the *penetration depth* parameter (λ). The normal-superconducting interface is also characterized by the *coherent length* (ξ), defined as the distance where the density of Cooper-pairs (also known as order parameter, n_c) changes from 0 to its maximum value.

In 1950, Gindburg and Landau classified the superconductors in two different types according to how the magnetic field penetrates the material: Type I and II. In the case of type I superconductors, the magnetic flux never enters the material as it is expelled by the generation of the aforementioned

supercurrents. However, if the external magnetic field is larger than a critical value, named critical magnetic field (H_C), the material can not maintain the superconducting state and it recovers the normal state. The maximum current density that any superconducting material can transport before entering the normal state is given by the *critical current density* (J_C).

In the case of type II superconductors, an additional magnetic state appears between the Meissner and normal state, named *mixed state*. In the mixed state, the magnetic flux enters the material in the form of quantized cylindrical flux lines, which are called *magnetic vortices* [37]. The density of Cooper-pairs in the central part of those vortices is 0, which means that the vortex core (with radius ξ) is non-superconducting. Each vortex has a fixed magnetic flux quanta of $\phi_0 = \frac{h}{2e} = 2.07 \cdot 10^{-15}\, Tm^2$, which is generated by the supercurrents that circulate around its core, in a region delimited by the coherence length ($\lambda > \xi$). As it is displayed in the H-T diagram of Fig. 3.1 (a), the boundaries of the mixed state are defined by the critical magnetic fields H_{C1} and H_{C2}. Those type II superconductors that are still superconducting at high magnetic field and temperature conditions ($\approx$ liquid nitrogen temperature) are also known as *High Temperature Superconductors* (HTS).

The magnetic vortices are forced to move through the crystal due to the Lorentz-like forces that appear because of the presence of the supercurrents ($\vec{F_L} = \vec{J} \times \vec{B}$). This vortex motion dissipates energy, which lowers the J_C. Nevertheless, this energy dissipation can be minimized when the vortices are immobilized. Due to the non-superconducting vortex core nature, the vortices like to remain within the non-superconducting areas or lattice imperfections of the YBCO crystal that have similar dimensionality than its vortex core diameter ($\approx 2\xi$). As the amount of vortices generated within the material scales with the strength of the applied magnetic field, more defects are required when the magnetic field is increased in order to pin the additional vortices. Therefore, the pinning performance of YBCO films are enhanced when additional nanometer-sized defects are created. In addition, as ξ changes with temperature, not all defects are equally efficient at a certain temperature.

The normal-superconducting transition is not abrupt. Under high tem-

peratures and magnetic fields, the material enters within the "vortex liquid" regime where vortices are spontaneously activated from its pinning sites by thermal effects. As a consequence of that, the material is resistive in this regime ($J_C \approx 0$), even though it is still superconducting. The boundary between the "flux pinning" and "vortex liquid" regions is called irreversibly line (IL). This makes the IL parameter even more relevant than the upper critical magnetic field (H_{C2}) for technological applications.

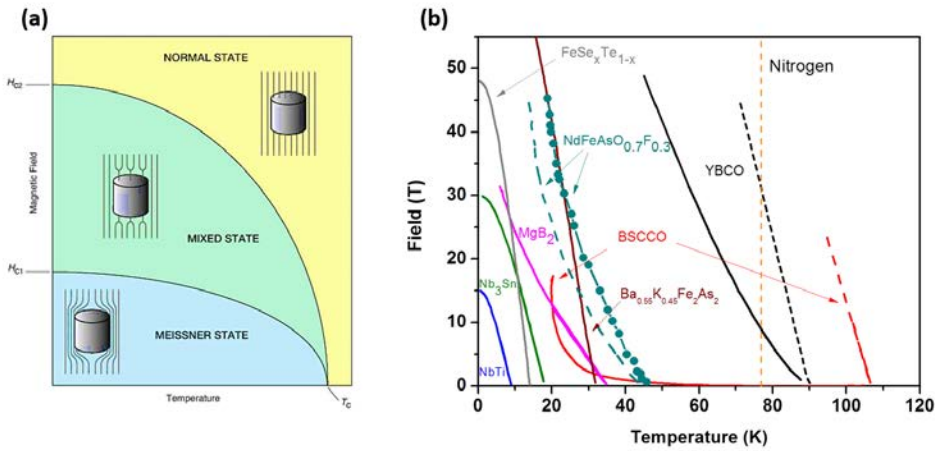

Figure 3.1: (a) Magnetic field vs. temperature phase diagram of a type II superconducting material. (b) Irreversibility lines (solid lines) and upper critical magnetic field curves (H_{C2}) (dashed lines) of some of the most used superconducting materials. The black lines correspond to the YBCO material.

Fig. 3.1 (b) shows the upper critical magnetic field value (H_{C2}) and IL for the most common superconducting materials. Among all the type II superconductors, the YBCO, discovered by C.W. Chu [6], is one of the most promising candidates for power applications [38] because, although it is not the superconducting material with higher H_{C2} value, it is the one with the largest IL. In fact, YBCO reaches the superconducting state at $T_C = 92K$, far above the Nitrogen liquid temperature (77K), which drastically reduces its working costs respect other superconducting materials.

Crystal structure

The $YBa_2Cu_3O_{7-\delta}$ (YBCO) unit cell structure is sketched in Fig. 3.2 (a). It can be described as an oxygen-deficient structure composed by three perovskite blocs, that are stacked along the c-direction, with lattice parameters $a = 3.823$Å, $b = 3.8863$Å and $c = 11.684$Å (for $\delta = 0.07$). While the Ba cation (green) seats at the center of the upper and lower perovskite blocks, the Y cation (yellow) is located at the center of the central block.

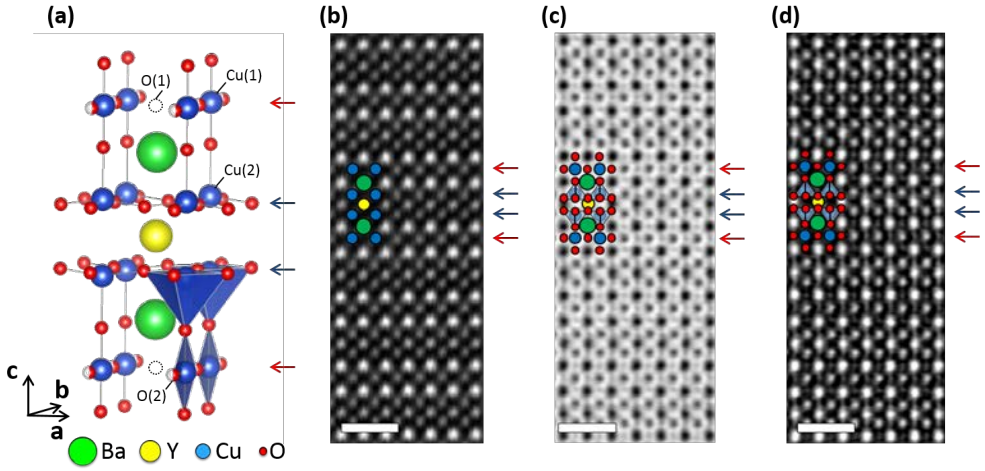

Figure 3.2: (a) Sketch of the orthorhombic YBCO unit cell. Ba, Y, Cu and O are represented in green, yellow, blue and red, respectively. (b) Z-contrast, (b) ABF and (d) contrast-inverted ABF images, showing the YBCO crystal structure viewed along the <100> zone-axis. Scale bars: 1nm. The blue and red arrows point towards two superconducting CuO_2 planes and two CuO chain layers, respectively.

The coordination between the Cu and O atoms depends on their crystallographic position. In particular, Cu(2) atoms are coordinated with five O atoms forming a tetrahedron whose base is superconducting. On the contrary, in the orthorhombic structure, Cu(1) atoms are coordinated with four O, all confined at the same a-c plane. This is the reason why these Cu-O layers are referred to as chain layers. While the crystallographic position O(1) always remains empty, the amount of oxygens within the O(2) position is triggered by the total

oxygen content of the structure (δ). Indeed, this inhomogeneous distribution of oxygen vacancies along the *a*- and *b*-axes generates the orthorhombic symmetry associated to the YBCO structure.

Fig. 3.2 (b) shows a high resolution Z-contrast image where the YBCO structure is viewed along the <100> zone-axis. The brightness associated to each atomic column is barely proportional to its Z^2 number [14]. Therefore, the brightest columns are associated to Ba cations (green), followed by the Y cations (yellow) and finally by the Cu ones (blue).

In addition to the Ba, Y and Cu cations, the ABF image displayed in Fig. 3.2 (c) also reveals the oxygen sub-lattice of the YBCO structure. All O atoms belonging to the superconducting planes (blue arrows) are not confined at the same basal plane than their bonded Cu. They are slightly shifted towards the Y cation, drawing a rippling pattern with the Cu atoms when moving along the basal direction, see Fig. 3.2 (d). Certainly, the overlapping between the Cu *3d*- and O *2p*-electronic shells depends on this Cu-O bond length and angle, which should have a relevant influence in the physical properties of YBCO [39–41].

The YBCO properties also depend on the total oxygen content $(7-\delta)$ within the structure. For instance, it is well known how this parameter influences the T_C and the J_C in bulk YBCO single crystals [39]. In particular, the T_C is maximized at 92 K when the YBCO structure has an optimal oxygen doping of 0.93 ($\delta = 0.07$). The amount of carriers within the superconducting planes is linked to the amount of oxygen vacancies within the chain layers (V_O), which act as charge reservoir for the superconductivity [42, 43]. Besides, the YBCO structural parameters are also influenced by the amount of oxygen within the chain layer positions [39].

The shear strains associated to the orthorhombic unit cell structure, with slightly different *a* and *b* parameters, are released by forming twin domains where the YBCO unit cell is rotated 90° [44–48]. These twin domains are homogeneously separated by coherent planes running along either the <110> or <1$\bar{1}$0>, which are named twin boundaries (TBs). When the YBCO structure is

viewed along the <100> or <010> zone-axes, the twin domains are separated by coherent vertical lines where the *a*- and *b*-axes successively alternates [48]. In bulk single crystals, the separation between TBs mainly depends on the the YBCO grain size [49]. Otherwise, the TB spacing is observed to vary with the film thickness or substrate mismatch in epitaxial YBCO thin films [50].

Importance of defects

The term "defect" has been normally associated to a negative connotation. However, the presence of defects is highly desirable in the YBCO material, as they contribute to the pinning of magnetic vortices. However, not all of them are beneficial for this purpose. Vortices only get pinned in those defects with similar dimensionality than its core diameter ($\approx 2\xi$), where the supercurrents that create the magnetic flux quanta are still able to circulate around the edges of the defect. Otherwise, larger defects are detrimental for the YBCO properties as they are not able to pin vortices, but act as blocking barriers for the supercurrents. This explains why both the physical and microstructural properties of YBCO films are strongly correlated. For instance, either the IL can be shifted towards H_{C2} values, or larger J_C can be reached at certain field conditions, when a particular defect landscape is optimized [51–53] .

The first evidence regarding the advantages of creating additional defects within the YBCO lattice was observed when YBCO was grown in the form of thin films. Researchers discovered that the IL was automatically shifted to larger temperatures and fields as a direct consequence of the larger amount of defects compared to bulk single crystals [54–56]. Afterwards, researchers tried to improve the pinning performance of YBCO thin films by creating artificial defects by means of irradiating the YBCO structure with electrons, protons or charged ions [57] or by decorating the substrate surface with dispersed NPs prior to the YBCO growth [58–60]. In all cases, the authors reported an enhancement of the pinning performance when the external magnetic field was oriented parallel to the YBCO *c*-axis due to the abundant presence of columnar defects. This kind of pinning mechanism was referred to as "correlated pinning", as they observed a clear correlation between the particular geometry of the crystalline defects and the specific magnetic field orientation where the

pinning performance was improved. On the contrary, the case of "uncorrelated" or "random" pinning sites refers to those pinning contributions that are effective independently of the magnetic field orientation. Accordingly, the "uncorrelated" pinning mechanisms tend to favor an isotropic pinning behavior.

Our research group has a long expertise on the fabrication of *c*-axis textured YBCO nanocomposite (NC) thin films onto oxide crystal substrates, where oxide-based NPs are trapped within the YBCO matrix [48, 51, 52, 61, 62]. The introduction of the NPs within the YBCO matrix favors the nucleation of additional defects, which improve the pinning efficiency of the YBCO NC films, thus increasing their J_C. In this thesis, pristine films refer to YBCO films that do not contain NPs.

In this chapter, we will present the structural and physical properties of two different families of NC films: the spontaneously segregated (ss-NC films) and the preformed nanoparticle (pn-NC films) NC films. In the ss-NC films, the NPs are generated *in situ* during the same heating step as that of the epitaxial YBCO film. The nanoparticles nucleate and grow slightly before the YBCO growth, during the heating step [51, 52, 61, 63–66]. In the pn-NC films, a colloidal solution is formed with the mixture of the YBCO preocursor phases and the preformed metal oxide NPs, with a well-defined size and structure [62, 67–69]. Similar fabrication steps are followed in both approaches, which are explained in the following section.

Growing process of ss-NC films

YBCO thin films (either NC or pristine) are grown following a Chemical Solution Deposition (CSD) process based on the decomposition of Metal-Organic Trifluoracetates (MOD-TFA), proposed by Gupta et al. at 1988 [70]. This method lowers the YBCO fabrication costs and increases the YBCO growing rate compared to physical processes, where high vacuum chambers are required [71]. The growth comprises four steps: deposition, pyrolisis, annealing and oxygenation [52, 62, 65, 72–74].

First, the YBCO solution is prepared by mixing the YBCO powder within trifluoroacetic acid. The mixture is stirred and heated at 50°C for 72 h, and

afterwards filtered and evaporated under vacuum. The mixture of TFA salts ($Ba(TFA)_2$, $Cu(TFA)_2$ and $Y(TFA)_3$) is then dissolved in methanol [75]. The molar concentration of the TFA salts is 0.25 M, 0.50M and 0.75M, respectively, leading to the required stoichiometric ratio of 1:2:3. Extra amount of precursor salts containing the desired transition metal cation (Zr, Hf, Co,...) are also incorporated within this precursor solution [51, 52].

This solution is then **deposited** by spin coating onto the desired single crystal oxide substrate. The solvent is removed during the spinning of the solution and a flat gel is formed. This procedure is only effective for laboratory-scale samples where typically small substrates (25 cm^2) and thin films (< 300 nm) NC films are grown. However, this method is easily scalable to thicker films and longer lengths by depositing the YBCO precursor solution using the Ink-Jet printing technology [76, 77]. This equipment permits to deposit single YBCO precursor solution droplets by applying electric pulses to a piezoelectric print-head.

The formed gel undergoes a first thermal process during the **pyrolisis** step. In particular, the sample is loaded within a tubular furnace with controlled temperature ($\approx 300°C$) and oxygen flux flow ($0,07l/min$) conditions for approximately 30 min. During this process all the organic phases are evaporated.

Finally, the chemical reactions that leads to the YBCO phase occurs during the **annealing** step. The sample is placed within a tubular furnace that is heated until 800°C during 3h, with a constant nitrogen flow rate of 0.6 l/min and a very low oxygen partial pressure (200 ppm). At these growing conditions, the YBCO nucleates in the tetragonal phase. The YBCO structure becomes orthorhombic when the furnace is cooled down. In order to ensure an optimal oxygen concentration ($\delta = 0.07$), films are kept within the furnace at temperatures around 450°C under a higher O partial pressure for several hours. This last step is called **oxygenation**.

Properties of single ss-NC films

The structural properties of a 200nm-thick pristine and a 200nm-thick 10% molar $BaZrO_3$ (BZO) ss-NC YBCO thin films, both grown onto $LaAlO_3$ (LAO) single crystal substrates, are compared in Fig. 3.3. Previous results demonstrated that the optimal BZO concentration that maximizes the J_C of the ss-NC films is a 10% [78]. Fig. 3.3 (a) and (d) show the 2-dimensional X-ray diffraction (2D-XRD) patterns measured in the pristine and ss-NC films, respectively.

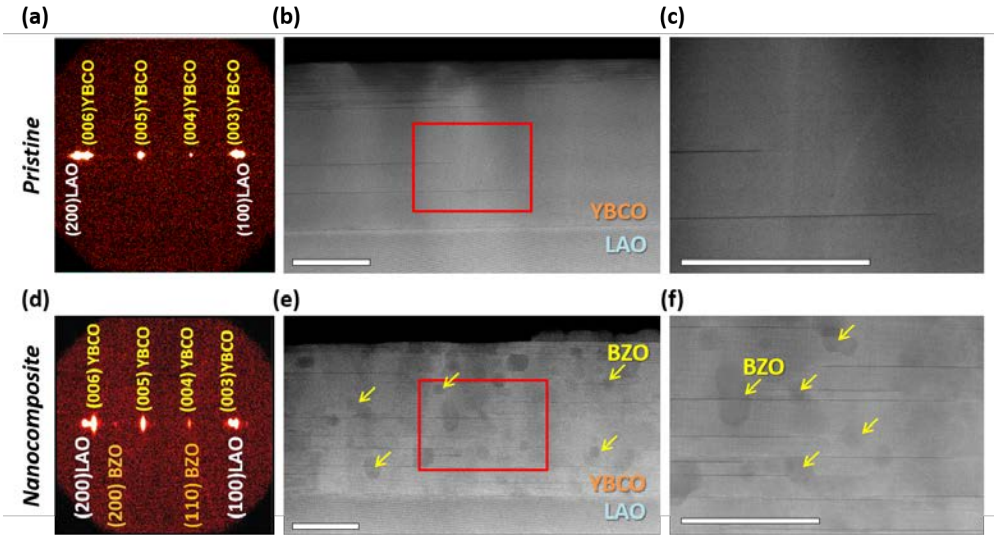

Figure 3.3: 2D-XRD patterns of (a) a pristine and (d) a 10% BZO ss-NC films. Low-magnification Z-contrast images of (b) the pristine film and (e) the ss-NC sample. The areas marked with red squares in (a) and (e) are displayed with higher magnification in (c) and (e), respectively. Some BZO NPs are marked with yellow arrows. Scale bars: 100nm

A first evaluation of the YBCO texture and NP orientation can be extracted from the XRD patterns shown in Fig. 3.3 (a) and (d). We only identify the $(00l)_{YBCO}$ and $(00l)_{LAO}$ reflections in both pristine and ss-NC films, which confirms the growth of c-axis textured YBCO. Besides, these reflections are centered at $\chi = 0$ and have a spot-like shape, which is a

prof of the good crystal quality and orientation. Growing biaxially textured YBCO films is crucial for having good electrical performances because the superconductivity only occurs through the ab-planes, which have to remain parallel to the substrate surface. Hence, the formation of misoriented YBCO grains within the YBCO films drastically reduces their J_C. Even though the $(00l)_{YBCO}$ spots are slightly enlarged along χ in the ss-NC film compared to the pristine sample, the measured misorientation angle is lower than 6°, which is the maximum value before the J_C starts to decrease [79, 80].

The weak ring-shaped signal appearing between the $(004)_{YBCO}$ and $(100)_{LAO}$ reflections in the 2D-XRD pattern of the ss-NC film, see Fig. 3.3 (d), is ascribed to the $(110)_{BZO}$ reflection, which is the most intense one. The $(110)_{BZO}$ reflection is detected for all the χ values, forming a ring-shaped reflection geometry, which indicates that most of the trapped NPs are randomly oriented respect the YBCO matrix. Otherwise, the spectrum also contains a spot-like reflection placed at $2\theta = 42.7°$ and $\chi = 0$ between the $(005)_{YBCO}$ and $(006)_{YBCO}$ reflections, which is ascribed to the $(200)_{BZO}$ reflection. The appearance of this reflection means that some NPs keep an epitaxial relationship with the YBCO and substrate crystals. Typically, is observed that those NP remaining onto the substrate surface are the ones that maintain a cube-on-cube epitaxial relationship with the substrate crystal [51, 62, 65].

Fig. 3.3 (b) and (e) show low magnification Z-contrast images of the pristine and ss-NC films, respectively. The regions marked with the red squares are displayed in Fig. 3.3 (c) and (f) (pristine and ss-NC films, respectively). Both films exhibit different microstructures. In the pristine sample, only few dark stripes running along the basal plane are identified, which are mainly localized at the film surface. Otherwise, in the BZO ss-NC film, we observe the presence of BZO NPs (dark circles) that are well dispersed throughout the film, with an averaged diameter of 20-30nm. A larger concentration of these characteristic stripes is also identified in this ss-NC film compared to the pristine one, being them homogeneously distributed through the film. Indeed, these dark stripes are the result of the presence of the most common defect observed in the YBCO films, the $YBa_2Cu_4O_8$ (Y124) intergrowth [22, 48, 52, 81–83].

The atomic structure of one isolated Y124 intergrowth defect is shown in the high resolution Z-contrast images that are displayed in Fig. 3.4 (a) and (b), where the YBCO lattice is viewed along the <100> and <010> zone-axes, respectively. The Y124 intergrowth is a planar defect that consists of a non-conservative stacking fault based on the introduction of an additional Cu-O plane at the chain layer position, forming a double-chain layer. For this reason, the Y124 intergrowth defect is also referred to as "*stacking fault*" or "*double-chain layer*". At either side of the defect, the structure is shifted half-unit-cell along the b-axis, leading to a displacement vector of $\frac{1}{2}[0\frac{b}{2}\frac{c}{6}]$ [22, 48, 52, 83]. The additional Cu-O plane creates a partial

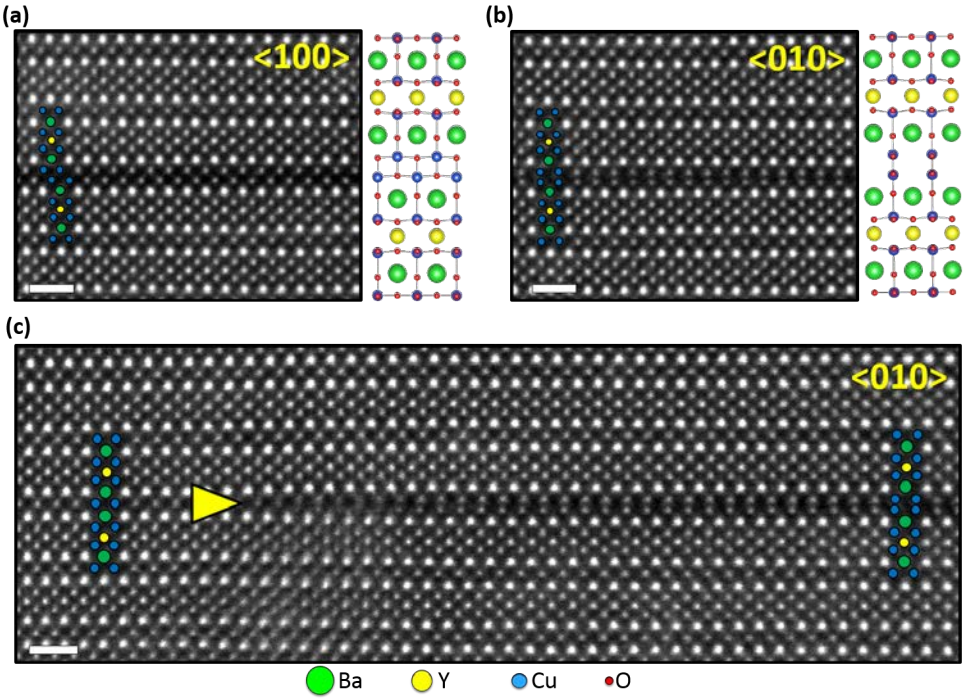

Figure 3.4: High resolution Z-contrast images of an isolated Y124 intergrowth embedded within the YBCO crystal structure, which is viewed along either the (a) <100> or (b,c) <010> zone-axes. The edge of the planar defect, composed by a partial dislocation, is viewed in (c) (yellow arrow). The YBCO structure is sketched with green (Ba), yellow (Y) and blue (Cu) circles. Scale bars: 1nm.

dislocation that is localized at the edge of the planar defect. The partial dislocation is indicated with a yellow arrow in the Z-contrast image of Fig. 3.4 (c).

The same isolated Y124 intergrowth is displayed with a lower magnification in the Z-contrast and the low-angle annular dark field (LAADF) images of Fig. 3.5 (a) and (b), respectively. The strain fields associated to the structural distortions can be imaged in the LAADF images [19–22].

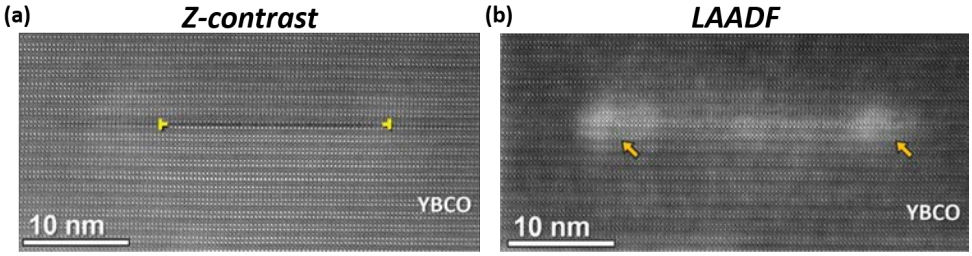

Figure 3.5: (a) Z-contrast and (b) LAADF images of an isolated Y124 intergrowth. The yellow crosses and orange arrows signal the partial dislocations positions, where the strain fields are localized.

The Y124 intergrowth is easily identified in the Z-contrast image, as it is viewed as a horizontal dark stripe. The partial dislocations localized at the edges of the planar defect are indicated with yellow crosses. As both images are acquired simultaneously, the partial dislocations are placed at the same image positions (orange arrows) in the LAADF image, see Fig. 3.5 (b). Notice that the contrast is enhanced around these positions, signaling the presence of strain fields that rapidly vanish, i.e., they are strongly localized around the partial dislocations [22]. *R. Guzman et al.* reported that a tensile-strain value of 1% is generated in these areas.

The presence of localized strain fields may act as a novel pinning mechanism according to the Bond contraction Pairing model theory (BCP) proposed by *G. Deutscher et al.* [84]. The author suggests that the Cooper-pair formation can be locally quenched in the presence of tensile-strain fields greater than a 1% value. This novel pinning mechanism was previously demonstrated to be effective in the ss-NC films [52].

As previously shown in Fig. 3.3, larger amount of Y124 intergrowths are generated in the ss-NC films compared to the pristine ones. This occurs because this defect helps to partially release the accumulated surface energy generated by the incoherent interfaces between the randomly oriented NPs and the YBCO matrix [52]. The relevance of the Y124 intergrowths on the pinning properties of YBCO films is investigated by analyzing the electrical behavior of both pristine and ss-NC films under the influence of external magnetic fields. It should be mentioned that similar J_C^{sf} values ($J_C^{sf} = J_C^{self\,field} = J_C(H = 0)$), around 4 MA/cm^2 at 77K, are typically measured in either pristine or ss-NC films.

In Fig. 3.6 (a) it is plotted the measured J_C as a function of the external magnetic field in both films, when H is oriented parallel to the YBCO c-axis. The particular microstructure of each film give rise to different electrical behaviors. The pristine film exhibits three differentiated regimes: first J_C is constant until an approximate field value of 10^{-2} T (single vortex regime), then the J_C starts to decay linearly with H (until approximately 5 T) and finally J_C decays exponentially. On the other hand, in the ss-NC film, the initial plateau is enlarged until an approximate field value of 10^{-1} T and then

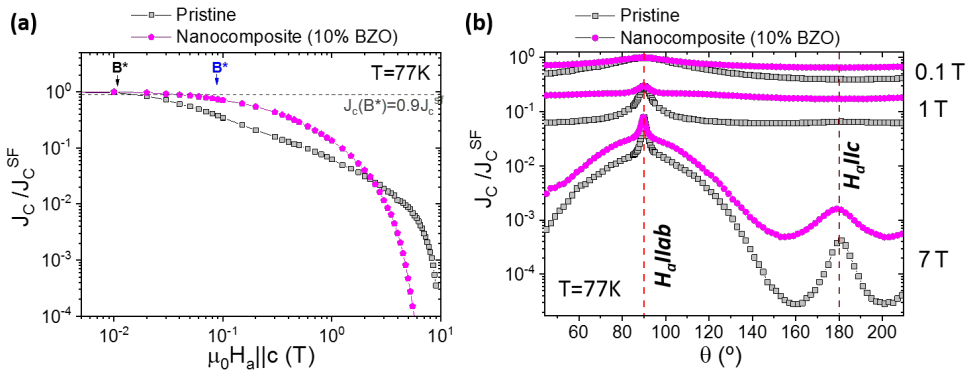

Figure 3.6: J_C dependency as a function of the (a) applied magnetic field strength and (b) orientation from a pristine (gray circles) and a single ss-NC (pink circles) films. The dashed lines in (b) indicate the configuration where the external magnetic field is oriented parallel to either the YBCO c-axis ($\theta = 180°$) or ab-planes($\theta = 90°$).

a rounded-like dependency is identified.

The enhancement of J_C at low fields can be evaluated using the applied magnetic field at which the "single" and "collective" pinning regimes split up, referred to as B^*. In the single vortex regime (B<B*), vortices do not interact between them and J_C(H) dependency is a plateau. Once the B* value is crossed, vortices start to interact between each other and the critical current density decays faster. The B* value is directly calculated from these curves at the specific magnetic field value where the J_C has decayed a 10% respect the initial J_C^{sf} value. Typically, the NC films (pink circles) exhibit larger B* parameters compared to pristine films (empty squares), as shown in Fig. 3.6 (a). The larger amount of pinning centers in the NC films (mainly Y124 intergrowths) shifts the B* parameter to higher values. Interestingly, a crossover between both curves is identified at magnetic field values around 3 T, being the pristine film the one that exhibits better pinning performances close to the IL conditions.

The appearance of this crossover is associated to the structural interaction between the twin boundaries (TB) and the Y124 intergrowth defects [53]. As the twin domains, and hence the TBs, are formed during the last stage of the YBCO annealing process when the YBCO transits from the tetragonal to the orthorhombic phase, the TBs have to travel from their nucleation positions throughout the YBCO film, thus encountering all of the already formed lattice defects. In the case of pristine films, a very low amount of defects is present and therefore the TBs remain as homogeneously separated vertical planes as in the case of bulk single crystals. In the case of ss-NC films, the TBs find a different YBCO microstructure, with a lot of NPs, Y124 intergrowths, strain fields, and so on. In this scenario, their accommodation is more complex, loosing the vertical coherence that is observed in pristine films and single crystal samples [48, 85]. As the TBs pin those vortices that are oriented parallel to the YBCO c-axis, acting as a correlated pinning defect, they are more efficient at very high mangetic fields and temperatures (when H_a ||c) than the strained areas localized around the Y124 intergrowth. It is worth mentioning that this effect is not noticed at lower temperature conditions, where the ss-NC-films exhibit much better pinning performances than pristine

films for all the measured range of fields and temperatures [53].

In Fig. 3.6 (b), the J_C is plotted as a function of the magnetic field orientation (θ). An anisotropic behavior is identified in all the curves obtained from the pristine film. In particular, they are composed by two maximums centered at $\theta = 90°$ and $\theta = 180°$, which correspond to the configuration where the magnetic field is oriented either parallel or perpendicular to the YBCO *c*-axis, respectively. Accordingly, these pinning contributions are ascribed to the presence of TBs ($\theta = 180°$) and Cu-O chain layers ($\theta = 90°$). Otherwise, an isotropic behavior is observed in the curves associated to the ss-NC film at 0.1T and 1T, being the J_C almost constant regardless of the θ value. This isotropic behavior is also ascribed to the larger presence of short Y124 intergrowths, which are homogeneously distributed through the NC film. However, the isotropic behavior is lost at high magnetic fields, even though the emerging pinning maximums are still broader than in the case of pristine samples.

3.2.2 Mixed spontaneously segregated NC films

Up to now, it has been summarized the accumulated knowledge of our research group regarding the physical and structural properties of single ss-NC thin-films, containing one NP specie. From now on we will show the newest results regarding the microstructural characterization of NC films and its correlation with their physical properties. First, we have evaluated the effect of introducing two different NP species within the same ss-NC film, which are referred to as *mixed ss-NC films*. It has to be remarked that the optimal NP concentration that maximizes the J_C of single ss-NC films was found to be a 10% molar in the case of BZO ss-NC-films and a 6% molar in the case of Ba_2YTaO_6 (BYTO) ss-NC films [52]. In addition, both BZO and BYTO NPs tend to keep a random orientation whereas the Y_2O_3 (YO) NPs prefer to establish an epitaxial relationship with the YBCO matrix [52]. We have studied four mixed ss-NC films, all having similar film thicknesses around 200 nm, each one containing the following NP composition: 10% BZO + 5% YO, 5% BZO + 5% YO, 5% BZO + 6% BYTO, 6% BYTO + 10% Cu. The aim of combining BZO and YO NPs is to study the effect of having a combination

of epitaxial and randomly oriented NPs within the same YBCO film. On the other hand, we have tried to reduce the NP agglomeration by mixing BZO and BYTO NPs in order to increase the total NP concentration. The latter combination (BYTO + Cu) was designed in an attempt to increase the amount of Y124 intergrowths as a result of introducing an excess of Cu. The resulting

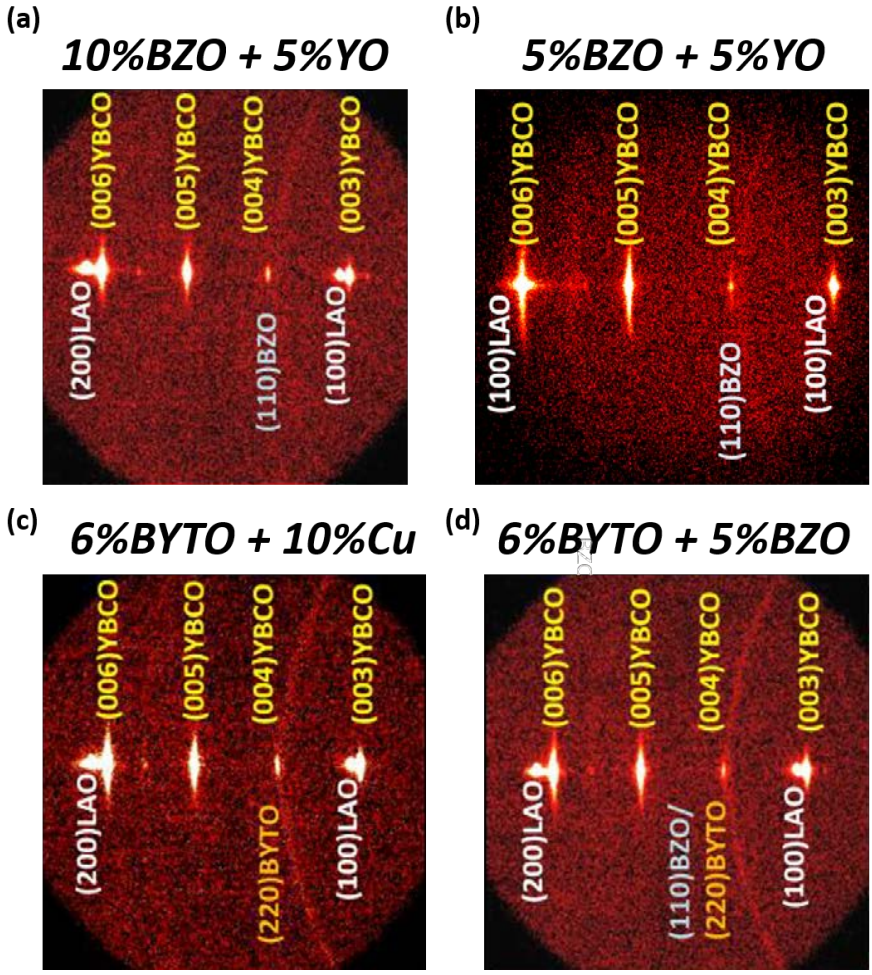

Figure 3.7: 2D-XRD patterns from the (a) 10% BZO+5% YO, (b) 5% BZO+5% YO, (c) 6% BYTO+10% Cu and (d) 6% BYTO +5% BZO mixed ss-NC films.

microstructures are firstly evaluated from the 2D-XRD patterns, which are shown in Fig. 3.7 (a-d).

Spot-like $(00l)_{YBCO}$ diffraction peaks are identified in all films, confirming the c-axis texture of the YBCO films. The YBCO diffraction peaks are enlarged few degrees along χ, which suggests that some YBCO grains are slightly misoriented. However, the misorientation degree never raises the critical 6° value and therefore good J_C^{SF} values are achieved from all films (≈ 4 MA/cm^2). The observed ring-shaped signals are ascribed either to the $(110)_{BZO}$ or $(220)_{BYTO}$ diffraction peaks of the randomly oriented NPs. In the case of the 6% BYTO + 5% BZO ss-NC film, the $(110)_{BZO}$ or $(220)_{BYTO}$ reflections overlap and therefore they can not be distinguished. The microstructure of all the studied mixed ss-NC films is investigated in more detail by acquiring Z-contrast images, which are shown in Fig. 3.8 (a-d).

All films have the expected nominal thickness, around 200 nm. Besides, the identification of horizontal Y124 intergrowths (black stripes) in all films confirms that the YBCO grows with a c-axis texture in all samples. In the case of the BZO+YO ss-NC films, see Fig. 3.8 (a) and (b), some homogeneously-dispersed rounded aggregates (yellow arrows) are identified, which correspond to the BZO NPs, as it will be confirmed below. In the case of the BYTO ss-NC films, see Fig. 3.8 (c) and (d), the NPs can not be identified due to the strong contrast variations. However, as we will show later, they also remain trapped within the YBCO matrix. In all films, some big aggregates are also observed (darker phases), which are ascribed to the presence of other secondary phases ($Y_2Cu_2O_5$, BaF_2 and CuO) that remain trapped within the YBCO lattice. These phases are products or precursors of the chemical reactions that generate the YBCO phase [72]. Like in the single ss-NC films, where only one kind of NP is used, the amount of Y124 intergrowths increases in all of the studied mixed ss-NC films compared to the pristine sample.

Fig. 3.9 shows high magnification Z-contrast images of some of the phases that remain trapped within the previous films. Fig. 3.9 (a) displays one of which its chemical composition is determined using EELS-SI. The obtained Cu, O and Ba EELS compositional maps are shown in Fig. 3.9 (b), (c) and

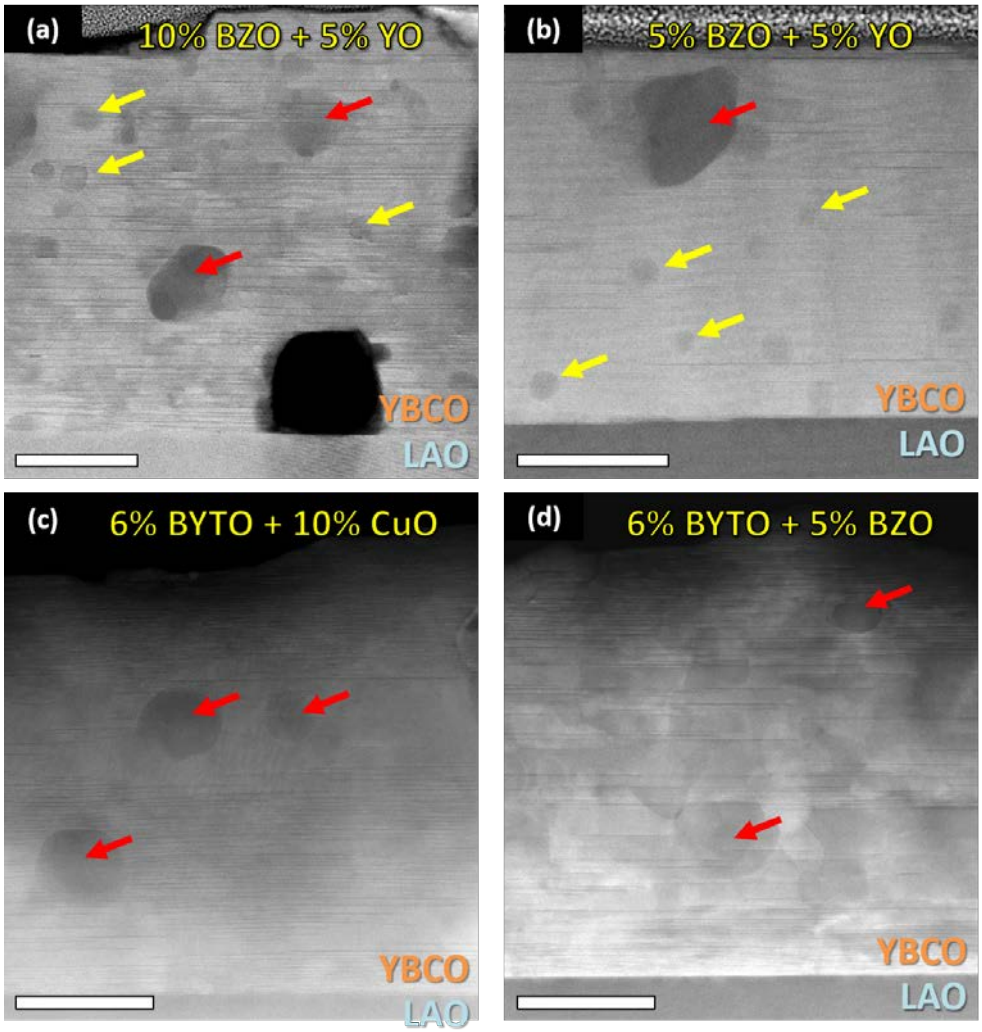

Figure 3.8: Low magnification Z-contrast images of the (a) 10% BZO+5% YO, (b) 5% BZO+5% YO, (c) 6% BYTO+10% CuO and (d) 6%BYTO +5% BZO. The yellow and red arrows points to BZO/BYTO NPs and additional phases. Scale bars: 50 nm.

(d), respectively, which are obtained by integrating the characteristic Cu L_{23}, O K and Ba M_{45} peak signals. The fact that the Ba signal decreases within the rounded phase while both the Cu and O signal do not vary, indicates that

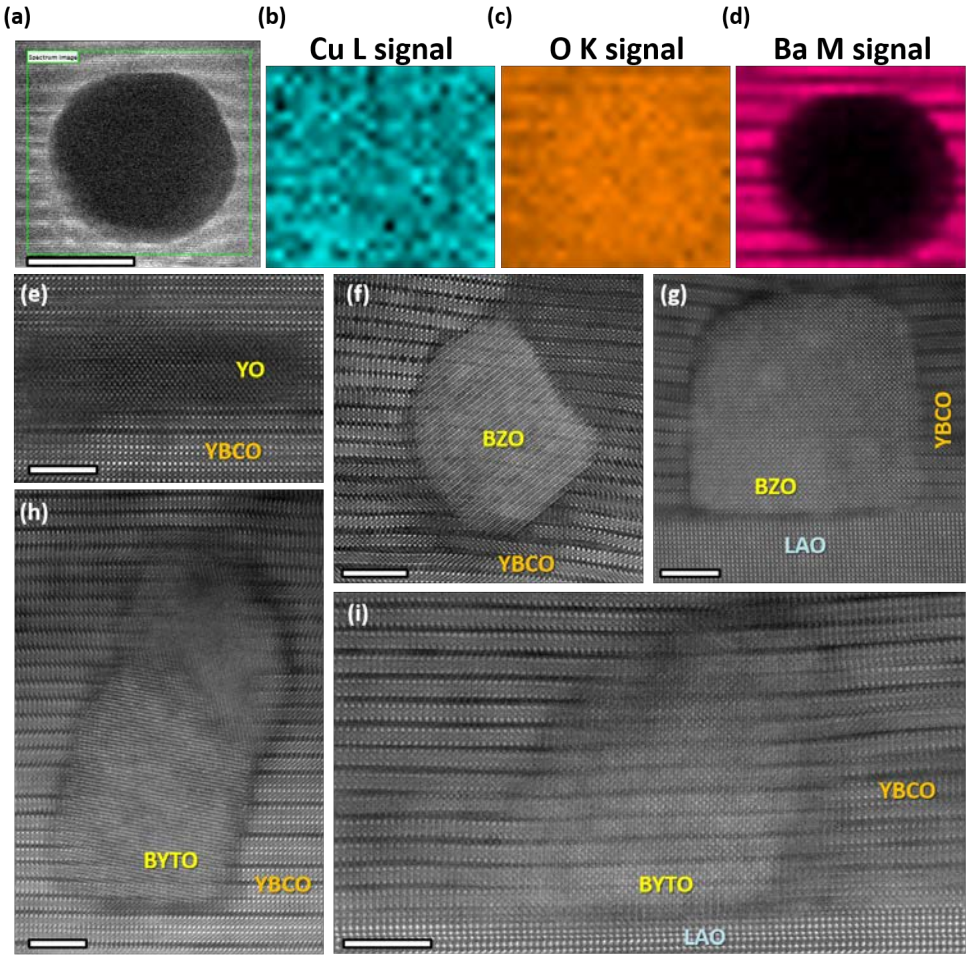

Figure 3.9: (a) Z-contrast image showing one dark and rounded phase that is trapped within the YBCO lattice. Scale bar: 50nm. An EELS-SI is acquired from the green-squared area. The obtained Cu, O, Ba compositional maps are shown in (b), (c) and (d), respectively. Z-contrast images of (e) an epitaxial YO NP, (b) a randomly oriented BZO NP, (c) an epitaxial BZO NP, (d) a randomly oriented BYTO NPs and (e) an epitaxial BYTO NP observed within the studied mixed ss-NC films. Scale bars: 5nm

this aggregate is either CuO or $Y_2Cu_2O_5$.

In Fig. 3.9 (e-f) it is shown high magnification Z-contrast images of epitaxial YO NP and randomly- and epitaxially-oriented BZO and BYTO NPs, respectively. As previously commented, the YO NPs maintain an epitaxial relationship with the YBCO lattice, as well as those BZO/BYTO NPs covering the substrate surface. Otherwise, the BZO/BYTO NPs that remain trapped within the YBCO matrix keep a random orientation. The averaged diameter of these NPs is found to be around 20nm. Besides, some agglomeration and coarsening effects between NPs occur during the YBCO growth.

Fig. 3.10 (a) displays the $J_C/J_C^{sf}(H)$ curves of the fabricated mixed ss-NC films. Two additional curves are also included in the plot, one belonging to a pristine sample (empty circular dots) and the other one to a 8% BYTO ss-NC film (brown hexagons), which is reported in Ref. [61, 65].

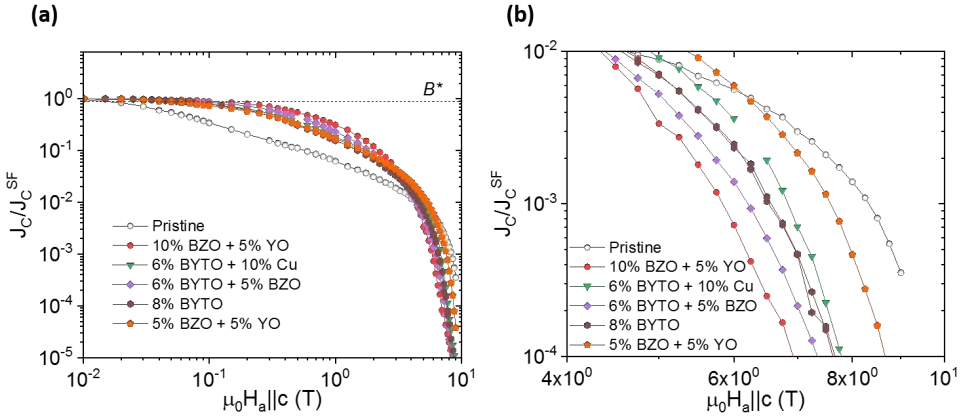

Figure 3.10: (a) $J_C/J_C^{sf}(H)$ curves corresponding to the studied ss-NC films. The B* value from each curve is extracted from the crossover between the $J_C/J_C^{sf}(H)$ curves and the dashed line (J=0.9J_C^{SF}). (b) An amplified view of the plot shown in (a) at very high fields.

The rounded-like behavior, typically observed in the single ss-NC films (brown hexagons), is also identified in all the mixed ss-NC films, which signals that the YBCO microstructure in both mixed and single ss-NC films is similar.

Only a slight J_C enhancement is observed in both the 10% BZO + 5% YO (red circles) and 6% BYTO + 5% BZO (pink rhomboids) ss-NC films for magnetic fields values lower than 3T. A closer look at the IL conditions (high magnetic fields) of the plot is shown in Fig. 3.10 (b). No additional pinning contributions are observed to occur from the epitaxial YO NPs. Besides, those films that present a larger B* value also exhibit lower J_C performances at very high field conditions (close to the IL), which evidences an inverse correlation between the B* and IL parameters at high temperatures (77 K) [53]. As previously mentioned, this inverse correlation only occurs when H is oriented parallel to the YBCO *c*-axis as a result of the lost of the TB vertical coherency due to the abundant presence of Y124 intergrowths and NPs. It is important to remark that although TB planes with no vertical coherence are not very effective pinning centers at high temperatures (close to the irreversibility line) they preclude vortex channelling at low temperatures, which might induce fast vortex motion [53].

Even though we have succeed on trapping a mixture of different kind of NPs within the same mixed ss-NC film, no relevant differences have been observed between the single and mixed ss-NC films regarding their microstructure and electrical properties. This result indicates that the fact of trapping two different kind of oxide-based NPs within the same NC film do not supply significant benefits respect introducing only one type. Besides, it seems that adding an excess of Cu content within the YBCO precursor solution, do not favors the formation of extra Y124 intergrowths but cuprate-based secondary phases.

We have further evaluated the density and length of the Y124 intergrowth that are present in all the studied mixed ss-NC samples in order to establish correlations between their structural and physical properties. The obtained results are displayed in the histograms of Fig. 3.11, where we have plotted the Y124 intergrowth density as a function of their length (in groups of 10nm) for each NC film.

Clearly, the concentration of short Y124 intergrowths (length<50 nm) is drastically enhanced in all the ss-NC films compared to the pristine

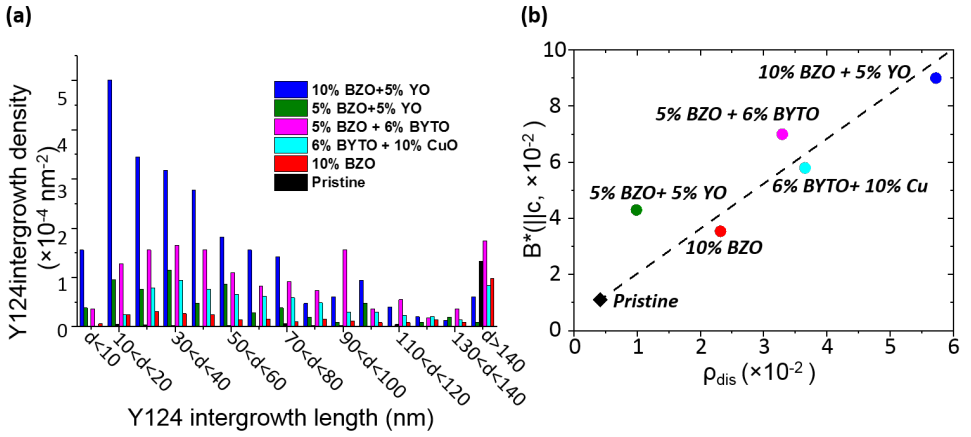

Figure 3.11: (a) Histogram showing the measured Y124 intergrowth density as a function of their length for the studied ss-NC (colors) and pristine (black) films. (b) Calculated ρ_{dis} associated to each sample, plotted as a function of its corresponding B* parameter. The dashed line signals the linear correlation between both parameters.

film, where only a few amount of large intergrowths (length>150 nm) is present. The averaged Y124 intergrowth length is therefore shifted from 150nm (or even larger values), in pristine samples, towards 30-50nm, in ss-NC films. The 6% BYTO+10% Cu film present a lower concentration of Y124 intergrowths than the the 6%BYTO + 5% BZO film, which evidences that adding an excess of Cu within the YBCO precursor solution do not promote the generation of Y124 intergrowths. The films that exhibit the highest B* values (10%BZO +5% YO and 6% BYTO and 5% BZO films) also have the largest density of short Y124 intergrowths, which signals the direct correlation between these two parameters. In order to further confirm this result, we have estimated the relative volume of strained YBCO regions (ρ_{dis}) in each sample by assuming that the Y124 intergrowths are circles with toroid-like shaped strained areas localized around their perimeter. In the appendix A, it is explained in detail how the ρ_{dis} parameter is calculated.

Fig. 3.11 (b) shows the ρ_{dis} value as a function of the B* parameter for each particular sample. A linear dependency between both parameters is identified, which means that the amount of pinning sites increases with the

density of strained areas. This result confirms the BCP theory and validates the hypothesis that the nanometer-sized strained regions act as a novel pinning mechanism in YBCO [86].

In short, we have demonstrated that the YBCO defect landscape that boost the pinning performance of YBCO NC films is the one composed by short Y124 intergrowths homogeneously dispersed through the YBCO film. When this occurs, the vortices are equally pinned for all magnetic orientations, reaching an isotropic pinning behavior. However, this particular defect configuration brakes the vertical coherence of the TBs, which reduces the pinning efficiency at the temperature and field conditions close to the IL, when H is oriented parallel to the YBCO *c*-axis. Therefore, the optimal YBCO defect landscape has to be designed as a function of the real conditions (temperature, magnetic field strength and orientation) at which the YBCO film will work.

3.2.3 Preformed nanoparticle NC films

Even though the 200 nm-thick ss-NC films already exhibit good superconducting properties, with T_C and J_C values around 90-92 K and 4 MA/cm^2, respectively, many problems were encountered when we tried to increase the film thickness. Besides, the ss-approach offers a low control on the final NP properties, mainly on their size and shape, because they spontaneously nucleate and grow during the annealing process. In addition, the NPs tend to coalescence and aggregate, specially in the case of thicker films, which reduces the effective cross section area of the films and lowers their electrical performances. The *preformed nanoparticle* route was designed in an attempt to overcome all of these problematics and to have more control on the final NP properties [62, 67–69, 87]. These new kind of NC films are referred to as *preformed nanoparticle-NC films* (pn-NC).

In this section, we show the structural and physical properties of pn-NC films that contain either a 20% molar of $BaHfO_3$ (BHO) or BZO NPs. A colloidal solution is formed by mixing the YBCO precursor phases with the already synthesized NPs [62, 69]. The absence of precipitates after several days confirms the stability of the final solution. By using this approach, we are able to increase the NP concentration up to a 20% molar while keeping the good

superconducting properties [69]. The films here studied were grown onto LAO single crystal substrates with nominal thickness around 120 nm. The averaged as-synthesized diameter of both BZO and BHO NPs was found to be around 10 nm [69]. Fig. 3.12 (a) and (d) display the 2D-XRD patterns obtained from a BZO and a BHO pn-NC films, respectively. All the $(00l)_{YBCO}$ reflections have a dot-like shape geometry, which confirms the growth of well-textured YBCO films. However, no Bragg reflections associated to either the BZO or BHO interplanar spacings are identified.

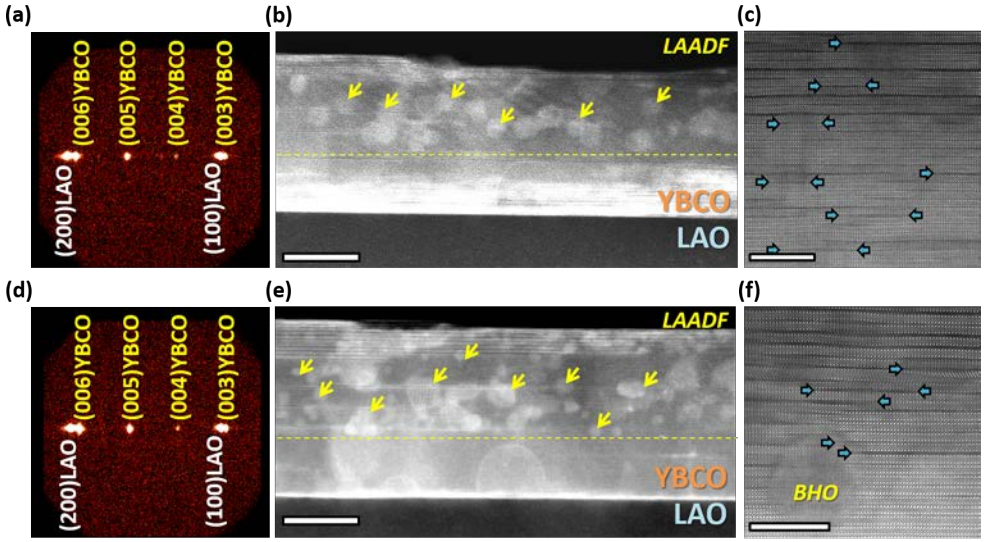

Figure 3.12: 2D-XRD patterns of (a) the 20% BZO and (d) BHO pn-NC films. Low magnification LAADF images of (b) the BZO and (e) the BHO pn-NC films. Scale bars: 50 nm. High magnification Z-contrast images of (c) the BZO and (f) the BHO pn-NC films. Scale bars: 10 nm. The dashed yellow lines indicate the seed-NC interfaces. The yellow and blue arrows point towards some BZO/BHO NPs and Y124 intergrowths, respectively.

In order to confirm that the BZO and BHO NPs remain trapped within the YBCO matrix and to further investigate the films' microstructure, we have acquired LAADF and Z-contrast images, which are shown in Fig. 3.12. Fig. 3.12 (b) and (e) show the low magnification LAADF images of the BZO and

BHO pn-NC films, respectively. The LAADF detector helps to identify how the NPs are dispersed within the YBCO matrix, as they appear as small and bright circular areas (some of them are marked with yellow arrows). Notice that no particles are present within the first 50 nanometers of the film. This first layer, which is referred to as *seed layer*, is used to avoid the nucleation of polycrystalline YBCO. In the absence of the seed layer, it was observed that most of the substrate surface tended to be covered by the NPs and, therefore, the epitaxial relationship between the YBCO and substrate was lost. We have fabricated this kind of heterostructure by using the same CSD-process, but with a two-step pyrolysis procedure. In particular, we have firstly deposited by spin coating and then pyrolyzed the first seed layer. Afterwards, we have deposited the pn-NC layer onto the as-pyrolyzed seed layer, also by spin coating, and we have carried out a second pyrolysis heat treatment in all the sample. Finally, both layers are annealed together and a continuous YBCO film is crystallized. The interface between both layers can be determined where the firsts NPs are found. This interface is observed to be placed 50 nm far from the substrate-film interface, which coincides with the seed layer nominal thickness. In the pn-NC layer, an homogeneous dispersion of the NPs is observed, with a low amount of agglomeration. Although most of the NPs keep their initial size, around 10 nm, the averaged NP diameter is found to be around 15nm due to coarsening effects or because of the incorporation of Y within its structure. However, the obtained value is lower than the averaged diameter of ss-NC films (20-30nm). Fig. 3.12 (c) and (f) display high resolution Z-contrast images corresponding to the central film areas of the BZO and BHO pn-NC films, respectively. The blue arrows indicate the presence of short Y124 intergrowths, whose generation is also promoted by the presence of the BHO or BZO NPs within the YBCO host lattice.

Two high resolution Z-contrast images of the trapped 10nm-sized BZO and BHO NPs (yellow arrows) are displayed in Fig. 3.13 (a) and (b), respectively. The fast-fourier transform pattern (FFT) associated to each Z-contrast image is displayed in the images' inset. This pattern is generated from the brightness periodicities that are present in the Z-contrast images. As this pattern belongs to the reciprocal space, the reflections that are placed close to the central position correspond to those periodicities having a larger

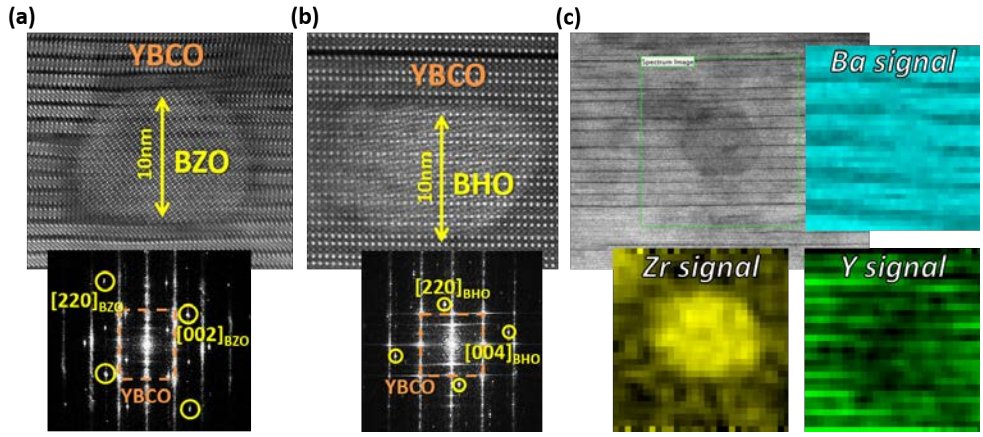

Figure 3.13: High magnification Z-contrast images of randomly oriented (a) BZO and (b) BHO NPs trapped within the YBCO matrix. The insets show the fast-fourier transform (FFT) patterns associated to each Z-contrast image. (c) Z-contrast image of the BZO pn-NC film with a NP (dark circle) from where an EELS-SI image has been acquired (green rectangle). The insets show the obtained Ba- (blue), Zr- (yellow) and Y- (green) compositional maps

amplitude and vice-versa. The appearing reflections in the FFT pattern of Fig. 3.13 (a) are associated to the $\{002\}_{BZO}$ and $\{220\}_{BZO}$ family planes (yellow circles), which are rotated 34° respect the $(100)_{YBCO}$ and $(001)_{YBCO}$ reflections (orange rectangle), respectively. The yellow spots observed in the FFT pattern of Fig. 3.13 (b) correspond to the $(004)_{BHO}$ and $(220)_{BHO}$ reflections, which are rotated 12° respect the $(100)_{YBCO}$ and $(001)_{YBCO}$ ones (orange rectangle), respectively. The measured BZO and BHO interplanar spacing matches well with the corresponding bulk values, which confirms the chemical composition of the viewed NPs. Besides, both NPs are observed to be randomly oriented respect the YBCO host matrix, as in the case of ss-NC films. We have additionally acquired an EELS-SI from the green squared region of the Z-contrast image shown in Fig. 3.13 (c), where a NP is present (dark rounded circle). This Z-contrast image was acquired from the BZO pn-NC film. The obtained Ba, Zr and Y compositional maps are displayed in the inset of Fig. 3.13 (c) as blue, yellow and green color maps, respectively. The compositional maps confirm that the NP region is Ba- and Zr-rich, *i.e.*,

that it is a BZO NP.

The measured J_C^{sf} values at 77K of the studied BZO and BHO pn-NC films are 3.7 MA/cm^2 and 3.1 MA/cm ^{2}, respectively, which are comparable to the values exhibited by the ss-NC films. In Fig. 3.14 (a) it is plotted their J_C/J_C^{sf} curves as a function of the external magnetic field (oriented parallel to c) at 77K. Two additional curves are also included as a reference, one belonging to a pristine sample (open black circles) and the other one to a 10% BZO + 5% YO ss-NC film (blue). Both pn-NC films exhibit a similar rounded-like electrical behavior than ss-NC films, with larger B* values than pristine samples. However, their electrical performances are still lower than the ones offered by the ss-NC films.

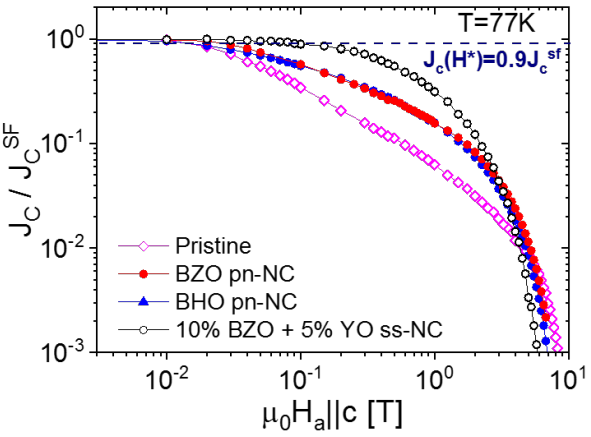

Figure 3.14: (a) $J_C/J_C^{sf}(H)$ curves corresponding to the BZO (red) and BHO (blue) pn-NC films. The black circles and magenta hexagons correspond to a pristine and a 10%BZO +5% YO ss-NC samples.

As expected, the pristine film has the largest IL, as the vertical coherence of the TB is maintained. Otherwise, the lowest IL value correspond to the ss-NC film, where the coherency of the TBs is lost. In the pn-NC films, an intermediate scenario is identified, which suggests that the TBs are still coherent is some areas. In order to further investigate this phenomenology, we

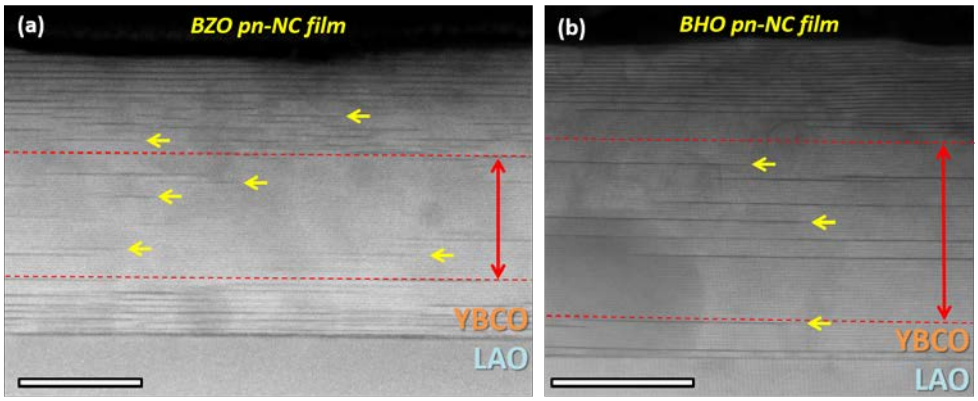

Figure 3.15: Z-contrast images of (a) the 20% BZO and (b) BHO pn-NC films. The yellow arrows point towards some Y124 intergrowths. The red dashed lines indicate the area with lower concentration of Y124 intergrowths. Scale bars: 50 nm.

have acquired additional Z-contrast images of the BZO and BHO pn-NC films, which are shown in Fig. 3.15 (a) and (b), respectively. Some of the Y124 intergrowths that are present within these films are indicated with the yellow arrows.

Even though the density of Y124 intergrowths is higher in the pn-films compared to the pristine samples, they have a central area (the one comprised between the red dashed lines) where the Y124 intergrowth density is significantly lower than in the ss-NC films. There, the TBs keep the vertical coherence and therefore they are still capable to pin some vortices at high magnetic fields conditions. Accordingly, the pn-NC films have a particular microstructure that can be understood as an intermediate scenario between the pristine and ss-NC microstructures. This is the reason why their J_C values are comprised between the pristine and ss-NC curves in the $J_C(H)$ plot.

As we have previously commented, some NPs increase their initial size due to agglomeration and coarsening effects. In order to minimize this problematics, we have tried to increase the YBCO growth rate by fabricating the samples with the *Flash heating* (FH) treatment.

Flash heating

A similar fabrication process that the one used to grow pn-NC films is used in the *Flash heating* approach, with the novelty that samples undergo a thermal shock during the annealing step. This is accomplished by pre-heating the furnace until the desired temperature, 750° in this case, and then loading quickly the sample. Samples transit from room temperature to 750° in few seconds, as shown in the heat diagram of Fig. 3.16 (a). By using this approach, the kinetics of all the occurring chemical reactions are accelerated and hence the YBCO growth rate, which should reduce the coalescence and agglomeration of NPs.

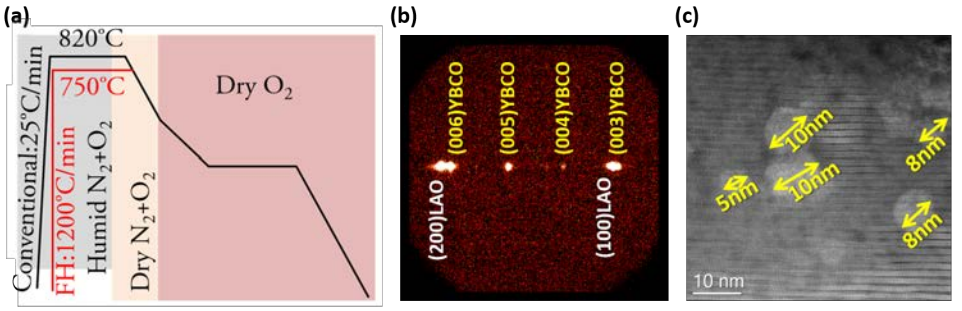

Figure 3.16: (a) Heating profiles used in the conventional (black line) and FH (red line) approaches. (b) Typical 2D-XRD pattern obtained from a FH-derived YBCO film. (c) Z-contrast image of a FH-derived BZO pn-NC film where some BZO NPs are viewed.

We have used this methodology to grow a 200 nm-thick pristine film and a 120 nm-thick 20% BZO pn-NC film, both onto LAO single crystal substrates. Similar 2D-XRD patterns are obtained from both samples like the one shown in Fig. 3.16 (b). The $(00l)_{YBCO}$ and $(00l)_{LAO}$ diffraction Bragg reflections are only identified, which have a dot-like geometry centered at $\chi = 0$, like in the YBCO films grown by the conventional method. This confirms that the YBCO has a *c*-axis texture when it is grown by the FH approach. Fig. 3.16 (c) shows a high resolution Z-contrast image of the FH-derived BZO pn-NC film where some BZO NP are identified. It is observed that the averaged BZO diameter is close to the as-synthesized value (10nm) when this approach is

used. This confirms that the coarsening effects are lowered when faster YBCO growth rates are used.

The microstructure of a pristine and a 20% pn-NC films, both grown by the FH approach, are evaluated by acquiring the Z-contrast images that are shown in Fig. 3.17 (a) and (b), respectively. Both films are compared with

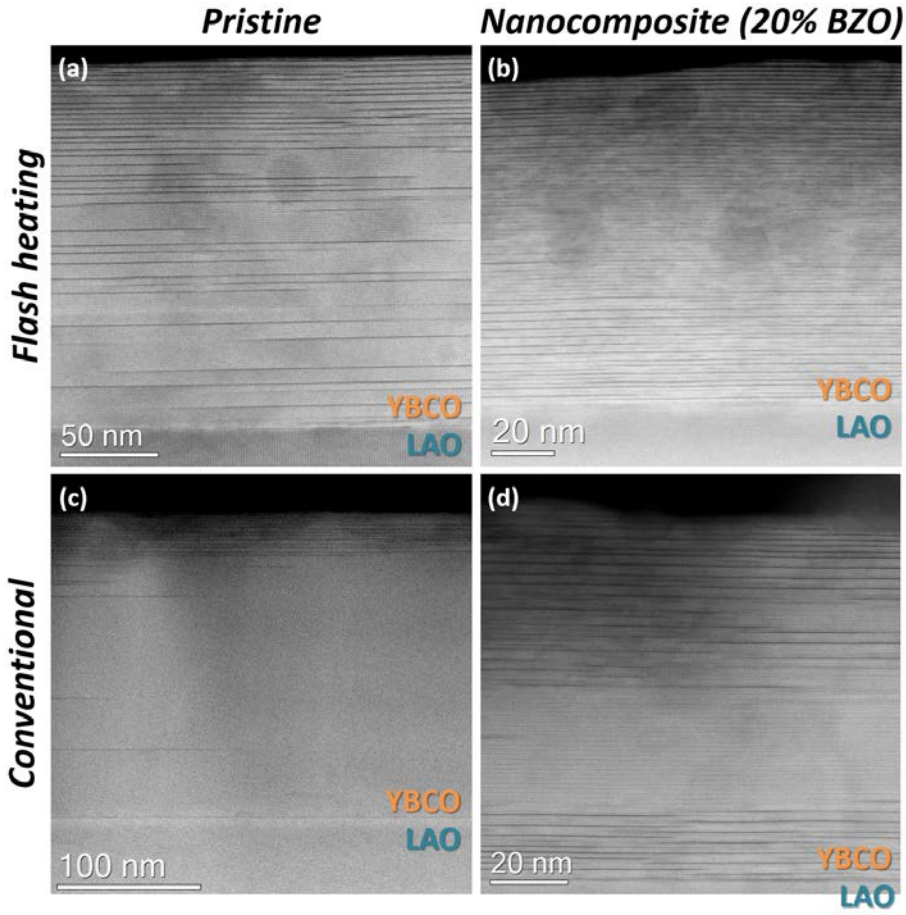

Figure 3.17: Z-contrast images of pristine and 20% BZO pn-NC films fabricated by the FH (a-b) and the conventional (c-d) approaches.

similar ones fabricated by the conventional process, which are shown in the Z-contrast images of Fig. 3.17 (c) and (d).

The FFT patterns (not shown) associated to the Z-contrast images shown in Fig. 3.17 confirm the biaxial texture of all the samples. However, the density and distribution of the generated Y124 intergrowth is observed to be different in each film. Indeed, if we compare the structural properties of samples that are grown by the conventional and by the FH processes, it is clearly observed that higher amount of short Y124 intergrowths are formed in the FH-derived ones. In order to confirm that, we have calculated the amount of Y124 intergrowths that are identified in the images of Fig. 3.17. This is represented in Fig. 3.18 (a) as histograms that gather the number of viewed Y124 intergrowths as a function of their length. In each particular growing process, the NC films always exhibit a larger amount of Y124 intergrowths compared to the pristine films. Besides, it is confirmed that larger amount of short Y124 intergrowths are generated when the FH approach is used, even in the pristine film. Interestingly, this result evidences that the growing process also influences the microstructural properties of the YBCO films.

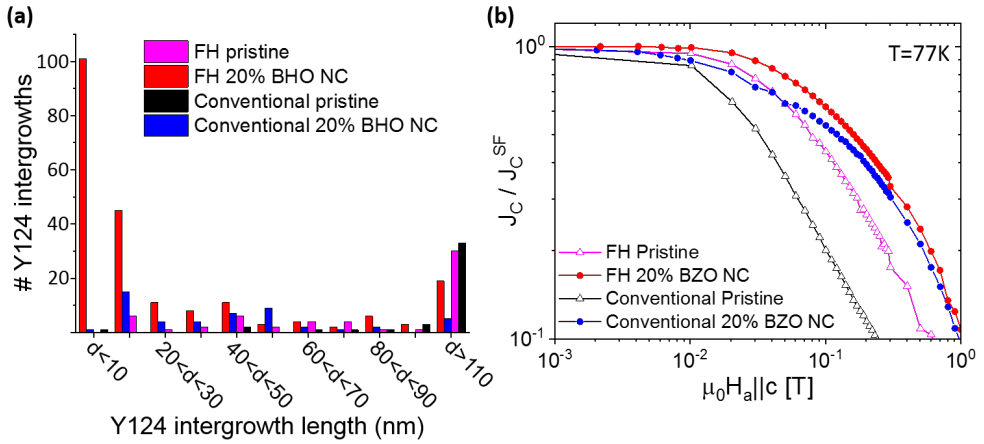

Figure 3.18: (a) Histograms showing the number Y124 intergrowths that are viewed in the Z-contrast images of Fig. 3.17 as a function of their length. (b) $J_C/J_C^{sf}(H)$ curves (with $H \parallel c$) at 77K from the studied samples.

Both FH-derived pn-NC and pristine films have similar J_C^{sf} values around 3 MA/cm^2. Although this J_C^{sf} value is acceptable, it is slightly lower than the J_C^{sf} values obtained from conventional films ($\approx$ 4 MA/cm^2). This is ascribed to the larger presence of big cuprate aggregates that reduce the effective cross section area of films. The J_C/J_C^{sf}(H) curves of the studied films, grown by the FH and conventional approaches, are shown in Fig. 3.18 (b). As expected, the larger amount of short 124 intergrowths shifts the B* to larger values in the case of FH-derived films, even in the pristine samples.

Thick films

One of the most common applications of the superconducting materials is the fabrication of cables that can carry high electrical currents. One of the key parameters that dictates the performance of a superconducting tape is the critical current that crosses a fixed 1 cm-width (A/(cm·w)). This parameter can be increased by either improving the material performance, i.e. the J_C, or by growing thicker films. As our current NC films are already close to their physical limit, it is much easier to fabricate thicker films. Unfortunately, the parameters that rule the chemical reaction dynamics depend on the amount of the reacting material. This occurs as the YBCO growth rate is lowered when the generated gases and precursor phases have to diffuse through more material, which facilitates the generation of undesired phases or pores. Accordingly, the experimental conditions for growing a 1 μm-thick or 200nm-thick YBCO films are different and therefore, the whole fabrication process has to be re-defined. This is even more complex in the case of NC films where additional problematics regarding the NPs might be encountered, such as agglomeration or coarsening effects.

In this section we demonstrate that it is possible to grow CSD-derived YBCO films with thicknesses around 1μm, keeping the *c*-axis YBCO texture, the homogeneously dispersed NPs and the good superconducting properties. Here, we describe the film microstructure of a 1 1μm-thick 12% BZO pn-NC film. We have used a substrate architecture composed by a first Zr-stablized Y_2O_3 single crystal substrate (YSZ) and a second buffer layer of *c*-axis textured $Ce_{0.9}Zr_{0.1}O_2$ (CZO) crystal. This heterostructure (YSZ/CZO) is used

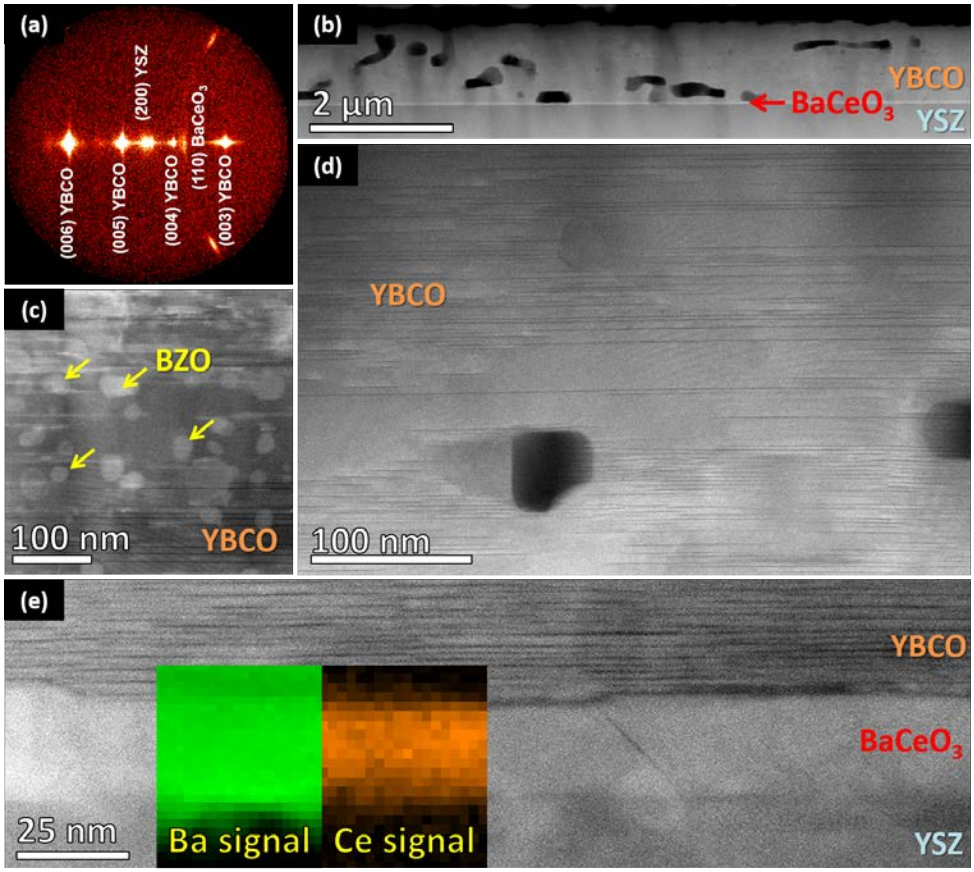

Figure 3.19: Microstructural analysis of the 1um-thick 12% BZO pn-NC film. (a) 2D-XRD pattern. (b) Low magnification Z-contrast image. (c) LAADF image, showing the homogeneous dispersion of BZO NPs within the film. (d) Z-contrast image of the central film area. (e) Z-contrast image of the YSZ/CZO-YBCO interface. Ba- (green) and Ce- (orange) compositional maps are superimposed onto the Z-contrast image, showing the chemical composition of the buffer layer.

in order to simulate as much as possible one of the substrate architectures that are commonly used in the commercial tapes, which is composed by an initial polycrystalline stainless steal layer and additional YSZ and CZO coatings [88]. The metallic layer protects the YBCO material while the oxide layers provide the crystal texture that is needed to grow c-axis oriented YBCO. The CZO

and the YBCO crystals have a very low lattice mismatch and this is the reason why this compound is used as a buffer layer. The studied film contains a 12% molar of BZO NPs which are previously synthesized and then diluted in the YBCO precursor solution, following the pn-approach. The film texture is firstly evaluated by acquiring a 2D-XRD pattern, which is shown in Fig. 3.19 (a).

The identification of dot-like shaped $(00l)_{YBCO}$ Bragg reflections confirms the c-axis texture of the YBCO film. Besides, a strong Bragg reflection is observed at the 2θ position corresponding to the $(110)_{BaCeO3}$ reflection, signaling that some $BaCeO_3$ (BCO) aggregates are formed. Besides, no Bragg reflections related to the CZO compound are identified, which suggests that the CZO layer might have reacted with the YBCO or other precursor phases, leading to the formation of a BCO layer.

Fig. 3.19 (b) shows a low magnification Z-contrast image of this 1μm-thick BZO pn-NC film. The film thickness value of 1 μm is confirmed, as well as the continuity and flatness of the film surface. Some darker regions are identified, which correspond to the presence of pores that remain trapped within the YBCO film. The homogeneous contrast within the YBCO film that can be observed in this image indicates that no big secondary phases neither misoriented YBCO grains are formed.

Fig. 3.19 (c) shows a low magnification LAADF image of the central region of the film where some NPs are viewed as rounded bright areas (yellow arows). An homogeneous distribution of NPs is confirmed, even though their averaged diameter (20nm) is increased a factor of 2 respect its original size (10 nm). As in the thinner pn-NC films, the NPs are randomly oriented respect the YBCO matrix. Fig. 3.19 (d) show a Z-contrast image of a central area of the film. The contrast homogeneity through several hundreds of nanometers confirms the good crystal quality, without any undesired secondary phase neither misoriented YBCO grains. The only impurity that can be identified in this image is the presence of some pores. Some Y124 intergrowths can be also identified, which are dispersed through all the film. However, their lengths (hundreds of nanometers) are observed to be larger than in the previously

characterized 120 nm pn-NC films.

In Fig. 3.19 (e), it is displayed a Z-contrast image of the film/substrate interface. The relative Ba- and Ce-content within the CZO buffer layer are evaluated by acquiring EELS compositional maps, which are shown as green (Ba) and orange (Ce) maps that are superimposed onto the Z-contrast image. A homogeneous Ba- and Ce-content is observed within the buffer layer, thus confirming the fully conversion of the CZO layer into the BCO one. Typically, the YBCO is observed to grow polycrystalline onto the BCO crystal as both compounds have a large lattice mismatch. However, in this case, we are able to avoid the nucleation of polycrystalline YBCO by lowering the annealing temperature down to 780°. Growing the YBCO at this temperature condition permits to nucleate the YBCO onto the CZO layer, before its conversion into the BCO layer. Therefore, we can preserve the YBCO *c*-axis texture even though the fully conversion of CZO into BCO.

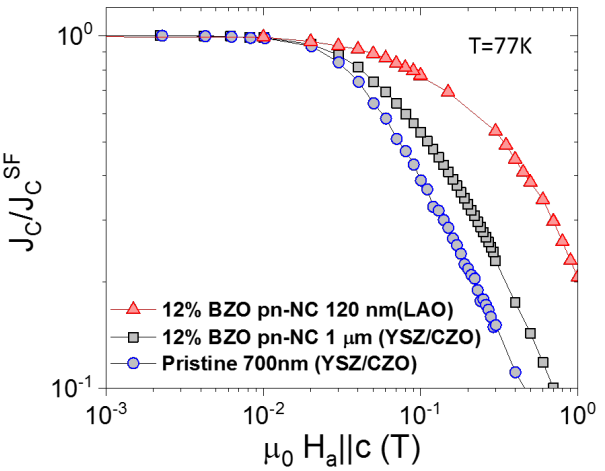

Figure 3.20: J_C/J_C^{sf}(H) curves at 77 K and $H \parallel c$ of the 1μm-thick 12% BZO pn-NC film (gray rectangles) and a 700 nm-thick pristine sample (blue circles), both grown onto YSZ/CZO substrate architecture, and of a 12% BZO pn-NC film (red triangles) grown onto a LAO single crystal substrate.

This film exhibits a T_C and J_C values of 90.5 K and 3.7 A/cm^2 at 77K, which yields to a 388.5 A/(cm^2·width). Notice that similar J_C values are achieved in the 120 nm-thick pn-NC films. Its corresponding $J_C/J_C^{sf}(H)$ dependency at 77 K is shown in Fig. 3.20 (gray squares). The resulting electrical behavior is compared with the ones obtained from a similar 700 nm-thick pristine film (blue line) and a 120 nm-thick BZO pn-NC film grown onto a LAO single crystal substrate. The 1 μm-thick BZO pn-NC film exhibits a smoother dependency than the pristine sample, but with lower J_C performances than the 120nm-thick pn-NC film, as the Y124 intergrowth are observed to be longer in the thicker film. This reduces the density of strained areas that are generated around the edges of the Y124 intergrowths. However, our results suggest that the pinning performance may increase if we are able to enhance the Y124 intergrowth density by increasing the NP concentration or reducing the averaged NP diameter.

3.2.4 Summary

In this first part of the chapter we have described the complex interplay between the YBCO microstructure and the physical properties of CSD-derived YBCO NC films.

We have shown that the NPs promote the presence of the most common defect found in YBCO films, this is the Y124 intergrowth. At the perimeter of this planar defect, it is localized a nanometer-sized YBCO area that is strained enough to locally quench the formation of Cooper-pairs. These areas act as a novel kind of "uncorrelated" pinning defect for the vortex motion. We have demonstrated that the pinning performance of YBCO films is significantly enhanced when the density of short Y124 intergrowths is increased, due to the larger density of these strained areas. However, we have also demonstrated that, when this occurs, the vertical coherence of the TBs is lost, which slightly reduces the pinning performance of the films at high fields and temperatures and when H is oriented parallel to the YBCO c-axis. For this reason, it is necessary to know at which field and temperature conditions the YBCO material has to work in order to engineer its optimal microstructure.

We have also investigated the possibility to mix two kind of NPs within

the same spontaneously segregated NC film (ss-NC films). Mixed compositions of BZO, BYTO, YO and Cu phases have been investigated. We have observed that the resulting films' microstructure and electrical properties are similar than those from single ss-NC films. Besides, we have estimated the density and length of the Y124 intergrowths that are generated within the studied films. From these measurements, we have been able to estimate the volumetric density of strained areas within each particular sample, which are localized around the perimeter of the Y124 intergrowths. We have observed that the relative fraction of strained areas linearly scales with the B* parameter.

Secondly, we have characterized the structural and physical properties of the preformed nanoparticle NC films (pn-NC), in which previously synthesized NPs are introduced within the YBCO precursor solution. We have observed that the fabricated pn-NC films exhibit similar electrical performances than ss-NC films. We have further exploited the better control on the NP properties that is offered by the pn-NC approach, to enhance the YBCO growing rate via the Flash heating route. We have observed that, when this approach is used, the NPs remain smaller and the amount of short Y124 intergrowths increases, thus opening new opportunities for engineering the defect landscape of the YBCO material.

Finally, we have demonstrated that it is possible to grow 1 μm-thick pn-NC films, keeping the c-axis texture, the crystal quality and the superconducting properties. The measured I_C value of 388.5 A/(cm^2·width) in this film makes the CSD-derived pn-NC a promising strategy towards the fabrication of CSD-derived commercial YBCO NC tapes, with good superconducting properties at high magnetic field and temperature conditions.

3.3 New insights onto the Y124 intergrowth

3.3.1 The real stoichiometry of Y124 intergrowth

In the previous sections, we have shown that in CSD-derived YBCO films displaying enhanced vortex pinning efficiency the introduction of secondary phases within the superconducting matrix renders a huge increase of the Y124 intergrowths. The extra amount of Cu that is needed for their formation would lead to a local Cu off-stoichiometry as either the solution precursors or the targets (used in magnetron sputtering or pulsed laser deposition techniques) used in the YBCO fabrication processes have an exact stoichiometry of $YBa_2Cu_3O_7$ (Y123). This controversy is automatically solved by the system during the YBCO growth via the introduction of Cu vacancies (V_{Cu}) within the Y124 intergrowth defect, also referred to as Cu-O double-chain layer [83]. These V_{Cu} permit to preserve the Y123 stoichiometry.

Fig. 3.21 (a) shows a Z-contrast image of the Y123 phase with two Y124 intergrowth defects, each one viewed either along the <100> (upper one) or <010> (lower one) zone-axis. The contrast within the upper Cu-O double-chain layer randomly varies along the basal direction, being the brightness lowered at some Cu sites (orange arrows). This signal lowering is ascribed to the presence of Cu vacancies (V_{Cu}) that are always ordered as vertical pairs. Otherwise, the contrast is observed to be homogeneous within the lower Cu-O double-chain defect, which is viewed along the <100> zone-axis, thus indicating that the pairs of V_{Cu} are only ordered along the *b*-axis. In Fig. 3.21 (b) and (c), it is displayed the Cu and O EELS compositional maps as red and green color maps, respectively. The vertical profiles correspond to the relative atomic composition (Cu and O) depth-profiles, which are obtained by summing the intensities of each map row. In the double-chain layer position (red and green arrows), both the Cu and O signals are observed to be lower than in the single-chain layer positions. This confirms that both the Cu and O content is lower in the Cu-O double-chain layer than in the Cu-O single layer.

DFT estimated the stability of different vacancy configurations by comparing their formation energies at 0 K. A supercell structure composed by a $Y_2Ba_4Cu_8O_{16}$ (Y248) stoichiometry containing Cu-O double-chain layers

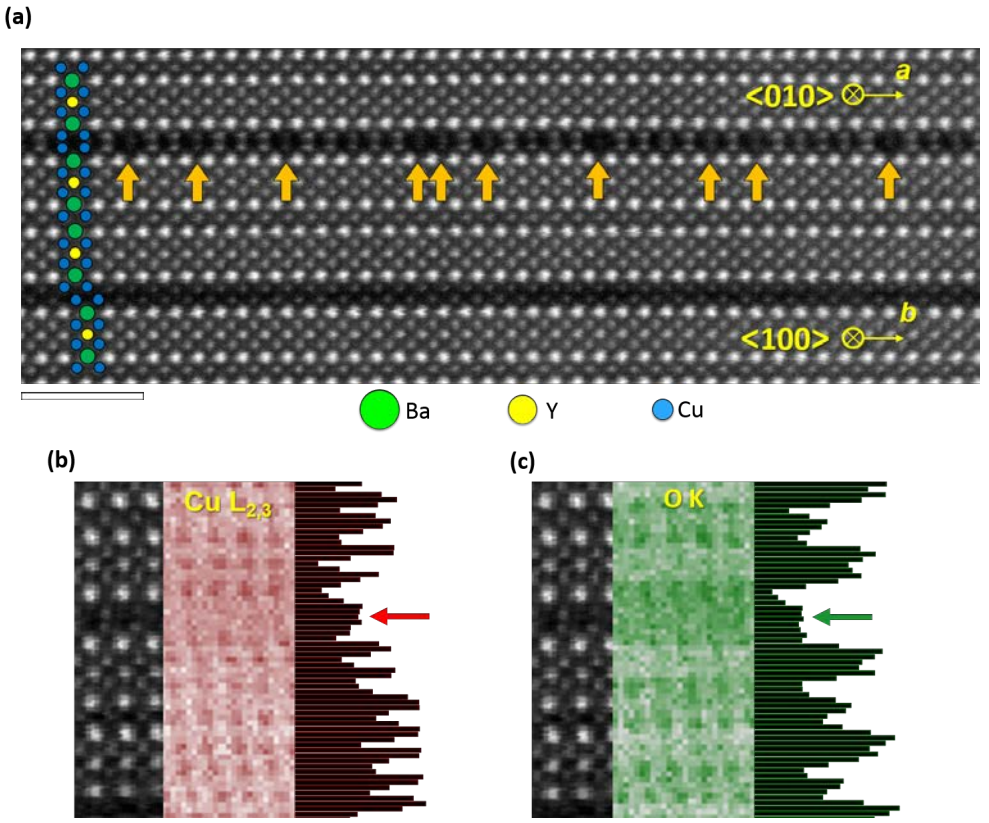

Figure 3.21: (a) Z-contrast image of two Y124 intergrowths viewed along the <010> (upper defect) and <100> (lower defect) zone-axes. The arrows point to Cu sites containing V_{Cu}. The Ba, Y and Cu atomic columns are represented with green, yellow and blue circles, respectively. Scale bar: 20nm. (b) Cu (red) and (c) O (green) EELS compositional maps. Each image displays, from left to right, the ADF simultaneous image, the EELS compositional map and the averaged signal profile. The arrows point to the Y124 intergrowth position.

instead of Cu-O single chains was used [83], which is represented in Fig. 4.9 (a). The more relevant values obtained from the DFT-calculations are summarized in the table of Fig. 4.9 (b).

The most favorable configuration corresponds to the case where one Cu

(a)

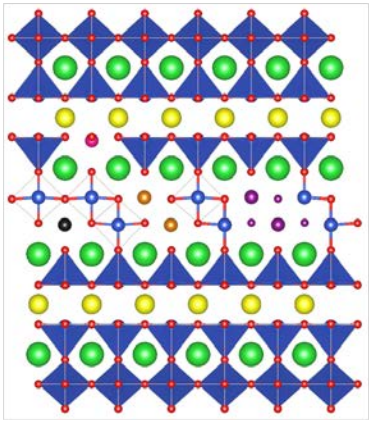

(b)

	Defect	Crystallographic position	Formation energy (eV)
●	V_{Cu}	Superconductor plane	1.40
●	V_{Cu}	Double-chain layer	2.11
●	$2\ V_{Cu}$	Double-chain layer	2.47
●	$2\ V_{Cu} + 3\ V_O$	Double chain layer	1.13

Figure 3.22: (a) Illustration of the Y248 crystal structure. The pink, orange, black and magenta circles indicate the crystallographic sites where the V_{Cu} have been tested in the DFT-calculations. The Ba, Y, Cu and O atomic columns are represented with green, yellow, blue and red circles, respectively. (b) Formation energy values associated to the specific vacancy configuration represented in (a) at O K

vacancy is introduced within the superconducting plane, with an associated formation energy value of 1.4 eV per Cu atom (at 0 K). This theoretical result is at odds with the experimental observation where pairs of Cu vacancies are identified within the Y124 intergrowth, which indeed corresponds to the configuration with a largest formation energy, 2.47 eV per Cu atom. This energy is even higher than the one obtained when a single V_{Cu} is placed within the Y124 intergrowth, with a value of 2.11 eV per Cu atom. This controversy is solved when additional oxygen vacancies decorate the pairs of Cu vacancies. Indeed, the formation energy shifts from 2.4 eV to 1.4 eV when the two Cu vacancies are decorated with three extra V_O in a specific geometry, being two of them located within the lower Cu-O double-chain plane and the other one within the

upper Cu-O double-chain plane. Notice that the oxygen signal that is measured in the corresponding compositional map of Fig. 3.21 (c), is also lower in the Cu-O double-chain layer than in the Cu-O single-chain position, which signals that a lower O content is present within the Y124 intergrowth defect. DFT also permits to calculate how the structure relax when we introduce this complex defect configuration within the double-chain layer. In particular, we have introduced a 50% of defects within the upper double-chain layer of the simulated Y248 structure in a periodic and alternating manner along the [110] direction. In order to compare both the DFT-simulated structure and the experimental one, we have simultaneously acquired Z-contrast and ABF images, which are shown in Fig. 3.23 (a) and (b), respectively.

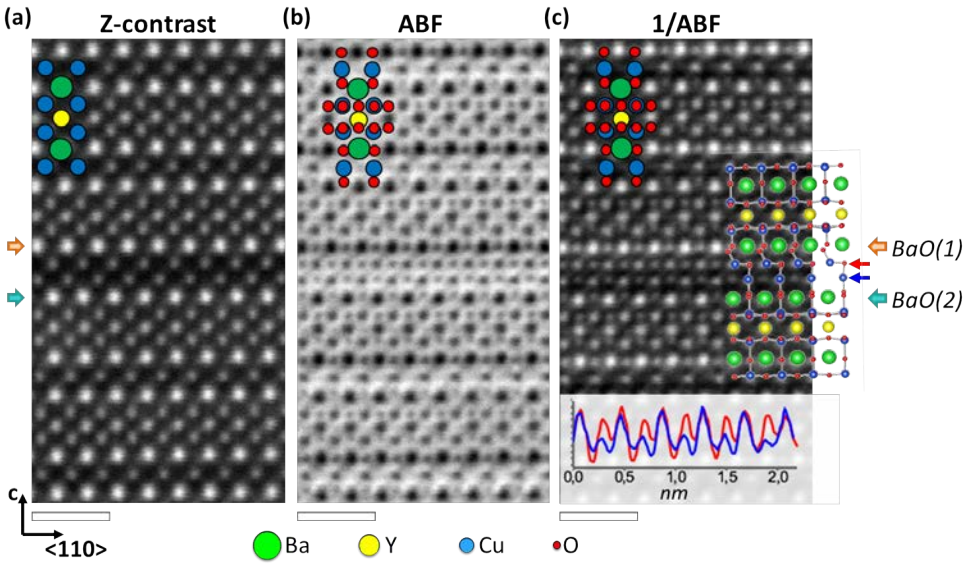

Figure 3.23: (a) Z-contrast, (b) ABF and (d) contrast-inverted ABF images of an isolated Y124 intergrowth viewed along the <100> zone-axis. The DFT-simulated structure is superimposed in (d). The inset shows two horizontal intensity profiles measured along the upper (red) and lower (blue) Cu-O double-chain planes. The Ba, Y, Cu and O atomic columns are represented with green, yellow, blue and red circles, respectively. Scale bars: 10 nm.

In order to view all the atomic sub-lattices more clearly, we have inverted

the contrast of the ABF image, as shown in Fig. 3.23 (c). Both the ABF and the Z-contrast images are acquired simultaneously from the same crystal region where one isolated Y124 intergrowth is present, which is placed at the center of the image. The observed structural shift, on either side of the fault, indicates that the crystal is viewed along the <100> zone-axis. The DFT-simulated and real structures are compared in Fig. 3.23 (c) by superimposing the DFT-structure onto the contrast-inverted ABF image. A good matching between both structures is observed. The relative O content within both Cu-O planes of the Y124 intergrowth are compared by tracing horizontal intensity profiles, see inset of Fig. 3.23 (c). Taking the Cu signal as a reference for normalization, it is clearly observed that the oxygen sites belonging to the lower Cu-O double-chain plane have a lower intensity value than those located within the upper Cu-O double-chain plane (blue profile). This result confirms that larger amount of V_O are located in the lower Cu-O double-chain plane, as predicted by the DFT.

3.3.2 Oxygen vacancies within the BaO planes

Notice that in the contrast-inverted ABF image (Fig. 3.23 (c)) the O columns located within the BaO plane that is placed above the fault (orange arrow), *BaO(1)*, appear brighter than those belonging to the lower BaO plane (green arrow), *BaO(2)*. From the two BaO planes that are present within the same Y123 unit cell, the BaO(1) plane corresponds to the one placed closer to the film surface. The contrast difference between the BaO(1) and BaO(2) planes evidences that some V_O are present within the BaO(2) planes. A lower magnification Z-contrast, ABF and contrast-inverted ABF images of a central region belonging to a YBCO thin film, with three Y124 intergrowths (blue arrows), are displayed in Fig. 3.24 (a-c), respectively. Notice that the same contrast difference is observed in all the viewed BaO(1) and BaO(2) planes adjoining one Y124 intergrowth defect. We have traced horizontal intensity profiles along the BaO planes that are located above (red profile) and below (green profile) one of the Y124 intergrowths, which are displayed in the inset of the Fig. 3.24 (c). Using the Ba signal for normalization, it is confirmed that the O atoms placed within the upper BaO plane (BaO(1)) appear brighter than those located within the lower one (BaO(2)). Besides, this contrast-asymmetry, generated at the BaO planes, is not exclusive from

the cells adjoining the faults, but it is repeated in all the viewed Y123 cells, forming a periodical and uneven pattern that is transferred along the *c*-axis direction.

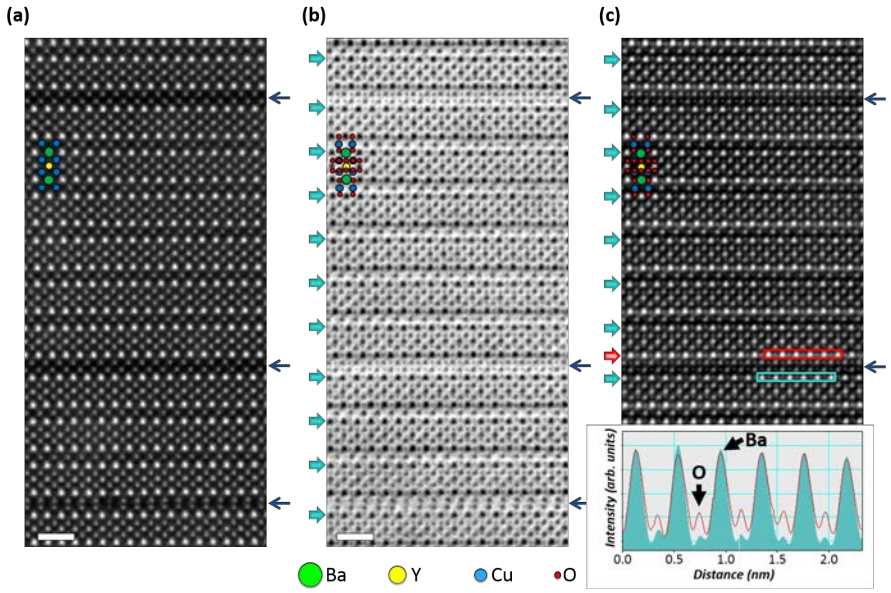

Figure 3.24: (a) Z-contrast, (b) ABF and (c) contrast-inverted ABF images of a YBCO crystal region with three separated Y124 intergrowths (blue arrows). The inset of (d) shows two horizontal intensity profiles measured along the BaO(1) (red) and BaO(2) (green) planes. The Ba, Y, Cu and O atomic columns are represented with green, yellow, blue and red circles, respectively. Scale bars: 10 nm.

The lower O intensity that is observed in the the BaO(2) planes (blue arrows) is ascribed to the presence of additional oxygen vacancies ($V_O^{BaO(2)}$). This observation is relevant as it is the first time that the $V_O^{BaO(2)}$ are experimentally observed in YBCO. Although it is widely accepted in the scientific community that the V_O are only generated within the Cu-O planes of the chain layers in YBCO [39, 89, 90], some early works already mentioned the possibility that a slight percentage of V_O (<10%) might be also present within the apical site positions, this is at the BaO planes [89, 91]. However, these apical vacancies were never observed experimentally. Besides, all of these

early studies were based on the study of YBCO bulk crystals, which have a different microstructure that the YBCO thin films. At this point, many questions arise regarding the formation of these $V_O^{BaO(2)}$. Are the $V_O^{BaO(2)}$ only generated in the case of CSD-derived YBCO films? Do they have a correlation with the appearance of Y124 intergrowths? Has the YBCO fabrication process anything to do with their formation? Does the substrate have any influence on their generation? Which is the driving force that govern the emergence of this defect? Surprisingly, we found an answer for most of these questions when we studied the microstructure of a YBCO single crystal sample. Fig. 3.25 (a) shows a low magnification Z-contrast image of the studied YBCO single crystal sample.

The image contrast is observed to be homogeneous within the single crystal core, which signals the presence of a pure Y123 crystal lattice, without Y124 intergrowths or any other crystalline defect. Surprisingly, the darker contrast identified at the crystal surface, generated by dark stripes running along the basal direction, indicates that significant amount of Y124 intergrowths are present there. We have acquired high resolution Z-contrast and ABF images at the single crystal core (orange square) and surface (green square) areas to compare the YBCO crystal structure between these regions and to study the presence of $V_O^{BaO(2)}$ in both regions. Fig. 3.25 (b) and (c) display the obtained Z-contrast and contrast-inverted ABF images of the crystal surface (green rectangle) and the core region (orange rectangle), respectively, being the central crystal area far from the influence of the Y124 intergrowths. As before, we have traced horizontal intensity profiles, which are normalized at the Ba maximum, along the BaO(1) (red profile) and BaO(2) planes (green profile) in both contrast-inverted ABF images, which are shown in Fig. 3.25 (e) and (f), respectively. Near the crystal surface (green squared region), where some Y124 intergrowths are present, the O columns located within the BaO(1) plane (red profile) appear brighter than those placed within the BaO(2) plane (green profile), as in the YBCO thin films. Otherwise, in the central region of the crystal, identical profiles are obtained from both the BaO(1) and BaO(2) planes. This finding evidences that the $V_O^{BaO(2)}$ are also present in bulk single crystals and that their formation is linked to the presence of the Y124 intergrowth defect, regardless of the YBCO fabrication process.

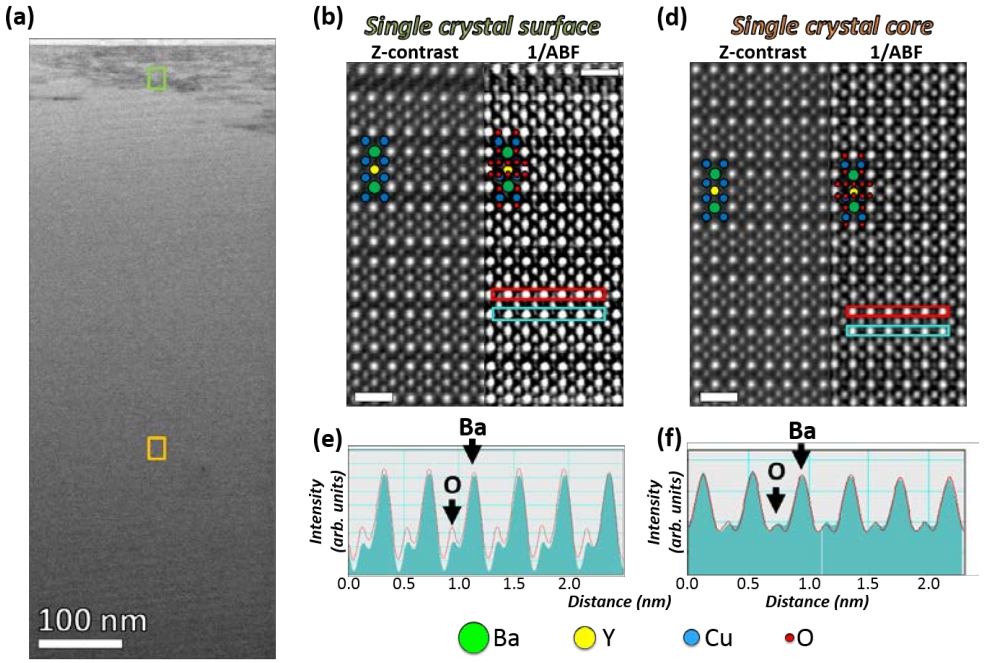

Figure 3.25: (a) Low-magnification Z-contrast image of a YBCO single crystal sample. The red and orange rectangles indicate the areas where the images shown in (b) and (d) are acquired. (b) Z-contrast and contrast-inverted ABF images of the YBCO crystal at the single crystal surface and (d) central region. The inset of (b) and (c) show the horizontal intensity profile measured at the BaO(1) (red) and BaO(2) (green) planes). The Ba, Y, Cu and O atomic columns are represented with green, yellow, blue and red circles, respectively. Scale bars: 10nm

Are the $V_O^{BaO(2)}$ only generated in the case of CSD-derived YBCO films and has the YBCO fabrication process anything to do with their formation? No, the generation of $V_O^{BaO(2)}$ have been observed in YBCO single crystals, and in sputtering-derived samples (images of which are not included in this thesis). Are they correlated with the appearance of Y124 intergrowths? Absolutely, the presence of $V_O^{BaO(2)}$ has only been identified around the Y124 intergrowth defects and not far of their influence. Does the substrate have any influence on their generation? No, these results show as well that the formation of V_O within the BaO(2) planes has nothing to do with the substrate mismatch, but

might be related to the strain accommodation that is needed when a Y124 intergrowth is embedded within the Y123 crystal lattice, as a result of the cell expansion resulting from the incorporation of an extra Cu-O plane, as it will be shown below. In addition, the fact that we have only observed V_O in the BaO(2) planes, and not in the BaO(1) planes, might be a consequence of the YBCO growing direction.

We have further studied the stability of placing one V_O at different crystallographic positions of the Y123 structure. As before, we have used DFT-calculations to estimate the formation energy of creating a V_O at different crystallographic positions. In this case, we have used a supercell structure composed by a Y123 unit cell structure, which is repeated two times along the three crystallographic axes. The obtained values are shown in the table 3.1. As expected, the most favorable configuration correspond to the case where a V_O is introduced within the Cu-O single-chain plane, with a formation energy value of 1.11 eV per oxygen atom. However, creating an V_O within the BaO plane only costs 1.13 eV per oxygen atom, which is only 0.02 eV higher than the former case. This means that the energy needed to introduce one oxygen vacancy either within the BaO plane or CuO chain layer is almost the same and therefore, the stability of both configurations is similar. Otherwise, the formation energy increases when the V_O is placed within the superconducting planes, which are always observed to be fully oxygenated. This theoretical calculations match well with the experimental observation of having V_O within the BaO(2) planes.

Defect	**Crystallographic position**	**Formation energy (eV)**	**c-parameter (Å) (2xY123 unit cells)**
V_O	Chain layer	1.11	23.674
V_O	BaO plane	1.13	23.632
V_O	Sup. plane (a-axis)	1.62	23.606
V_O	Sup. plane (b-axis)	1.59	23.603

Table 3.1: Formation energy and supercell c-parameter associated to the introduction of one V_O within the different crystallographic positions of the Y123 phase at 0 K.

From the previously considered questions, the only one that still remains unanswered is: Which is the driving force that govern the emergence of this defect? We expect that the mechanism ruling the formation of $V_O^{BaO(2)}$ has to be linked to the presence of the Y124 intergrowths because, as previously commented, both defects appear together. If we look at the third column of table 3.1, we can see that the theoretical c-parameter of the simulated supercell structure is slightly lowered when the V_O is introduced within the BaO plane. Taking this in mind and that an additional Cu-O plane is introduced within the

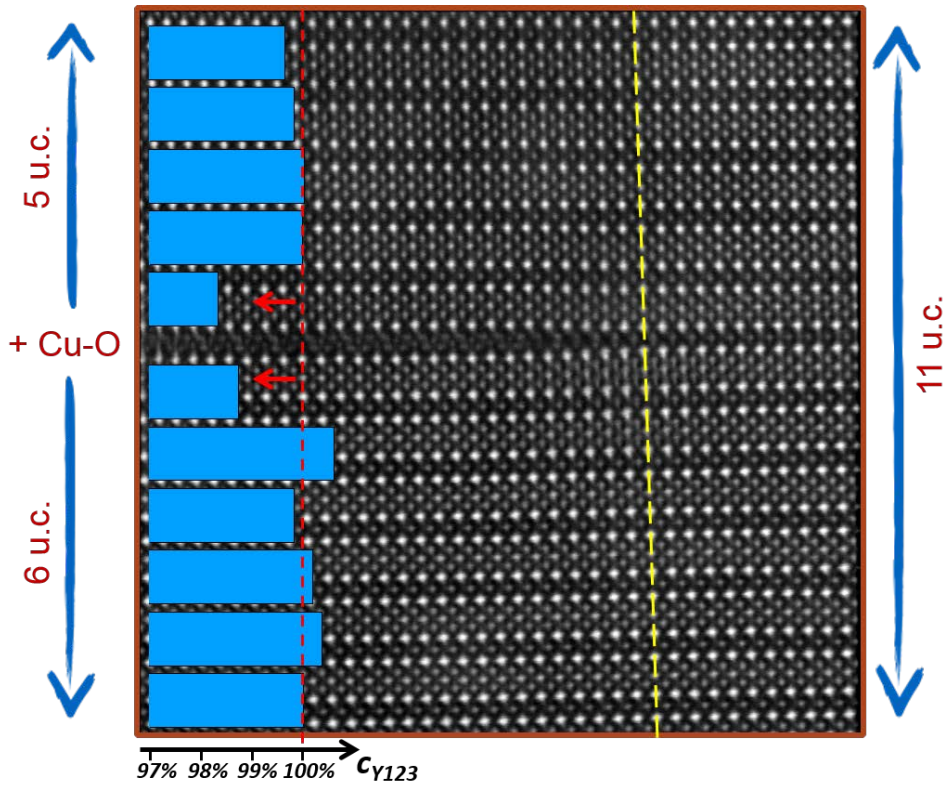

Figure 3.26: Z-contrast image of a YBCO crystal region containing an isolated Y124 intergrowth placed at the left-side of the image. Blue bars indicate the YBCO c-parameter at each YBCO unit cell. The dashed red line indicates the measured YBCO c-parameter far from the viewed Y124 intergrowth. The dashed yellow line separates the two viewed YBCO regions, which contains or not the Y124 intergrowth.

Y123 structure, thus expanding the Y123 structure along the *c*-axis direction, one can argue that the system generates $V_O^{BaO(2)}$ in order to compress the cell.

Fig. 3.26 displays a Z-contrast image of an isolated Y124 intergrowth, which is trapped within the Y123 crystal lattice. Eleven Y123 unit cells are viewed at the right side of the image whereas eleven unit cells plus one Cu-O plane is identified at its left side. As those BaO planes that are located at the upper and lower image edges are not bended, we can conclude that the YBCO crystal needs approximately 11 unit cells to accommodate the observed expansion [22]. One structural mechanism that might favor this lattice compression is the introduction of V_O within the BaO(2) planes. By measuring the Ba-Y interatomic spacings along the *c*-axis direction, we can estimate the c-parameter of the viewed Y123 unit cells, which is represented in Fig. 3.26 as blue bars that are superimposed onto the Z-contrast image. As we do not have any reference area, we have normalized the obtained values to those Y123 cells located as far as possible from the planar defect. Clearly, those Y123 unit cells located close to the Y124 intergrowth are more compressed probably due to a large concentration of $V_O^{BaO(2)}$.

3.3.3 Additional structural distortions

A closer look at the Z-contrast and contrast-inverted ABF images, permits us to identify the structural distortions stemming from the presence of the $V_O^{BaO(2)}$. Fig. 3.27 (a) shows a high resolution Z-contrast image of the YBCO crystal with an isolated Y124 intergrowth defect obtained from a YBCO thin film. The area delimited by the red square is magnified and displayed in Fig. 3.27 (b). By using a center-of-mass refinement process we are able to identify the coordinates of all the central positions of the viewed atomic columns [92], obtaining a set of coordinates for each atomic sub-lattice. Afterwards, we are able to map and quantify all the atomic shifts or interatomic spacings that are viewed in the images.

We have started by measuring how the presence of $V_O^{BaO(2)}$ distort the heavier cation sub-lattices. Firstly, we have observed that the c-spacing between the Y and its upper Ba cation (green arrows) ($\delta_{Y-Ba(2)}$ spacing) is reduced a relative value of 1.5% (taking as a reference the canonic Y123

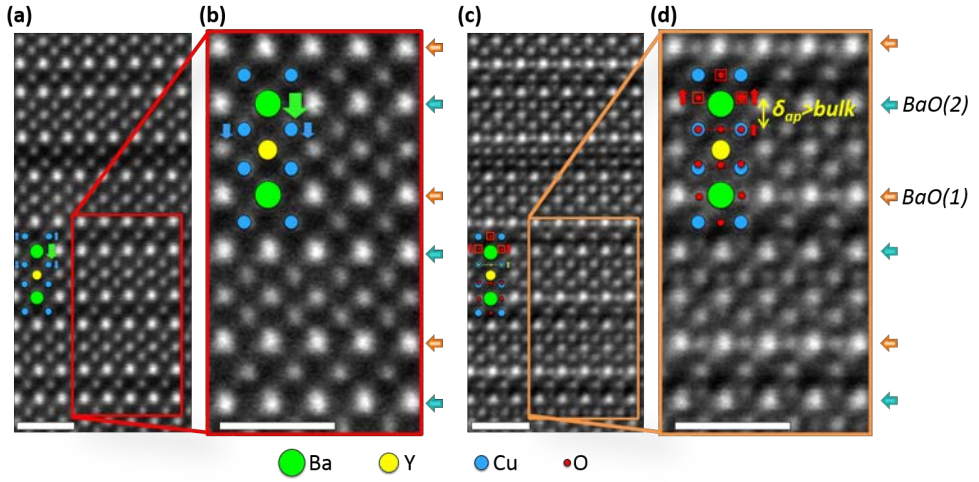

Figure 3.27: High resolution (a) Z-contrast and (c) contrast-inverted ABF images of a Y123 crystal region containing one Y124 intergrowth. The red and orange rectangular areas are magnified in (b) and (d), respectively. The Ba, Y, Cu and O atomic columns are represented with green, yellow, blue and red circles, respectively. The Ba, Cu and O shifts, occurring around the Y124 intergrowth, are represented with green, blue and red arrows, respectively. Scale bars: 10nm.

structure from Ref. [39]), *i.e.*, the Ba cations placed at the BaO(2) planes are shifted downwards. Secondly, we have identified that the Cu atoms belonging to the upper superconducting planes, from now on referred to as Sup_U, are also shifted downwards, being them located closer to its lower Y cation. Consequently, the spacing between the superconducting planes (δ_{sup}) is narrowed a 5.3% and the spacing between the Sup_U and its nearest chain layer (Sup_U-Ch) is enlarged a 4.3%. It has to be mentioned that these Ba- and Cu-spacings have been normalized to the BaO(1)-Y and Ch-Sup_D spacings, respectively, where Sup_D refers to the lower superconducting plane,as the used images do not contain a non-distorted reference area. This methodology is reasonable as no relevant distortions are observed within the lower-half-Y123 unit cell structure, where no V_O are present. Besides, this has been further confirmed by simulating, with DFT-calculations, a Y248 structure containing $V_O^{BaO(2)}$ in one of its BaO(2) planes, see Fig. 3.28. In the DFT-simulated structure, those perovskite blocks that do not contain $V_O^{BaO(2)}$ are not substantially distorted.

All of the measured distortions are indicated with green (Ba) and blue (Cu) arrows in the Z-contrast images of Fig. 3.27 (a) and (b).

We have also studied the emerging distortions regarding the oxygen sub-lattice, which is imaged in the contrast-inverted ABF image of Fig. 3.27 (c). The orange squared area of Fig. 3.27 (c) is shown, with a higher magnification, in Fig. 3.27 (d). Notice that the oxygen atoms located at the BaO(1) planes appear clearly brighter than those located at the BaO(2) planes due to the presence of the $V_O^{BaO(2)}$. Besides, the aforementioned distortions occurring at the heavier cations sub-lattices can also be identified in this contrast-inverted ABF image.

It is worth remembering that the oxygen atoms placed at the superconducting planes are shifted towards the Y cation, forming a rippling pattern with their neighboring Cu cations. This rippling is clearly identified in the Sup_D planes forming a Cu-O-Cu angle value of 165±2°, which coincides with the reference value [39]. However, this buckling almost disappears at the Sup_U plane. The measured Cu-O-Cu angle value in this case is 176±2°. Besides, the apical oxygens located at the the BaO(2) planes (red squares), those containing V_O, are shifted upwards. As a result of this shift, the spacing between the superconducting plane and its nearest apical oxygen (from now on δ_{ap}) is a (8±3)% greater in the Sup_U planes compared to the Sup_D ones.

Using DFT-calculations, we have simulated the relaxed Y248 structure containing a 50% of $V_O^{BaO(2)}$ in one of its BaO(2) planes in a periodic and alternated manner along the [110] direction, see Fig. 3.28. Similar distortions that those observed experimentally have been also identified in this DFT-simulated structure, showing good agreement. In particular, the Y-Ba(2) and δ_{sup} spacings are reduced a 0.9% and 4.9%, respectively, while the Sup_U-Ch spacing is enlarged a 1.8%. This latter distortion is the one showing a major discrepancy with the experimental results as the Sup_U-Ch spacing is observed to be larger in the experimental structure (4.3%) than in the simulated one (1.8%). However, this discrepancy might arise due to the fact that we have simulated a Y248 instead of a Y123 structure and that we do not know the density of $V_O^{BaO(2)}$ at each BaO(2) plane. Regarding the oxygen sub-lattice,

the Cu-O-Cu angle is also preserved in the Sup_D planes, with a Cu-O-Cu value of 165°, whereas it is enlarged a value of 177° within the Sup_U planes, showing good agreement with the experimental observation. Finally, the δ_{ap} spacing of the simulated Y248-structure is also higher in the Sup_U plane compared the Sup_D one, although the observed enlargement (1.3%) is lower than the experimental measure (8%).

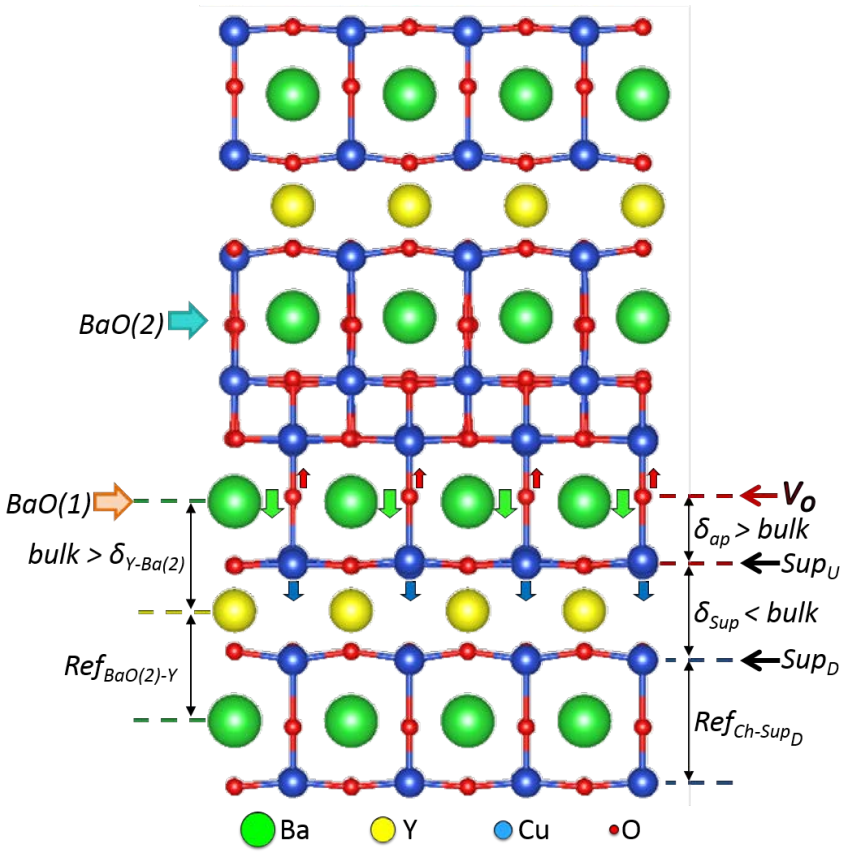

Figure 3.28: (a) Illustration of the DFT-simulated Y248 structure containing a 50% of V_O within the BaO(2) plane (orange arrow). The observed atomic shifts are represented with arrows. The Ba, Y, Cu and O atomic columns are represented with green, yellow, blue and red circles, respectively. Scale bars: 10nm.

The described distortions modify the atomic bondings between the superconducting Cu and their tetrahedrally coordinated oxygens. Therefore, we expect changes on the YBCO electronic configuration and therefore, on the YBCO physical properties as well. For instance, larger T_C values (up to 130K) are measured in Hg-based cuprates, where the buckling angle in the superconducting planes is around 180° [41, 93]. Besides, increasing the δ_{ap} parameter might also influence the transfer of carriers between planes and chains as their hopping amplitude depends on this interatomic spacing.

In order to investigate how the described distortions modify the electronic configuration of the YBCO superconductor at room temperature, we have performed Energy-loss near-edge spectroscopy (ELNES). The ELNES spectrum gives information about the energy that the transmitted electrons loose when they interact with the core electrons of the crystal and therefore, it provides information about the electronic states that remain empty. Besides, by using simultaneously the ADF detector and the EEL spectrometer we are able to associate each EEL spectrum to an image pixel, which permits to map all the spectral variations within a Z-contrast image.

3.3.4 ELNES spectroscopy

In the dipole approximation, the O K near-edge structure arises from the excitations of the O *1s*-electrons to the O *2p*-bands, whereas the Cu L edge result from the excitation of the *2p*-electrons into the empty bound states [15]. In perovskites, the O *2p*- and Cu *3d*-bands are strongly hybridized, as they have similar energies, being both of them located close to the Fermi level. For these reasons, significant spectral modifications are expected, in both edges, for slight variations of the band occupancy or the electronic levels.

For instance, the onset of the O K edge pre-peak is observed to shift to higher energies when lowering the O content of the YBCO structure [94, 95]. Accordingly, the pre-peak of the O K edge structure provides information about the electron density at each specific YBCO crystallographic position. Besides, the Cu oxidation state can be extracted from the Cu L_{23} edge structure as its onset shifts towards higher energies when the Cu oxidation state is reduced.

Fig. 3.29 (a) shows a high magnification Z-contrast image of the YBCO crystal from a thin film sample, where the O K edge structure has been

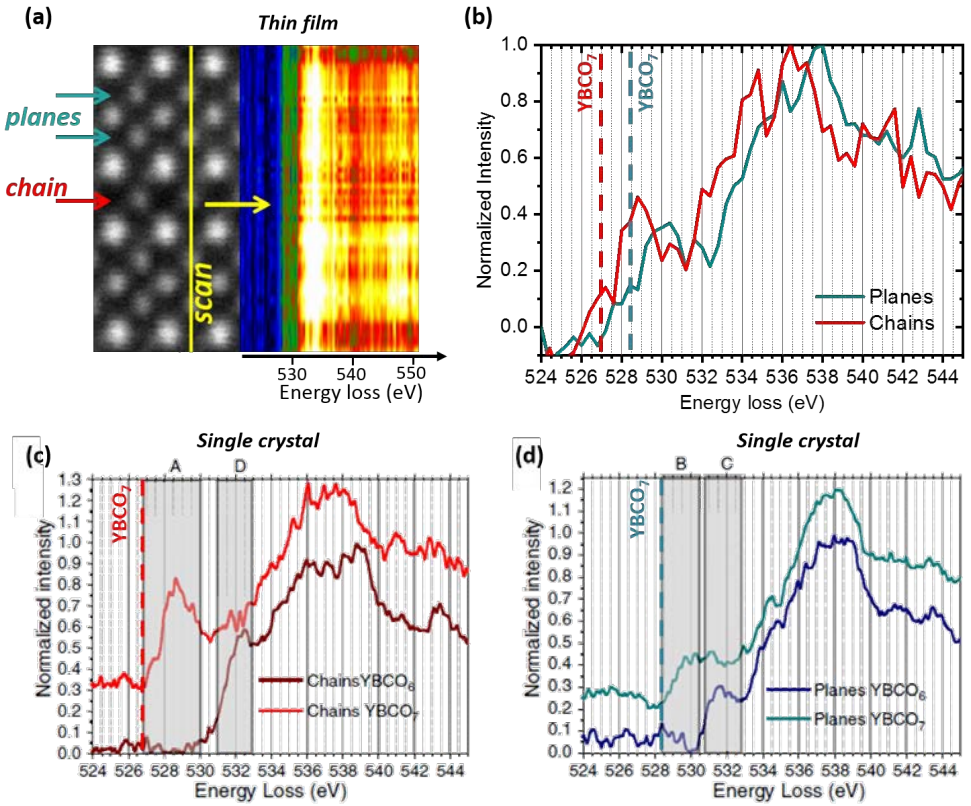

Figure 3.29: (a) Z-contrast image of the YBCO crystal lattice and the ELNES O K edge spectra obtained from the vertical scan indicated by the yellow line. The intensity of the ELNES spectra is represented with a temperature scale. The superconducting and single-chain layer planes are indicated with green and red arrows, respectively. (b) ELNES O K edge associated to the chain (red line) and superconducting plane (green line) positions. The red and green dashed lines indicate the energy values of the O K pre-peak onset positions in chain and plane, respectively, from an optimally doped $YBCO_7$ structure. (c) Comparison of the ELNES O K edge structures between a doped and an under-doped YBCO single crystals in chains and (d) planes, respectively. Fig. (c) and (d) are extracted from [94].

acquired along the yellow vertical scan. The O K edge structure is observed to vary as we move along the *c*-axis direction. The specific O K edge fine-structures associated to the CuO chains (red line) and CuO_2 superconducting planes (green line) are displayed in Fig. 3.29 (b). The statistical noise of each spectrum is reduced by adding up several spectra from equivalent atomic sites and by using the PCA filter [26, 96].

The O K edge fine-structures in the superconducting plane and chain positions are clearly different, being the onset of the O K pre-peak located at the 538.5 eV and 527 eV positions, respectively. We have used the spectra shown in Ref. [94] as a reference for comparison, which are obtained from YBCO single crystals. The authors compare the O K edge fine-structure between an under-doped $YBa_2Cu_3O_{6.03}$ ($YBCO_6$) and an optimally-doped $YBa_2Cu_3O_{6.97}$ ($YBCO_7$) single crystals at the chain layers, see Fig. 3.29 (c), and superconducting planes, see Fig. 3.29 (d). Notice that the achieved energy and spatial resolution and signal-to-noise ratio in our ELNES spectra and in the ones from the single crystal samples are similar. In the single crystal, the O K pre-peak onset depends on the oxygen content, being located at lower energy positions for larger oxygen concentrations. In particular, the O K pre-peak onset of the optimally doped YBCO crystal ($YBCO_7$) is placed at the 527 eV position in the chains and at the 528.5 eV position in the planes, as in our experimental observation. This result confirms that our YBCO thin films has the optimal oxygen concentration ($YBCO_{6.97}$).

We have carried out the same analysis using the Cu $L_{2,3}$ near-edge structure. Fig. 3.30 (a) displays a Z-contrast image of the YBCO crystal belonging to the thin film sample with the measured Cu L edge vertical scan. The obtained Cu L fine-structures associated to the specific chain (green) and plane (red) positions are displayed in Fig. 3.30 (b). As in the O K edge, the observed Cu L edge fine-structures are found to be different at both crystallographic sites. At the chains, the L_3 peak splits into the α and β peaks, centered at 931.5 eV and 934 eV, respectively. A chemical shift towards higher energies is observed in the Cu L edge when the Cu oxidation state is reduced. This is the reason why the α peak is associated to a Cu oxidation state of (+2) whereas the β peak refers to (+1). Therefore, the splitting of the L_3 suggests

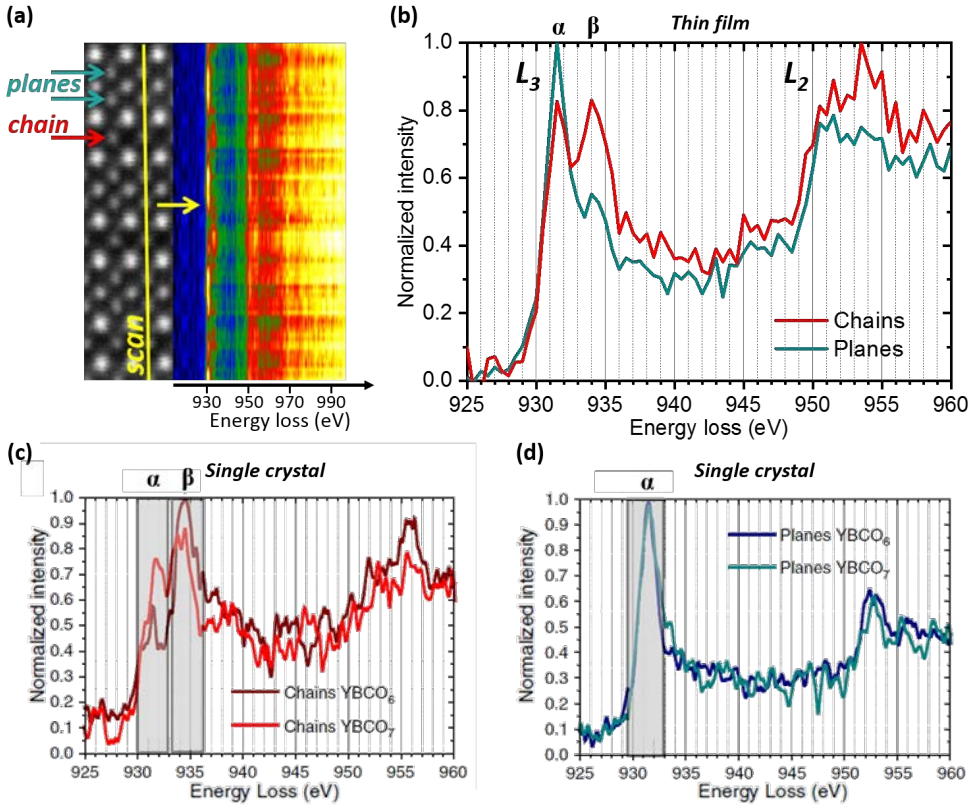

Figure 3.30: (a) Z-contrast image of the YBCO crystal lattice and the ELNES Cu L edge spectra obtained from the vertical scan indicated by the yellow line. The intensity of the ELNES spectra is represented with a temperature scale. The superconducting and single-chain layer planes are indicated with green and red arrows, respectively. (b) ELNES Cu L edges associated to the chain (red line) and superconducting plane (green line) positions. (c) Comparison of the ELNES Cu L edge structures between a doped and an under-doped YBCO single crystals in chains and (d) planes, respectively. Fig. (c) and (d) are extracted from [94].

that a mixture of $Cu^{+1/+2}$ cations is present within the single-chain layers. However, the Cu-O bonds in YBCO might be different than those from CuO or Cu_2O compounds and therefore, the observed Cu L EELS fine-structure in YBCO might also differ from these copper oxides compounds. In the chain positions, the α/β ratio can be also related to the oxygen concentration

of the YBCO structure as the O^{2-} anions located at the chain layers take electrons from their neighboring Cu cations, thus changing their valence from Cu^{+1} to Cu^{+2} [90, 97, 98]. Otherwise, the L_3 peak associated to the superconducting Cu cations is mainly composed by the α peak, which signals that the superconducting Cu have an oxidation state value of Cu^{+2} and that the hole carriers are well confined within the superconducting planes.

We have compared our Cu L fine-structures with the ones obtained at the chain and plane positions from YBCO single crystals, see Fig. 3.30 (c) and (d), respectively [94]. As before, we have obtained similar Cu L edge fine-structures at both the plane and chain positions than those reported from $YBCO_7$ single crystal samples [94].

We have further studied how the previously described distortions, found around the Y124 intergrowth defect, modify the ELNES O K and Cu L fine-structures. First of all, we have compared the Cu L edge structure obtained at different crystallographic sites of the double-chain layer, see Fig. 3.31 (a). The obtained spectra matches well with the previously shown Cu L edge from the single-layer site, also shown in this plot as an orange spectrum. Besides, we are not able to distinguish significant spectral variations when moving along the basal direction.

Secondly, we have compared the fine-structure of the O K edge between the distinct oxygen apical positions, this are the BaO(2) (with the V_O) and the BaO(1) planes. The obtained spectra are shown in Fig. 3.31 (b). As commented, the emergence of the pre-peak is related to the hybridization between the O and the Cu orbitals. The presence of V_O lead to a higher amount of electrons and a lower amount of unoccupied states in the O *2p*-band. Therefore, the presence of V_O in these sites diminishes the pre-peak intensity.

We have also compared the O K edge structures associated to the Sup_U (red line) and Sup_D (black line) superconducting planes, which are shown in Fig. 3.31 (c). The O K pre-peak onset is placed at the same energy position. However, the pre-peak intensity is lowered in the upper superconducting plane (red line), where the Cu-O-Cu bond angle and the δ_{ap} spacing are enlarged

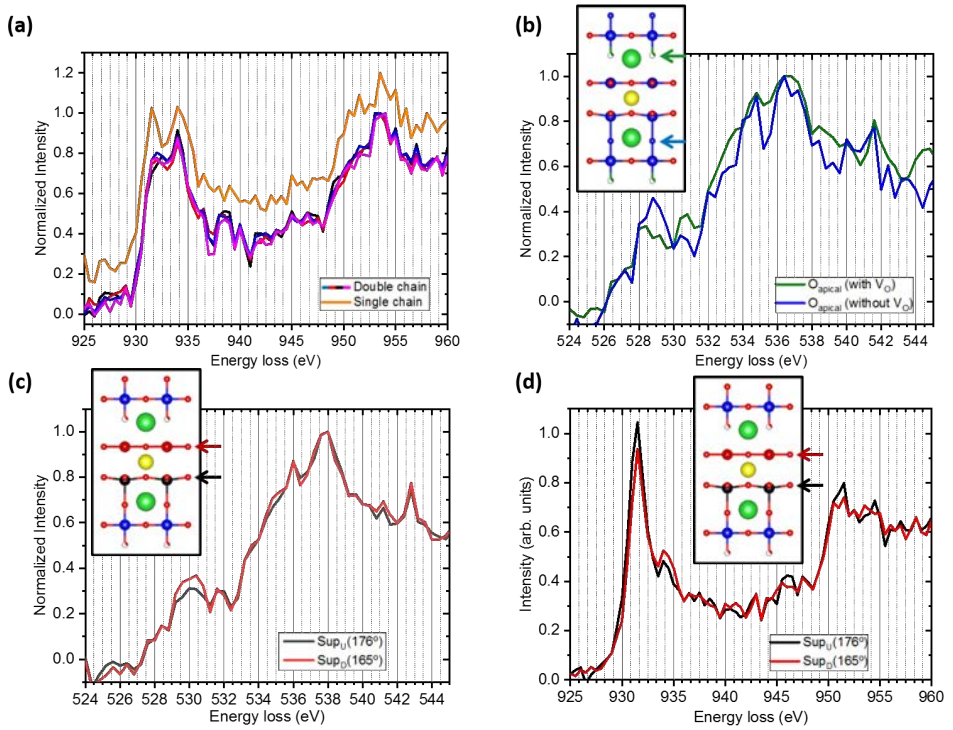

Figure 3.31: (a) ELNES Cu L edge fine-structure of the Cu-O single-chain layer (orange line) and equivalent crystallographic sites from the same Y124 intergrowth defect. Each color line correspond to a different spectrum obtained from equivalent Cu sites within the same defect. (b) Comparison of the ELNES O K edge spectra between the BaO(2) (black line) and BaO(1) (red line) apical sites and (c) between the upper (black line) and lower (red line) superconducting planes. (d) Comparison of the ELNES Cu L edge spectra between the upper (black line) and lower (red line) superconducting planes. The insets illustrate the distorted YBCO structure with the arrows pointing to the crystallographic sites where the EEL spectra were acquired.

respect the lower one, which suggests that more electrons are confined at the upper plane.

Finally, we have also studied the Cu L edge fine structures of both planes, displayed in black (Sup_U) and red (Sup_D) in Fig. 3.31 (d). The observed α/β ratio is slightly larger in the Sup_U plane than in the Sup_D one. The observed

changes are associated to the enlargement of the Cu-O-Cu bond angle towards 180° in the Sup_U plane. The concomitant enlargement of the δ_{ap} spacing might also contribute to the change of the Cu L edge fine-structure. Theoretical calculations are planned to understand the observed changes in the electronic structure.

3.3.5 Summary

In the second part of this first chapter we have described the *real* structure of the Y124 intergrowth defect, which is the most common defect found in YBCO thin films, stemming from the incorporation of an extra CuO chain plane between the Ba cations forming the double-chain layer, and all the concomitant distortions emerging around it. Our results and assessments apply to all YBCO thin films, regardless of the used YBCO growing process.

First, we have shown that the Y123 stoichiometry is preserved within the Y124 structure thanks to the spontaneous creation of a complex vacancy cluster configuration composed by oxygen decorated Cu di-vacancies, which are ordered along the *b*-axis direction The oxygen vacancies are also ordered, being two of them located at the lower double-chain plane and one at the upper plane. The stability of this particular vacancy configuration has been confirmed by the use of DFT-calculations.

We have also shown the occurrence of previously unforeseen V_O within the BaO(2) planes, in a periodic and uneven distribution along the *c*-axis direction, which are always found close to the Y124 intergrowths. The stability of this point defect has also been studied using DFT-calculations. We have linked the formation of V_O within the BaO(2) planes to the presence of Y124 intergrowths.

We have measured the atomic shifts appearing within the upper perovskite block of the Y123 unit cell, where the $\mathrm{V}_O^{BaO(2)}$ are placed. We have shown that the vertical symmetry of the Y123 unit cell is broken as a consequence of the emerging distortions. The more relevant observed distortions that might influence the YBCO physical properties are the enlargement of the spacing between the upper superconducting plane and its apical oxygen site

(δ_{ap} spacing) and the Cu-O-Cu buckling angle of the upper superconducting planes.

Finally, we have used ELNES spectroscopy to study the influence of all the observed distortions in the YBCO electronic configuration. In particular, we have studied how the Cu L and O K edge fine-structures vary at different Y123 crystallographic positions. We have observed some spectral changes respect the ones obtained from single crystal powder samples. Even though, we have made some correlations between the observed distortions and the spectral changes, further theoretical calculations should be carried out in order to fully understand the implications of the characterized structural modifications in the YBCO electronic configuration.

As the Y124 intergrowth constitutes one of the most common defects of the YBCO microstruture, being always present in YBCO films and single crystals (regardless of the fabrication process), we can anticipate that they will also contain V_O within the BaO planes and all of its associated distortions, which are not a particularity of the CSD-derived YBCO films. For this reason, it is mandatory to further investigate the implications of the observed structural distortions such as the increase of the Cu-O-Cu buckling angle and the δ_{ap} spacing on the YBCO superconducting properties, for instance by simulating the density of states of the distorted YBCO lattice by means of DFT.

Chapter 4

Strain accomodation mechanisms in epitaxial LNO and NNO thin films

4.1 Chapter preview

$RENiO_3$ oxides are a well known family of perovskite oxides that exhibit a tunable metal-insulator transition (MIT) and a resistive switching behavior [11, 99, 100]. The MIT temperature is observed to shift to higher temperatures when the RE ionic radius is decreased, due to a reduction of the Ni *3d*- and O *2p*-orbital overlapping. Yet, the RNO electrical properties can be further modified by inducing additional changes on the Ni-O bonds by means of the epitaxial strain [100–103]. Although this have been deeply investigated, it still remains unclear how these compounds accommodate the substrate mismatch when they are epitaxially grown onto single crystal substrates.

In this chapter we describe the lattice defects and the associated structural distortions appearing in $NdNiO_3$ and $LaNiO_3$ thin films. We have investigated the specific defect landscape present in both compounds when they are grown onto either LAO or $(LaAlO3)_{0.3}(Sr_2TaAlO_6)_{0.7}$ (LSAT) single crystal substrates, which imposes a tensile- and compressive-strain, respectively. We have used STEM-EELS to characterize the microstructure of each particular heterostructure and the subtle atomic distortions appearing around their preferential lattice defect, this is, the Ruddlesden-Popper fault (RPF). We have also measured the transport properties of the studied films, which have been then correlated with the observed microstructure in each case.

4.2 Introduction

$RENiO_3$ (RNO), where RE refers to a rare earth, have attracted major interest since it is one of the few oxide materials that present metallic conductivity at room temperature and an abrupt metal-to-insulator transition (MIT) for a certain temperature [2, 11, 99, 104]. These properties make these compounds very promising as elements for adaptive electronics [105–107]. Fig. 4.1 (a) displays the resistivity of different RNO crystals, with distinct RE species, as a function of the temperature. Both the resistivity and the MIT temperature are observed to increase with the atomic number of the used RE cation [99, 104]. This correlation arises because the rotations of the NiO_6 octahedra are more pronounced when the radius of the used RE cation is decreased, *i.e.*, the RE atomic number is increased, as illustrated in Fig. 4.1 (b). The fact of increasing the octahedral rotations lowers orbital overlapping between the *2p* O and *3d* Ni energetic levels and therefore, the system bandwidth [11, 99, 104]. Except the $LaNiO_3$ compound, which presents the maximum Ni-O-Ni bond angle (165°), all the other RNO compounds exhibit a MIT.

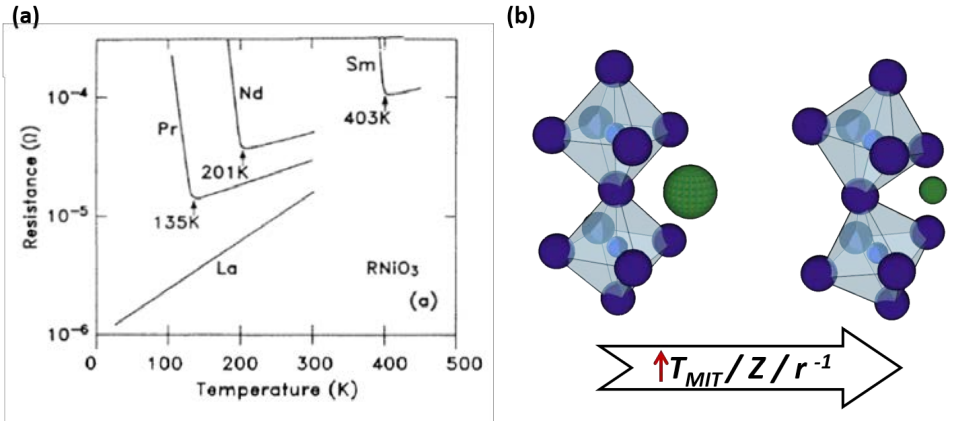

Figure 4.1: (a) Evolution of the resistivity with temperature for different RNO crystals, extracted from Ref. [99]. (b) Illustration showing the increase of the octahedral rotations when the RE radius is decreased.

Likewise, it is possible to induce changes in the RNO electronic properties by modifying the Ni-O bonds, for instance by epitaxial strain [11, 100–103, 108, 109] or hydrostatic pressures [110, 111]. Although it has been confirmed that these two mechanisms cause the MIT shifting to lower temperatures when the material is compressed, this effect is more pronounced when the distortions are generated by epitaxial strain [11, 101]. This is why high-quality epilayers grown on single crystal substrates are favored for fundamental studies and for proof-of-principle device work. However, it still remains unclear how the RNO films accommodate when they are epitaxially grown on different substrates. In this chapter, we have studied the appearing defects and distortions in tensile and compressive-strained $LaNiO_3$ (LNO) and $NdNiO_3$ (NNO) thin films by the use of STEM-EELS.

4.3 Fabrication process

NNO and LNO samples were prepared through a chemical solution deposition method. This process involves three steps: the synthesis of a precursor solution, a spin coating deposition and a final annealing process.

The precursor solutions are prepared by dissolving the metal salts $Ni(CH_3COO)_2$, $Nd(NO_3)_3$ and $La(NO_3)_3$ in methoxyethanol. The molar relationship between the Ni and the RE cations have to be 1:1. The solution is heated under reflux during 5 hours until a complete dissolution of the metal salts is reached, which is then filled up in a 5ml valued flask to achieve the desired final concentration of 0.2 M. The final layer thickness is tunned by diluting the 0.2 M (25 nm) solution down to 0.1 M (12.5 nm) or 0.05 M (6 nm) concentrations. The final solutions can be stored under argon, ensuring good stability for several months.

The solution is deposited following a spin coating route, where a 15 μl of the precursor solution is deposited onto the substrate surface, which is held on the spinner with a micropipette. Then the spinner rotates at 6000 rpm during 2 minutes and most of the solution is spilled out of the sample, thus ensuring a flat and homogeneous sol-gel. Afterwards, the sample is placed on a hot-plate at 70°C to dry the excess of solvent.

Afterwards, the films are set on an alumina crucible, placed within a quartz tube inside a tubular furnace. An specific thermal process is carried out in order to decompose the organic species and to grow the desired RNO phase. The samples are grown at a total pressure of 1 bar under a flux of oxygen of 0.12 l/min. Different thermal profiles were studied for each material, with temperatures ranging from 700°C to 950°C and dwell times between 1 and 6 hours. LNO and NNO were succesfully fabricated onto LAO, STO and $(LaAlO3)_{0.3}(Sr_2TaAlO_6)_{0.7}$ (LSAT) single crystal substrates.

Film characterization during growth process

The best growing conditions, which ensure a well textured c-axis film growth, were found through a careful study where the annealing temperatures, dwell times and heating ramps were tunned. After each thermal process, we evaluated the film texture by performing θ-2θ XRD scans in a Bragg-Brentano configuration. The obtianed XRD spectra of the LNO and NNO films for different annealing temperatures is shown in Fig. 4.2 (a) and (b), respectively.

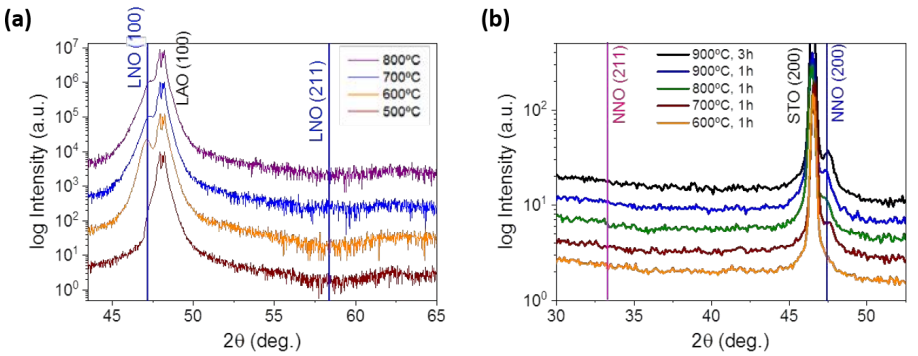

Figure 4.2: (a) θ-2θ XRD spectra of 25 nm-thick (a) LNO and (b) NNO films grown onto LAO and STO, respectively.

The $(100)_{LAO}$ and $(100)_{LNO}$ are the only Bragg reflections that are identified in the spectra that is shown Fig. 4.2 (a), which was obtained from

the LAO/LNO heterostrucutres. This confirms the growth of c-axis textured LNO films. Besides, the maximum $(100)_{LNO}$ peak amplitude was achieved when an annealing temperature of 600°C was used (orange line). The heating process of the NNO films was optimized by growing this compound onto a STO single crystal substrate, as the $(200)_{NNO}$ reflection overlaps with both the $(200)_{LSAT}$ and $(200)_{LAO}$ reflections, thus hindering the monitoring of the film epitaxy. The obtained spectra are shown in Fig. 4.2 (b), where only the $(200)_{STO}$ and $(200)_{NNO}$ reflections are identified, hence confirming the c-axis texture of the NNO film as well. In this case, it was necessary to go up to 900° for longer dwell times to obtain the maximum $(200)_{NNO}$ amplitude,

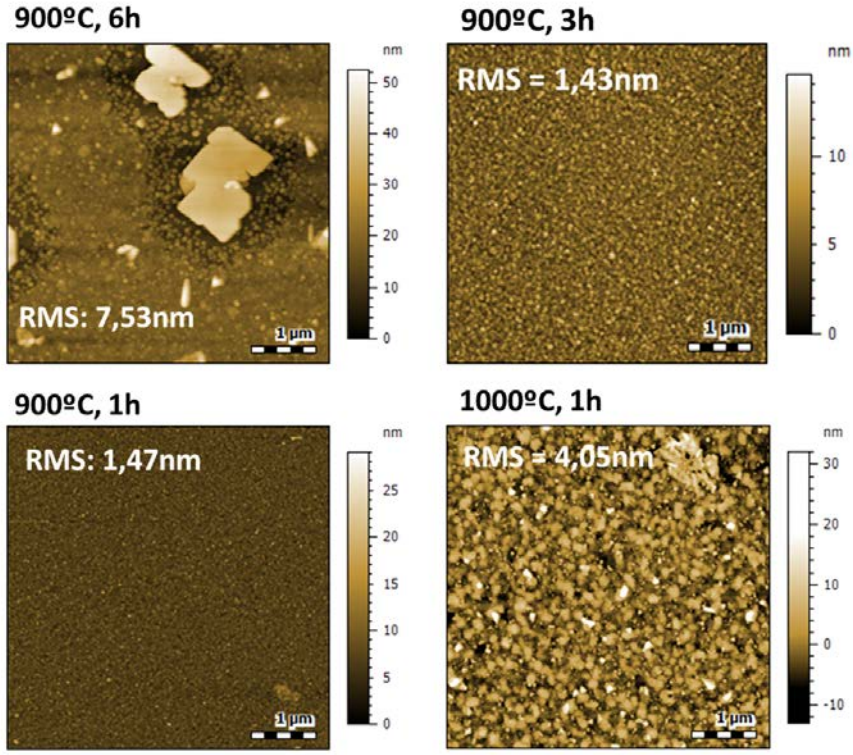

Figure 4.3: Top-view phase-contrast images of NNO films grown by different thermal treatments. The RMS (root-mean square) indicates the films' roughness.

as the NNO crystal is more unstable than the LNO due to its smaller RE radius

The roughness and surface morphology of the films were also evaluated by acquiring top-view phase-contrast images with an Atomic Force Microscope. Fig. 5.5 shows the film surface of four 12.5 nm-thick NNO films grown by different thermal processes. The films that present lower roughness values and smaller amount of surface aggregates are the ones annealed at 900°C during 1 to 3 hours.

The films' thickness was determined by XRD reflectometry experiments and afterwards confirmed from the STEM images. Fig. 4.4 (a) displays one

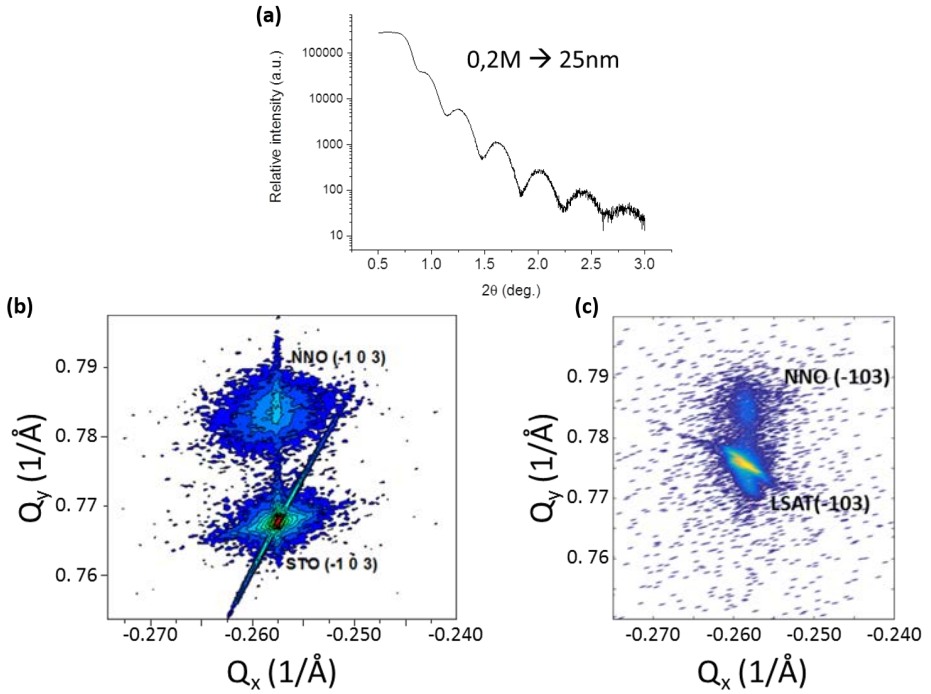

Figure 4.4: (a) XRD reflectometry measurement from a 25 nm NNO film. Reciprocal space maps of the (103) reflection of two 25 nm-thick NNO films grown onto (b) STO and (c) LSAT single crystal substrates.

illustrative example of the obtained reflectometry reflexions. A film thickness of 25 nm is estimated from the characteristic spacing between the reflected maxima, at the same time that a low film roughness is ensured.

Reciprocal space maps (*Q-plots*) were also analyzed in order to see the in-plane lattice parameter of the films. Fig. 4.4 (b) and (c) show the obtained *Q-plots* from tensile-strained NNO films grown onto either STO or LSAT single crystal substrates, respectively. Both films have the same Q_x value than their underlying crystal substrate, meaning that both films are biaxially strained.

4.4 Crystal structure

The NNO and LNO compunds present an orthorhombic and a rhombohedral unit cell structure, respectively. However, their pseudocubic unit cell structure resembles the perovskite structure, with the RE cations located at the cube corner positions and a NiO_6 octhaedral unit at the central position. Besides, their pseudocubic lattice parameters are similar to those from conventional ceramic substrates, such as LAO and LSAT, and therefore, it is possible to grow epitaxial RNO/LAO or RNO/LSAT heterostructures. The lattice parameters and strain values of the fabricated epitaxial heterostructures are summarized in Table 4.1.

RNO	$\mathbf{a}_{pc}^{film}$ (Å)	**Substrate**	$\mathbf{a}_{pc}^{subs}$ (Å)	**Strain** (%)	$\mathbf{T}_{MIT}$ (K)	**Thickness** (nm)
$\mathbf{NNO}_{ort}$	3.811	LAO_{rhom}	3.791	-0.5	198	20
$\mathbf{NNO}_{ort}$	3.811	LAO_{rhom}	3.791	-0.5	112	6
$\mathbf{NNO}_{ort}$	3.811	$LSAT_{cub}$	3.868	+1.5	Insulating	6
$\mathbf{LNO}_{rhom}$	3.859	LAO_{rhom}	3.791	-1.8	Metallic	6
$\mathbf{LNO}_{rhom}$	3.859	$LSAT_{cub}$	3.868	+2.3	Metallic	6

Table 4.1: Structural properties of the films. NNO and LNO cell parameters were extracted from Ref. [99] and the ones from LAO and LSAT were directly given by the substrate supplier. The nominal strain value (ε) is calculated by the common equation: $\varepsilon = \frac{a_{subs} - a_{film}}{a_{subs}}$, where $\varepsilon > 0$ means tensile strain

Fig. 4.5 (a) and (b) illustrate the pseudocubic cell structure of both NNO

and LNO phases, respectively. The oxygen octhaedra of both NNO and LNO compounds differ from the ideal perovskite structure. In the case of the LNO compound, the octahedra are tilted along the $a^-a^-a^-$ pseudocubic axes (following Glazerś notation) leading to a Ni-O-Ni bond angle of 165.2° [112]. Whereas, they are tilted along the $a^-a^-b^+$ axes in the NNO compound. This is not the only noticeable structural difference between NNO and LNO compounds, as Nd cations are shifted up and down drawing a zig-zag-like pattern (green arrows in Fig. 4.5 (b)) through the $[001]_{PC}$ direction (subscript PC for pseudocubic notation) in the NNO compound [113]. In the studied NNO films, in the absence of strain, the Ni-O_{basal}-Ni angles parallel to the substrate surface correspond to the 156.1° and 157.6° ones, whereas the perpendicular Ni-O_{apical}-Ni one is 157.6°.

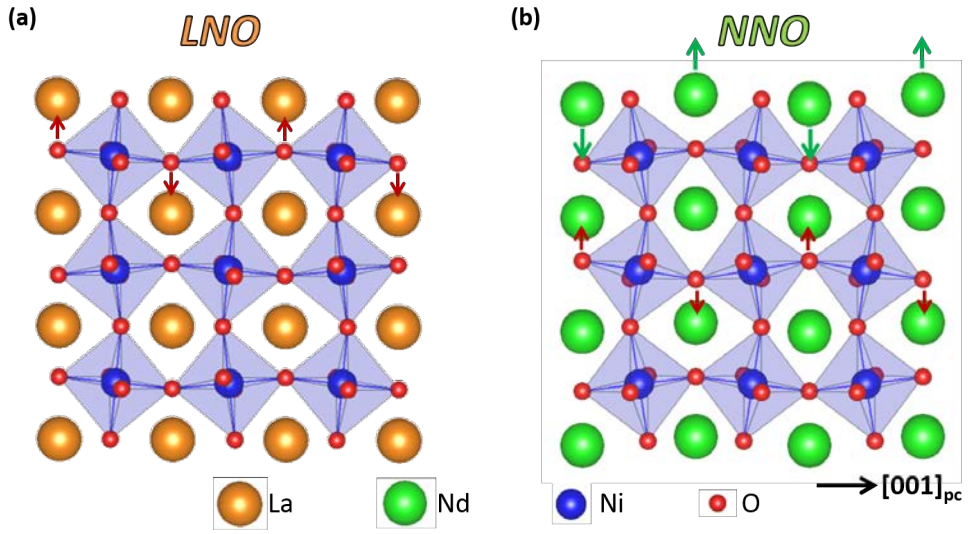

Figure 4.5: Pseudocubic structure of the (a) NNO and (b) LNO bulk phases. La, Nd, Ni, and O atoms are plotted in orange, green, blue, and red, respectively.

4.5 STEM-EELS characterization

In this section we describe the microstructure and the main defects appearing in each particular film. Fig. 4.6 shows low magnification Z-contrast

images of the films. In all cases it can be observed the presence of a continuous RNO film with a very flat surface. The films' thickness is also confirmed from these images, with values ranging between 4-6 and 24-26 nm (lower image), thus coinciding with the expected nominal values. Except for the LNO/LAO heterostructure, some dark aggregates are identified at the films' surface (yellow arrows), which evidence that a secondary phase is also formed during the growing process.

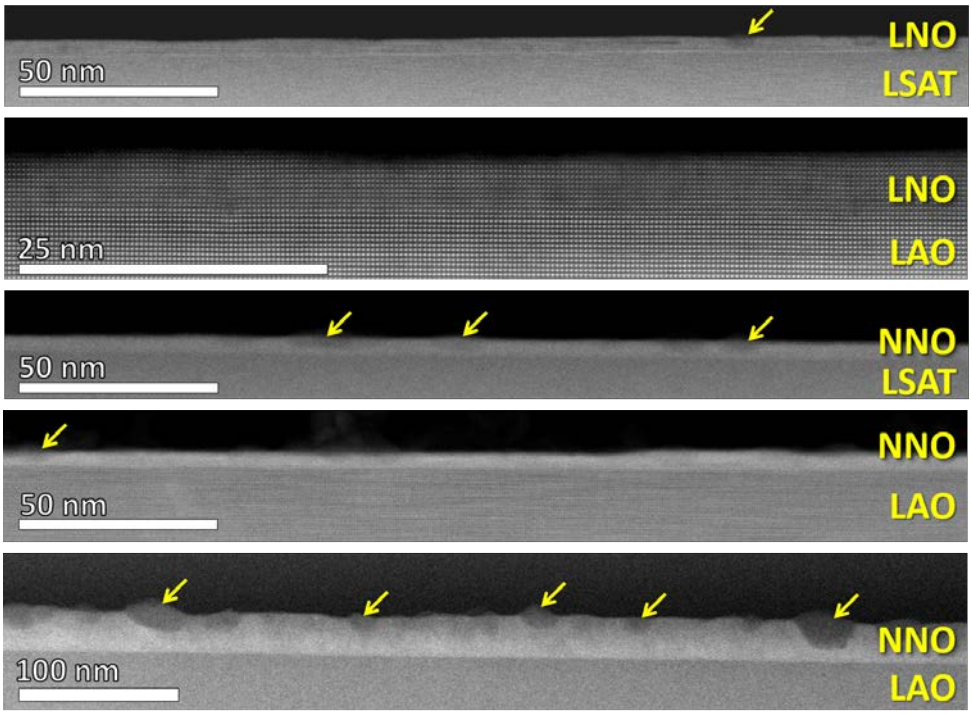

Figure 4.6: Low magnification Z-contrast cross-sectional images of the studied heterostructures. From the top to the bottom it is displayed the LNO/LSAT (6 nm), LNO/LAO (6 nm), NNO/LSAT (6 nm), NNO/LAO (6 nm) and NNO/LAO (25 nm). Yellow arrows point to the location where additional dark phases are identified.

The texture of the 6 nm-thick films is further evaluated by acquiring Z-contrast images with atomic resolution, see Fig. 4.7. These images further

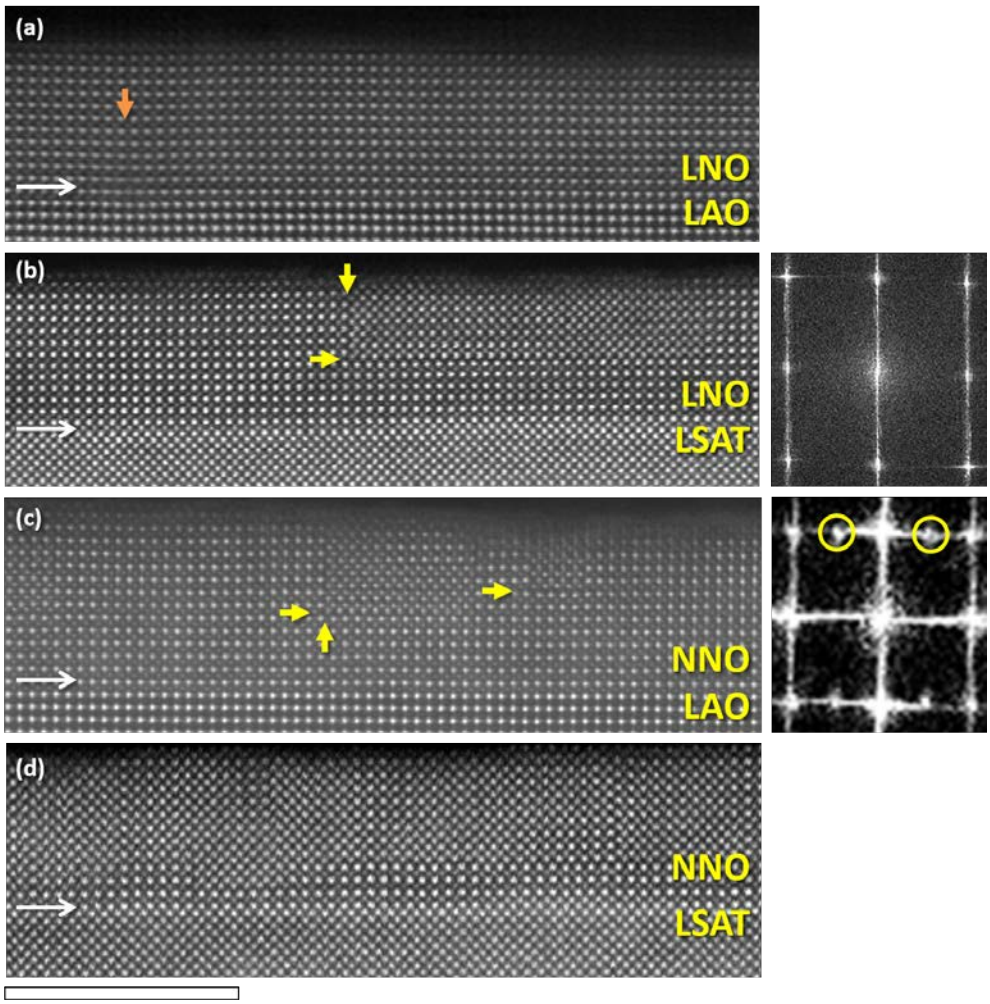

Figure 4.7: Z-contrast images of LNO and NNO thin films grown onto LAO (a), (c) and LSAT (b)-(d) substrates. Misfit dislocations and RPFs are pointed out with orange and yellow arrows, respectively. Inset shows the spots appearing at the Fourier transform (FFT) pattern associated to the Nd rippling (marked with yellow circles). Scale bar: 5 nm.

confirm the epitaxial growth of the 6 nm-thick RNO films, always exhibiting a cube-on-cube epitaxial relationship with the substrate crystals. Still, in some

areas, it is possible to identify the same Nd rippling present in NNO bulk crystals [113], see Fig. 4.5. This Nd rippling feature can be also detected by the appearance of additional spots in the corresponding fast-Fourier transform (FFT) pattern (yellow circles), as shown in the inset of Fig. 4.7 (c). For the particular thickness of 6 nm, we observe that the Nd rippling always runs parallel either to the [100]pc or [010]pc substrate directions, thus defining different grain domains. Besides, this Nd rippling permits to identify the $[100]_{PC}$ as the preferential NNO growing direction (normal to the substrate surface). In contrast, these spots are not observed in the FFT pattern associated to the images of the LNO compounds, see inset of Fig. 4.7 (b), as no La rippling is present in this compound. The substrate/RNO interfaces (marked with white arrows) are observed to be sharp and coherent. Two different kind of defects are identified within the films, which seem to depend on the used RE specie and substrate.

In the case of LNO grown onto a LAO substrate, misfit dislocations are generated at the substrate-film interface (orange arrow in Fig. 4.7 (a)). If the film is fully relaxed by the misfit dislocations, it is possible to estimate the separation (S) between them by this simple expression: $S = |b| / \varepsilon$, where ε refers to the nominal strain value and b is the Burgers vector associated to the misfit dislocation [114, 115]. Considering that $\vec{b} = (100)$ and $\varepsilon = -1.8\%$, misfit dislocations are expected to be 21 nm apart if the sample is fully relaxed. However, they are observed to be separated 50nm in the Z-contrast image of Fig. 4.8, where two neighboring misfit dislocations are viewed (yellow arrows).

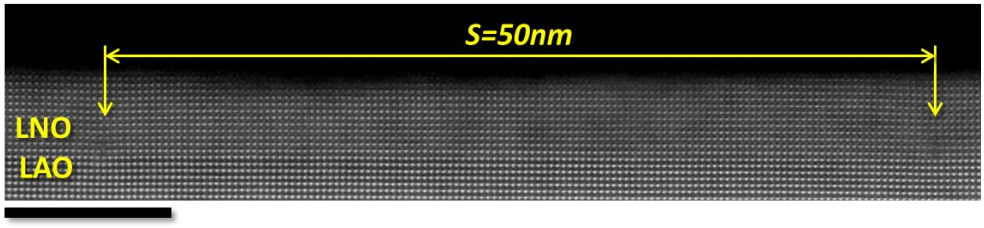

Figure 4.8: Z-contrast image of the 6 nm-thick LNO film where two misfit dislocations are identified (yellow arrows). Scale bar: 10 nm.

This larger separation indicates that the LNO film is still partially strained even though the presence of misfit dislocations. The fact that, from the

whole set of studied samples, we have only observed misfit dislocations in the LNO/LAO heterostructure indicates that the substrate structure has a major influence on the type of defect that is generated within the RNO films, which are formed to accommodate the epitaxial strain. Accordingly, the fact that both the substrate and the film share the same rhombohedral symmetries in this case might favor the formation of misfit dislocations instead of other lattice defects, which are not observed in this film.

In the other heterostructures, the RNO crystals prefer to create another kind of defect: the Ruddlesden-Popper fault (RPF) (yellow arrows in Fig. 4.7). As sketched in Fig. 4.9 (a), the RPF is characterized by suppressing a Ni-O plane at the same time that the unit cell structure is shifted half-unit-cell along the $[111]_{PC}$ direction [116, 117]. In the RPF defect, the Nd and O atoms are arranged like half-unit-cell of the rock-salt structure while the perovskite structure is preserved at either side of the fault, but shifted. In Fig. 4.7, it is seen that the RPFs run along either the basal or out-of-plane crystallographic axes. However, we have further acquired a planar view Z-contrast image in order to confirm that the RPFs are only oriented along the crystallographic

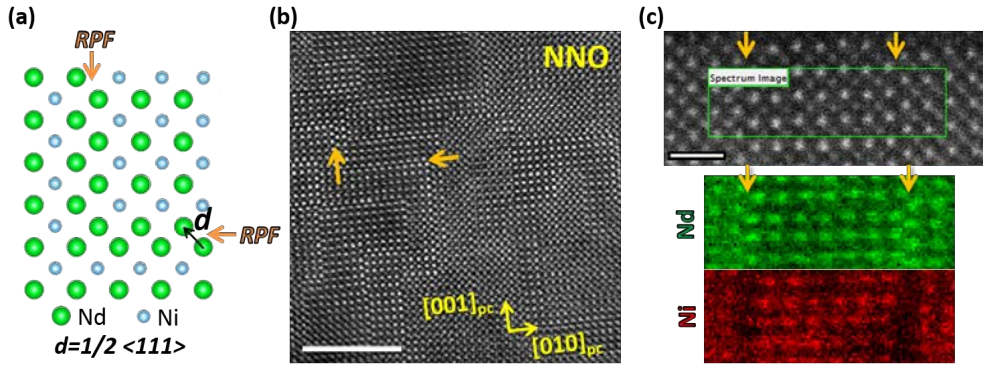

Figure 4.9: (a) Illustration of the NNO crystal with a horizontal and a vertical RPFs (orange arrows). The Nd and Ni cations are represented as green and blue circles. (b) Planar view Z-contrast image of the NNO film. The orange arrows point to some RPFs. (c) From the top to the bottom the image shows a Z-contrast image with the green area from where the EELS-SI was acquired and the Nd (green) and Ni (red) EELS compositional maps.

axes, see Fig. 4.9 (b). Notice that in some areas of the Z-contrast images that are shown in Fig. 4.7 and Fig. 4.9 (b), the Nd and Ni atomic columns have the same contrast because two different nanometer-sized regions, shifted by the rock-salt fault, are superimposed along the viewing axis. When this happens, the RE and the Ni atomic columns lie one upon another and the difference in contrast is canceled [65, 116].

In Fig. 4.9 (c), we show a zoom-in into an area of Fig. 4.9 (b), where two parallel RPFs are viewed (orange arrows). We have investigated their chemical composition by acquiring an EELS-SI from the area marked with a green square. The green and red color maps correspond to the Nd and Ni EELS compositional maps, which have been obtained by integrating in all pixels the area beneath the Nd M_{45} and Ni L_{23} EELS peaks, respectively. These maps confirm that the Ni signal decreases at the rock-salt fault, due to the suppression of the Ni-O plane, and that both of its sides are composed by Nd-O planes.

As the precursor solution contains the exact $RENiO_3$ stoichiometry, the presence of the RPFs poses a stoichiometric issue. It is worth remembering that some secondary phases were previously identified in some of the Z-contrast images of Fig. 4.6. The chemical composition of one of these aggregates is investigated by performing EEL spectroscopy. Fig. 4.10 (a) and (b) show low resolution cross sectional and planar view images of a 25 nm-thick NNO/LAO heterostructure, respectively, containing some of these secondary phases. These NiO NPs are always observed to be homogeneously dispersed at the surface of the films with diameters ranging approximately between 5-50 nm.

One of these secondary phases is viewed in a higher magnification Z-contrast image in Fig. 4.10 (c). We have acquired an EEL spectrum from one of these phases, which is shown in Fig. 4.10 (c) (red line). The obtained spectrum is observed to be analogous than the NiO reference spectrum (black line), which is also displayed in the plot. Besides, we have further confirmed that all the other secondary phases are also NiO nanoparticles. Interestingly, they are not identified in the LNO/LAO heterostructure, as the LNO crystal prefers the generation of misfit dislocations rather than RPF defects.

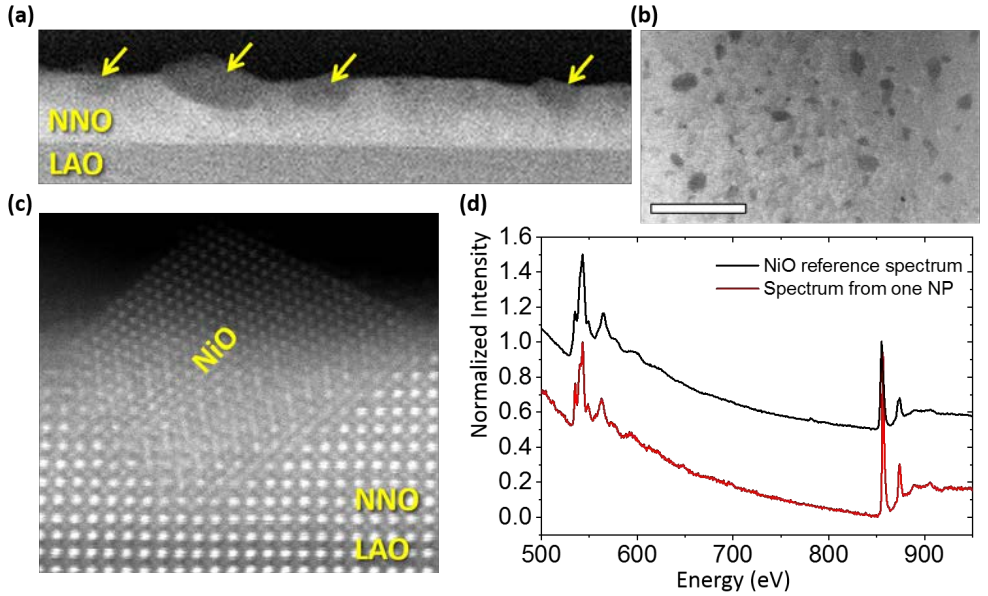

Figure 4.10: (a) Cross sectional and (b) planar view Z-contrast images of a 25 nm-thick LAO/NNO heterostructure containing some NiO aggregates (yellow arrows) at the film surface. Scale bar: 200 nm. (c) Z-contrast image of a 6 nm-thick LAO/NNO heterostructure with a NiO NP from where we have acquired the EEL spectrum shown in (d) (red line). The reference NiO EEL spectrum (black line) is also displayed for comparison

The atomic structure of a 25 nm-thick NNO/LAO heterstructure is evaluated by acquiring the Z-contrast image that is shown in Fig. 4.11. The LAO/NNO interface is atomically sharp and coherent. The first 6-10 nanometers (below the yellow line) are observed to be clean of defects and, above this first layer, a dense network of RPFs is present. As previously commented, we can identify the typical Nd rippling also observed in bulk crystals from the FFT pattern associated to this Z-contrast image. From the patterns acquired in different film regions, see Fig. 4.11 (b) and (c), we can still identify the spots associated to the Nd rippling (yellow circles) but, differently than in the 6 nm-thick films, the Nd zig-zag is also observed to occur along the out-of-plane direction in this 25 nm-thick film (Fig. 4.11 (c)).

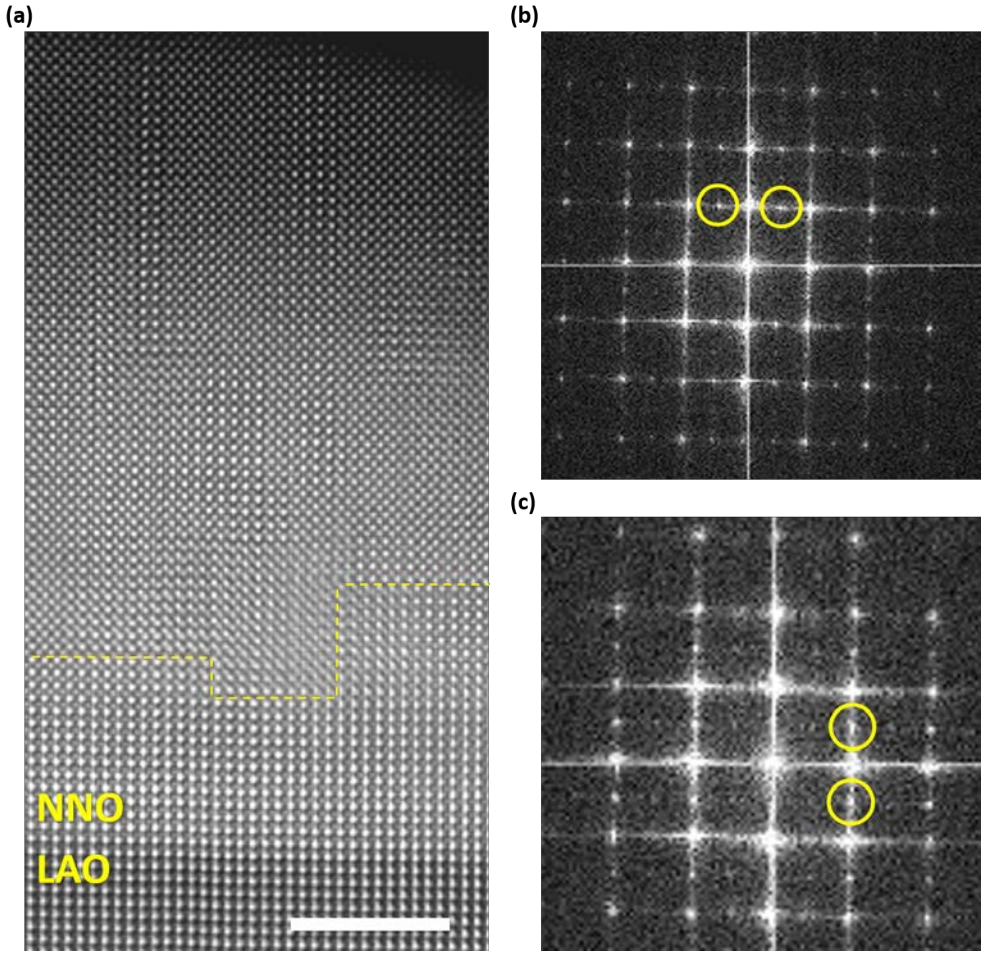

Figure 4.11: (a) Z-contrast image of a 25 nm-thick NNO film grown onto LAO. The dashed yellow line separates the defect-free slab and the upper film region with a lot of RPF defects. Scale bar: 5nm. (b) and (c) FFT patterns obtained from different film regions. The yellow circles indicate the reflections ascribed to the Nd rippling.

We have additionally evaluated the density of RPFs (R) for each 6 nm-thick RNO film. This calculation was performed by summing the perimeter length of all the viewed RPFs in several Z-contrast images and dividing the resulting number by the total film area that was used, as done in Ref. [118]. The obtained

R values for the NNO films are 0.22, when grown onto LAO ($\varepsilon \approx -0.5$), and 0.70 nm^{-1}, when grown onto LSAT ($\varepsilon \approx 1.5$); whereas the obtained R values for the LNO films are 0, when grown onto LAO ($\varepsilon \approx -1.8$) due to the presence of misfit dislocations, and 0.044 nm^{-1} when grown onto LSAT ($\varepsilon \approx 2.3$). These R values evidence that the density of RPFs tends to increase with the substrate mismatch value in both RNO compounds. The residual resistivity of each RNO film is also observed to increase with R.

4.5.1 GPA analysis

The fact that the concentration of RPFs increases with the substrate mismatch suggests that the occurrence of RPFs is a strain relief mechanism that helps to accommodate the epitaxial strain of the RNO films. We have carried out a strain analysis study in all the LNO and NNO layers in order to further confirm this statement. We have used the GPA software, which allows for measuring strain, or deformation, with respect to some reference area, in our case the substrates. Circular masks with radii producing a lateral resolution of approximately 1 nm in the GPA images were defined around the (200) and the (002) reflections in order to minimize possible artifacts coming from the RPFs and LSAT substrate. The resulting in-plane e_{xx} and out-of-plane e_{yy} strain maps are shown in Fig. 4.12. Regarding the LNO films (Fig. 4.12 (a) and Fig. 4.12 (d)), the e_{xx} distortion maps show no color depth-wise variations in defect-free areas, meaning that the substrate in-plane parameter is completely transferred to the film. On the other hand, the observed color change in the e_{yy} distortion map is associated to an out-of-plane parameter expansion (compression) in the compressive-strained (tensile-strained) LNO layer when grown onto LAO (LSAT). The resulting strain is homogeneous within the layer with values around 2%(-1.5%) in samples grown onto LAO (LSAT). These results confirm that both films are still partially strained with values similar than those reported in previous studies [117].

In the case of NNO films, different scenarios are observed; see Figs. 4.12 (b-c, e). First, the e_{xx} map corresponding to the NNO film grown onto LAO (low compressive strain) shows a coherent strained film with a homogeneous out-of-plane expansion of 1.5% respect the bulk value. Second, the NNO film shows two differentiated regions when grown onto a LSAT substrate: a three-unit

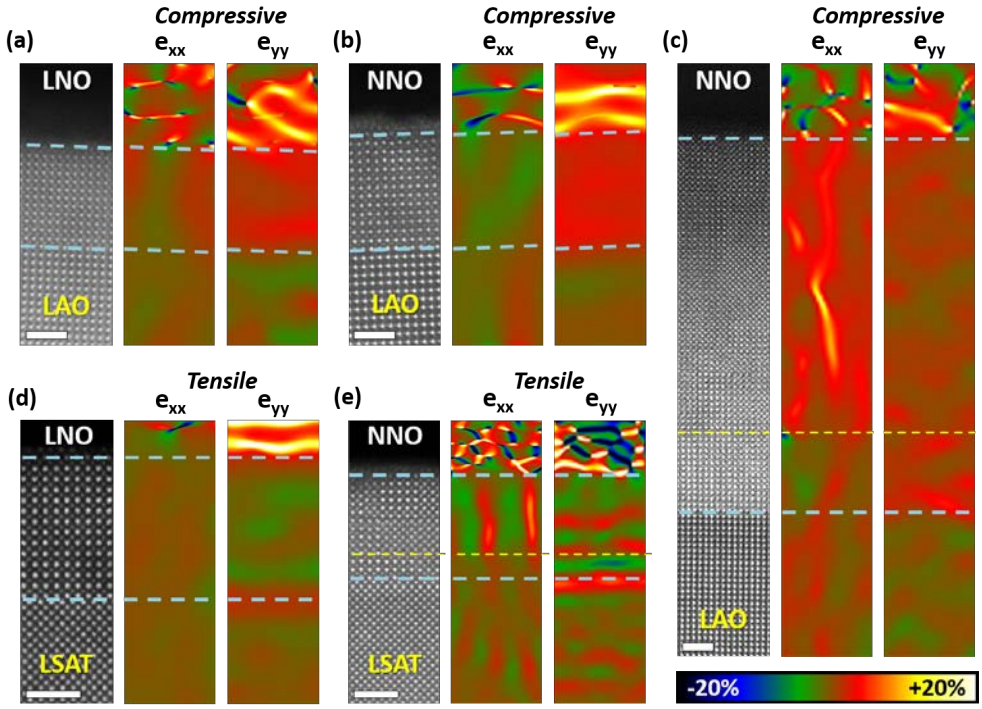

Figure 4.12: Z-contrast images and e_{xx} and e_{yy} deformation maps obtained from the (a-b) 6 nm-thick LNO/NNO films grown onto LAO and LSAT (d-e) substrates, and from a (c) 25 nm-thick NNO/LAO film. Maps are displayed with a temperature scale whose contrast limits are ±20%. The films' edges are indicated with blue dashed lines. Areas below the yellow dashed lines are clean of defects. Scale bars: 2nm.

cell-thick defect-free slab close to the interface, and a dense network of rock-salt faults above it. The yellow dashed line in Fig. 4.12 (e) marks the interface between these two different regions of the NNO film. The e_{xx} map reveals a fully strained and coherent defect-free slab region, i.e., an expansion of the in-plane NNO cell parameter. Besides, as expected for a Poisson-like deformation, the e_{yy} map shows an out-of-plane compressed layer. However, in the upper layer, strong contrast variations are observed in the e_{xx} and e_{yy} maps, stemming from a large concentration of rock-salt faults. Interestingly, the 25-nm-thick NNO film grown onto LAO also shows a 6 nm-thick defect-free layer that is compressed (expanded) along the in-plane (out-of-plane) direction, growing up

to the first 6 nm of the film; see Fig. 4.12 (c). Yet, in the upper region of the film, with larger amount of RPF defects, the in-plane parameter is expanded, suggesting that abundant presence of RPF helps to the accommodation of the epitaxial strain in this region.

4.5.2 Defect-driven distortions

We have further studied the subtle distortions appearing around the RPF defect. Fig. 4.13 (a) shows a Z-contrast image of the LNO/LSAT heterostructure with an horizontal RPF crossing the middle of the LNO film. The central position of all the viewed atomic columns are identified by using the center-of-mass refinement process. From the set of coordinates associated to the La sub-lattice, we obtain a detailed real-space map of the in-plane (green) and out-of-plane (blue) parameters, both shown in Fig. 4.13 (b). No substantial variations are identified within the in-plane color-map, meaning that the substrate imposes its in-plane cell parameter to the whole LNO film. On the contrary, in the out-of-plane parameter map (blue), some variations are identified at the rock-salt fault and at the cells that are adjoining the fault, which are observed to be darker than the other ones. This evidences that the Nd-Nd spacing is compressed at these positions. In order to study this distortion in more detail, we have averaged the cell parameter values at each film monolayer, which are displayed in the upper depth-profiles of Fig. 4.13 (c).

As expected, the substrate in-plane parameter is observed to be transferred from the substrate to the whole film. Besides, the elimination of the NiO plane at the rock-salt fault structure (black arrow) reduces the Nd-Nd spacing along the out-of-plane direction a value of 2.891Å (a_{NNO} = 3.812Å). As observed in the blue map, the cells located at either side of the rock-salt fault are also compressed an approximate relative value of -5% or -6% along this direction, taking as a reference the film or substrate, respectively, which is tantamount a reduction of the unit cell volume.

From the Ni set of coordinates, we have measured the distance δ between the Ni and the unit cell center-of-mass positions, as illustrated in the inset of Fig. 4.13 (c). We observe that the Ni atomic columns shift towards the fault at either side of the fault, thus generating a polar-like distortion. It is worth

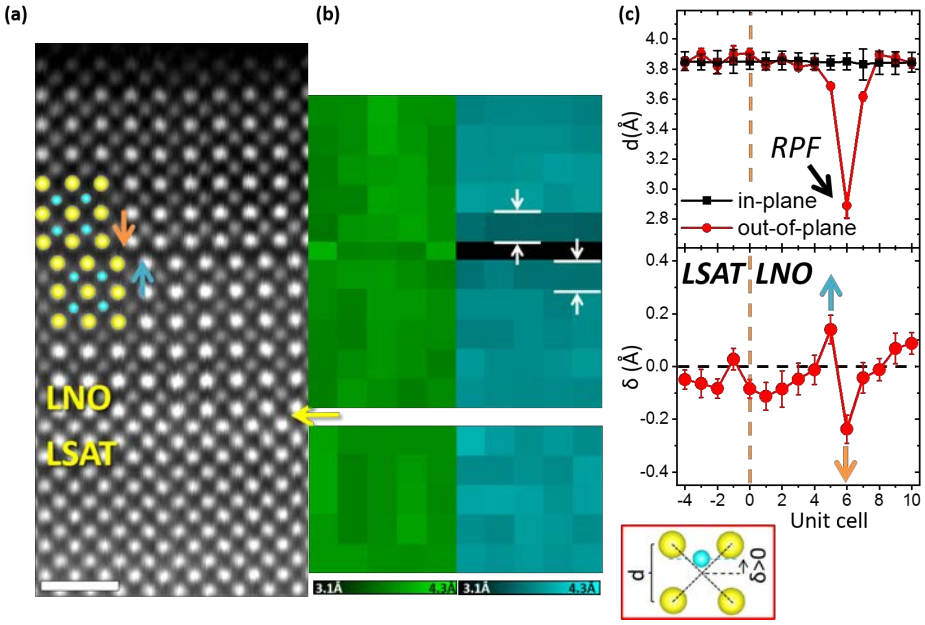

Figure 4.13: (a) Z-contrast image of a LNO/LSAT heterostructure with a horizontal RPF crossing the middle of the film. The yellow arrow marks the LNO-LSAT interface. The La and Ni cations are sketched with yellow and blue circles, respectively. Scale bar 1 nm. (b) In-plane (green) and out-of-plane cell parameter maps obtained from (a). Each square represents one unit cell whose intensity scales with the measured parameter value. (c) Top: averaged values of the in-plane (black) and out-of-plane (red) spacings. Bottom: Depth-profile of the δ spacing. The dashed line marks the interface between the LNO film and the LSAT substrate. Inset: schematics of the LNO structure showing the measured spacings (d and δ).

noting that both effects are confined only at the very first unit cells surrounding the RPF and that they are observed in all the studied heterostructures. These out-of-plane distortions are similar to those observed in the LNO/LAO heterostructures direction [119, 120], but different in orientation to those recently reported oxide systems such as the $Sr_{n+1}TinO_{3n+1}$ Ruddlesden-Popper phase [121], which show a polar distortion parallel to the rock-salt fault plane.

These distortions are always generated concomitantly to the formation of

RPFs, regardless of the used RNO compound and RPF orientation. An example of that is shown in Fig. 4.14 where it is displayed a Z-contrast image of a NNO/LAO heterostructure containing a vertical and a horizontal RPFs, and its corresponding in-plane (green) and out-of-plane (blue) cell parameter maps. Both maps reveal a cell compression, along the normal direction of the RPF, in the cells located at either side of both faults.

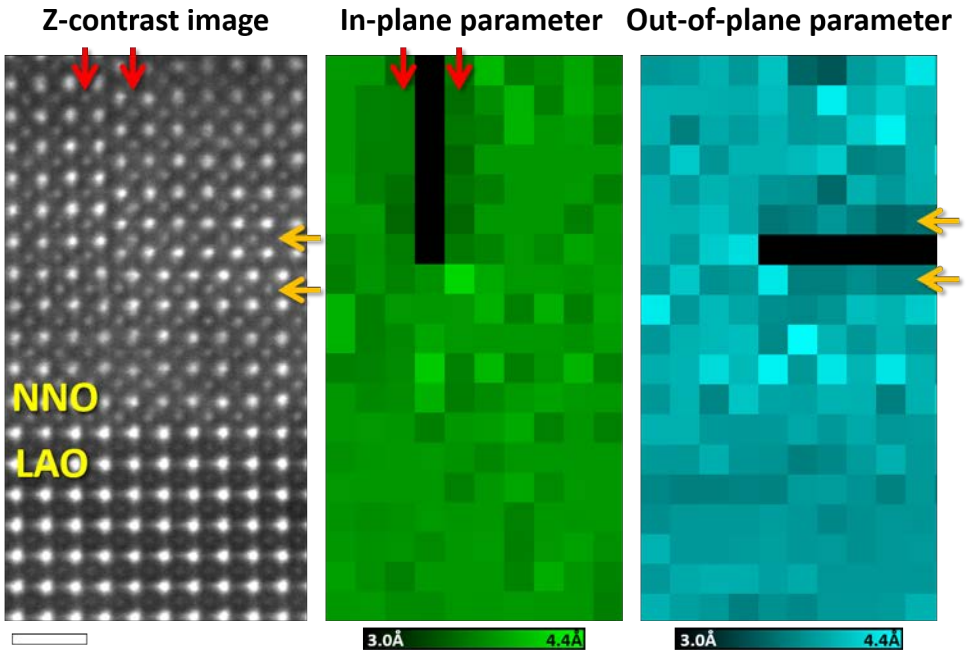

Figure 4.14: From left to right: Z-contrast image of a LAO/NNO heterostructure, containing a vertical (red arrows) and a horizontal RPF (orange arrows), and the measured in-plane (green) and out-of-plane (blue) cell parameter maps.

4.6 Transport properties

In order to see the influence of the RPFs in the RNO electrical properties, we have measured the evolution of the films' resistivity with the temperature, which are displayed in Fig. 4.15, . These measurements were performed using Van der Pauw configuration in a PPMS Quantum design system with variable

temperature, ranging from 400K down to 5K. From the obtained curves, it is clearly observed that both the film resistivity and the T_{MIT} are highly influenced by the substrate, film thickness and RE cation specie. In particular, the sharp MIT is only observed in NNO films grown onto the LAO substrate, which is shifted from 201K (in bulk) to lower temperatures when the film is compressed by epitaxial strain, as equally reported by *Catalano et al.* from magnetron sputtered RNO thin films [101, 103]. This is not occurring when NNO is grown onto LSAT substrate (tensile-strain) which always behaves as an insulating material for the measured range of temperatures. In contrast, LNO films remain always metallic (as in the case of bulk) regardless of the used substrate, even though the resistivity is different in each case.

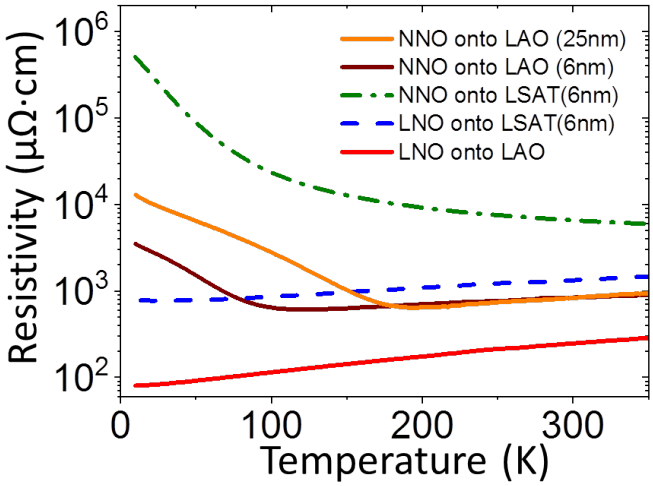

Figure 4.15: Evolution of the films' resistivity with temperature. Solid lines correspond to the NNO films whereas dashed lines to the LNO ones.

The films' microstructure described so far allows establishing some correlations with these resistivity measurements. As shown in previous studies, the electrical transport of RNO films is influenced by the mismatch [100, 101], orientation [103, 122], and symmetry [123] of the chosen substrate; and by the film thickness [100] and termination [119, 124]. All of these parameters play a

role on the stabilization of the Ni-O-Ni bond angles and lengths and therefore on the intrinsic RNO electronic configuration [11, 99, 104]. From the transport measurements of our films, shown in Fig. 4.15 (b), it is observed that compressive strain shifts the MIT to lower temperature values in NNO films as a direct consequence of the narrowing of the Ni-O bonds [11, 100, 101, 109]. Besides, tensile strain increases the film resistivity more than one order of magnitude, in both LNO and NNO films, compared to the compressed films. On the one hand, this increase of the resistivity might be also ascribed to an enlargement of the Ni-O bond lengths. However, the lower resistivity measured in the Pulsed Laser Deposition-derived LNO/LSAT [125] suggests that the RPFs also influence the electrical transport, as the RPFs might act as blocking barriers agents to the current flow due to the Ni-O plane suppression. This is more evident in the case of the NNO/LSAT heterostructure, where the high concentration of RPFs, with only two or three defect-free monolayers, not only increases the film resistivity more than one order of magnitude, but it also enlarges the insulating behavior out of the measured range of temperatures (5-400K). Besides, when comparing the resistivity vs temperature curves of RNO films grown by chemical and physical methods, one realize that CSD-derived RNO films have a less abrupt MIT [101, 103, 116, 126], which we ascribe to their larger concentration of defects.

4.7 Summary and conclusions

In short, we have investigated the defect landscape that is present in epitaxial NNO and LNO thin films when grown onto LAO and LSAT, which induces an epitaxial compressive- and tensile-strain, respectively.

We have observed that misfit dislocations are generated when both film and substrate share the same structure, in the LAO/LNO heterostructure, whereas Ruddlesden-Popper faults are formed in the other scenarios. We have carried out a strain analysis to confirm that all the films were still epitaxially strained when they had a thickness of 6 nm. Whereas, the 25 nm-thick film exhibited an in-plane expansion at the upper film region where high amount of RPFs were present, thus becoming a strain relaxation mechanism. In addition, we have observed that the density of RPFs also increases with the substrate

mismatch value.

We have also characterized the additional structural distortions occurring around the RPFs. In particular, we have observed a huge structural compression at the rock-salt fault defect along its normal direction due to the suppression of the Ni-O plane. Those cells located at either sides of the fault were also observed to be compressed along the fault perpendicular direction as well. Besides, a polar-like distortion has been identified at those cells adjoining the fault. In particular, their Ni atoms were shifted far from their unit cell central position towards the rock-salt fault.

We have also measured the electrical transport properties of the studied films. We have observed that both the strain and the presence of the RPFs affect their electrical conductivity and the MIT. While the compressive strain shifts the MIT transition to lower temperatures, due to an increase of the Ni and O orbital overlapping, the presence of RPFs seem to be detrimental for the electrical transport, as the Ni-O-Ni bonds are locally truncated at the faults. We believe that the RPFs is the preferential defect in RNO compounds. However, the generation and density of RPF was observed to depend on the used substrate and its orientation, epitaxial strain, RE compound and growing conditions.

Chapter 5

Structural and physical properties of LSMO ultrathin films

5.1 Chapter preview

In this chapter, we study the physical and structural properties of $La_{0.67}Sr_{0.33}MnO_3$ (LSMO) thin films grown by CSD onto a $SrTiO_3$ (STO) single crystal substrate, with thicknesses ranging between 2-22 nm. A transition from a metallic to an insulating regime is observed when the film thickness is reduced down to two nanometers. However, all the studied samples present similar ferromagnetic behaviors, which contradicts the double-exchange transport mechanism expected in this compound. Besides, it has been previously reported that LSMO films transit from a ferromagnetic-metallic to a non-ferromagnetic-insulating phase when the film thickness is reduced below a critical value due to the appearance of a dead layer [127–130]. Some authors attributed this phenomenology to the segregation of non-ferromagnetic and insulating phases close to the substrate surface [129**?** –132], other ones to orbital reconstruction effects at the STO/LSMO interfaces [128, 133]. Nonetheless, there is still controversy behind this phenomenology. Here, we use the combination of STEM-EELS to investigate the atomic and chemical structure of our CSD-derived samples in order to get new insights into the exhibited thickness-dependent ferromagnetic-conducting to ferromagnetic-insulating transition.

5.2 Introduction

5.2.1 Phase diagram and physical properties

Manganese oxides, also referred to as manganites, is one of the most studied perovskite oxides [7, 10, 134]. The ferromagnetic behavior of $LaMnO_3$-$CaMnO_3$, $LaMnO_3$-$SrMnO_3$ and $LaMnO_3$-$BaMnO_3$ mixed crystals was discovered in 1950 by the hand of Jonker and Van Santer [135]. The interest for these compounds re-emerged during the nineties after the discovery of their *"Colossal Magnetoressistance"* (CMR) effect close to the Curie temperature (T_C) [136, 137].

Among other manganite compounds, $La_{1-x}Sr_xMnO_3$ stands out as it exhibits the largest bandwidths and T_C values [7, 10]. Its phase diagram, shown in Fig. 5.1(a), is composed by several structural, electric and magnetic phases arising at different temperature and Sr concentration conditions.

At low temperatures and low Sr doping ($x \approx 0$), $La_xSr_{1-x}MnO_3$ is anti-ferromagnetic, insulating and orthorhombic. As the Sr doping increases, the system transits towards a metallic-ferromagnetic regime while the crystal structure becomes rhombohedral (R). If we keep increasing the Sr content, the system becomes orthorhombic, insulating and anti-ferromagnetic (firstly A-type and then C-type). The maximum T_C temperature (red line) is reached at $369K$ when the structure has a Sr content of 0.33.

Above the T_C (red line) and Néel temperatures (green lines), the $La_xSr_{1-x}MnO_3$ compound always behave as a paramagnet, although transitioning from an insulating-orthorhombic phase (low Sr content) to a metallic-rhombohedral, metallic-tetragonal, semiconducting-tetragonal and semiconducting-cubic regimes when progressively increasing the Sr concentration. This huge variety of structural, magnetic and electric phases is linked to the strong coupling between the lattice, orbit and spin degrees of freedom. In addition, the Sr concentration tailors the overall Mn valence state, thus governing the magnetic moment and the amount of available carriers (holes) within the Mn *3d*-energetic levels, which also governs the electrical conduction [7].

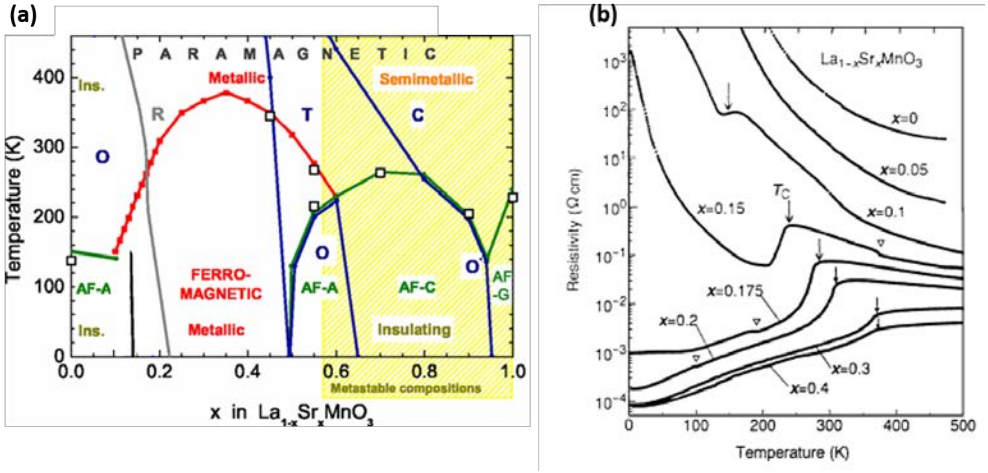

Figure 5.1: (a) Structural, magnetic and electric $La_{1-x}Sr_xMnO_3$ phase diagram as a function of the temperature (K) and the Sr content. AF-A, AF-C and AF-G refer to A-, C- and G-type anti-ferromagnetic configurations while C, T, R and O refer to cubic, tetragonal, rhombohedral and orthorhombic structures, respectively. The red and green line indicates the T_C and Néel temperature, respectively. (b) Resistivity vs temperature curves measured in $La_{1-x}Sr_xMnO_3$ single crystals with different Sr content (x). Arrows and open triangles indicate the Curie temperature and anomalies associated to structural distortions, respectively. These figures have been extracted and adapted from [10, 138]

In the $LaMnO_3$ (x=0) compound, Mn cations have an oxidation state value of +3, with one electron within the e_g level. The additional Sr^{+2} cations, which substitute the La^{+3} cations, take electrons from their neighboring Mn^{+3} cations, thus injecting additional holes within the Mn e_g level and therefore changing some Mn^{+3} to Mn^{+4}. This change on the electronic configuration of the $La_xSr_{1-x}MnO_3$ modifies its physical properties such as the T_C , magnetic moment, electrical behavior or resistivity. A clear example of that is shown in Fig. 5.1 (b), where the resistivity (ρ) of different $La_xSr_{1-x}MnO_3$ single crystals, having distinct Sr concentrations, are plotted as a function of the temperature. It is observed that the resistivity decreases when the Sr is increased at the same time that the system transits from an insulating to a metallic behavior at $x \approx 0.175$. Besides, the system exhibits a metal-to-insulator

transition when 0.175<x<2 at temperature values coinciding with the T_C.

The LSMO properties are also influenced by the presence of structural modifications occurring due to the presence strains. This is typically accomplished by growing the LSMO crystal as epitaxial thin films onto single crystal substrates, which impose the epitaxial strain. These structural distortions might modify the electronic configuration of LSMO and hence, its physical properties. As a consequence of that, it is crucial to understand both the structural and magnetic changes occurring at the LSMO/substrate interfaces for the development of devices based on the colossal magnetoresistance or exchange-bias effects [7, 139].

5.2.2 Crystal and electronic structure

The $La_{0.67}Sr_{0.33}MnO_3$ (LSMO) compound has a rhombohedral unit cell structure that is preserved in all the exhibited magnetic and electric phases. Its pseudocubic cell structure resembles the perovskite structure with the characteristic $a = 3.876$Å and $\alpha = 90.46$ lattice parameters [140]. The Mn cation is placed at the central position of the cubic structure and it is octahedrally coordinated with 6 oxygen atoms, forming a MnO_6 unit. One third of the La cations, which sit at the cube corner positions, are substituted by Sr^{+2}.

The LSMO electronic states are depicted in Fig. 5.2 (a). The internal crystal field resulting from the MnO_6 octahedral coordination splits the degenerated Mn *3d*-band into two new energy levels: the three-fold t_{2g} level (lying in lower energy) and the doubled e_g states [1]. Electrons successively occupy the available energetic levels located at lower energies while keeping the same spin orientation, which minimize the Coulomb repulsion energy as dictated by the Hund rules. This particular electronic configuration leads to two energetic bands whose energy depends on the spin orientation (up and down). This is the reason why LSMO is able to reach full spin polarization at low temperatures, becoming a half-metallic ferromagnet. The e_g level is only partially occupied in the case of Mn^{+3} cations. In the case of Mn^{+4} cations, the e_g level remains empty, with only three electrons populating the less energetic t_{2g} shell. The electronic configuration, spin and magnetic moments of Mn^{+3} and Mn^{+4} cations are $t_{2g}^{3\uparrow}\ e_g^{\uparrow}$, S=2 and $M = 4\mu_B$; and $t_{2g}^{3\uparrow}$, S=3/2

and $M = 3\mu_B$, respectively.

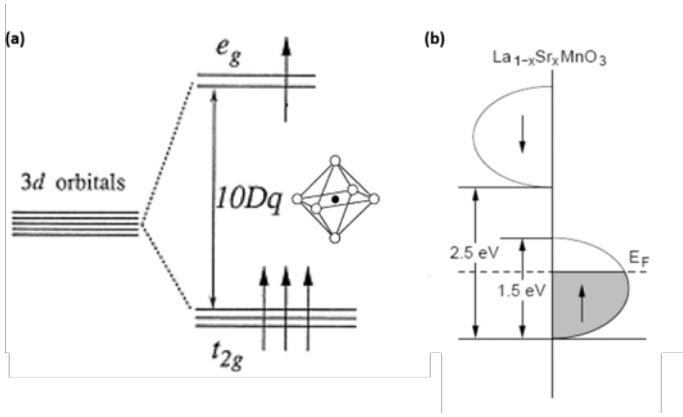

Figure 5.2: (a) Mn^{+3} 3d electronic shell. The 5-fold degenerated *3d*-energetic level splits into the lower 3-fold degenerated t_{3g} and higher 2-fold eg energy bands as a result of the internal field generated by the O octahedra. (b) Spin-dependent energetic bands of $La_{1-x}Sr_xMnO_3$ crystals. The given energetic values correspond to the particular case of $La_{0.67}Sr_{0.33}MnO_3$. These figures have been extracted from references [8, 134]

Besides, the electrical transport and magnetic behavior are strongly coupled in LSMO crystals due to the Double-exchange (DE) mechanism, which is described in the following section.

5.2.3 Transport and magnetic properties

In first approximation, the movement of electrons in $La_xSr_{1-x}MnO_3$ compounds (with intermediate Sr doping) is based on the DE mechanism proposed by Zener in 1951 [141]. As it is sketched in Fig. 5.3 (a), this transport mechanism consists on the simultaneous hopping of two electrons between neighboring Mn cations assisted by an intermediated oxygen anion. The first electron jumps from the left-sided Mn^{+3} e_g level to its neighboring O *2p*-orbital. At the same time, the electron that have the same spin orientation, located at the O *2p*-level, hopes from this intermediated *2p*-O orbital to the available e_g level, placed at its right-sided Mn^{+4}. After one DE interaction,

the oxidation state of the two neighboring Mn cations is exchanged without reducing the overall ferromagnetic moment, as sketched in Fig. 5.3 (b). Zener pointed out that this hopping mechanism was only allowed in ferromagnetic crystals, where all Mn cations share the same spin orientation. In addition, the DE interaction only occurs in $La_xSr_{1-x}MnO_3$ compounds that has a mixed Mn valence between +3 and +4, as some Mn e_g states have to remain available for allowing the electron movement.

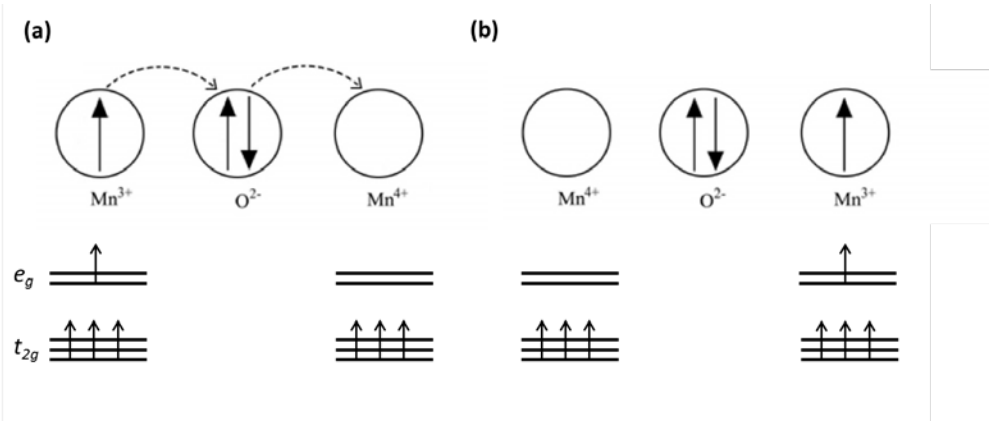

Figure 5.3: Schematic representation of the Double Exchange mechanism.(a) Initial and (b) final configuration before and after one DE process.

Few years later, P. W. Anderson and H. Hasegawa demonstrated that the hopping probability in a DE mechanism was described by the expression: $t_{ij} = t_0 \cos(\theta/2)$, where t_0 is the orbital overlapping and θ the relative orientation between the spins of the electrons [142]. Even though the maximum transition probability was still occurring when both Mn cations were aligned ferromagnetically, the DE mechanism was also allowed in other magnetic configurations.

As it is described in the formula, the hopping probability, and hence the LSMO resistivity, is also influenced by the t_0 parameter. This parameter correlates with the Mn-O bond angle, reaching the maximum value when Mn and O are confined at the same plane. However, the presence of octahedral

tilts reduces their shell overlapping, thus increasing the LSMO resistivity. In bulk LSMO crystals, the oxygen octahedra are tilted along the $a^-a^-a^-$ axes (following the Glazer's notation), leading to a Mn-O-Mn bond angle of 166.3° [143–145].

It is therefore clear that any change on the LSMO canonic structure might have implications on its electronic configuration, and hence on its physical properties too, which can be accomplished by the effect of an epitaxial strain [129, 131, 132, 146, 147]. In this chapter, we investigate the physical and structural properties of epitaxial LSMO films grown onto a STO single crystal substrate (which imposes a biaxial tensile strain of 0.7%), with thickness values ranging between 2 and 22 nm. Two additional considerations have to be taken into account in this kind of heterostructures. The first one is that the octahedral network is truncated at the STO/LSMO interface, as the STO lattice presents the idealistic perovskite unit cell structure without octahedral rotations. The second one is that LSMO present a polar stacking along the [001] direction, giving rise to a polar discontinuity at the STO/LSMO interface, as the STO is a non-polar substrate. Theoretical and experimental observations points out that the polar discontinuity generated in similar interfaces, as in the case of the $LaAlO_3/SrTiO_3$ heterostructure [148–151], might induce polar displacements of the B cation or oxygen anions to compensate the internal field. Here, we tackle these two issues among others, like chemical inter-diffusion and strain accommodation.

5.3 Growth process

Three LSMO thin films, with nominal thicknesses of 2, 12 and 22 nm, were fabricated following a chemical solution deposition route (CSD). In this process, stoichiometric amounts of metal acetate precursors are dissolved on acetic acid with a molar concentration of 0.03, 0.1 and 0.3 molar, respectively, respect the Mn content. Then, the solution is stirred at 50 °C for 10 min and spin coated on thermally treated (100) STO single crystal substrates. Finally, the samples are thermally processed in a tubular furnace at 900-1000°C in an oxidizing atmosphere for 10-60 min. Further details of the LSMO fabrication

process are reported elsewhere [152].

The growing conditions were optimized by monitoring the crystal orientation, film surface and film microstructure by means of X-Ray diffraction (XRD), atomic-force microscopy (AFM) and STEM analysis. Fig. 5.4 shows the $\theta - 2\theta$ XRD scans obtained from the 12nm- and a 22-nm thick samples. The XRD scan obtained from the 2 nm-thick sample is not included because no LSMO peaks were identified due to its low signal-to-noise ratio.

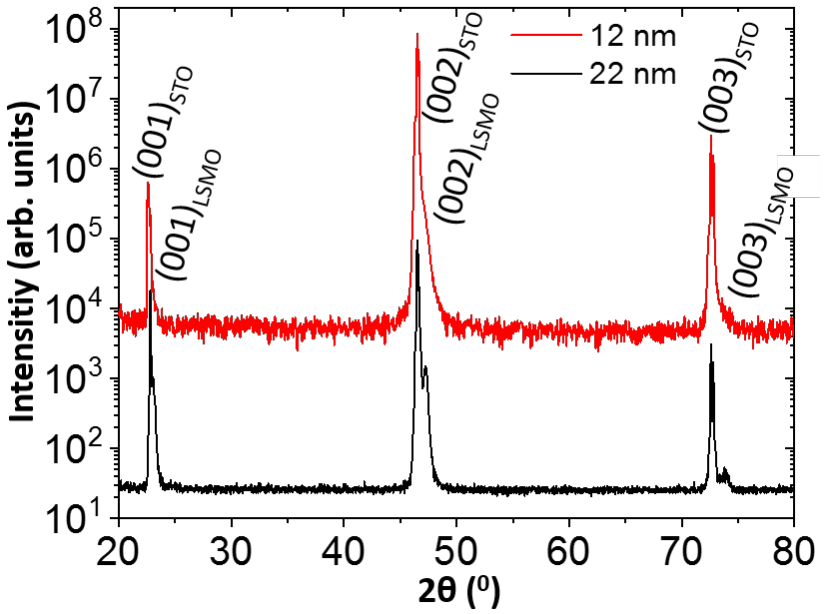

Figure 5.4: θ-2θ XRD spectrum measured from the 22 (black) and 12 nm-thick (red) LSMO films grown onto STO single crystal substrates. The Bragg reflections associated to the $[00l]_{STO}$ and $[00l]_{LSMO}$ family planes are indicated.

The $(00l)_{STO}$ and $(00l)_{LSMO}$ Bragg reflections are clearly identified in the XRD spectrum of the 22 nm-thick film, thus confirming the growth of an epitaxial LSMO film with a c-axis texture. Although this is not so clear in the 12 nm-thick film XRD spectrum, where a low signal-to-noise ratio is

obtained, all the measured $(00l)_{STO}$ peaks have a shoulder that coincides with the expected 2θ values associated to the $(00l)_{LSMO}$ reflections, thus indicating that both films have a similar texture. In addition, no additional Bragg reflections are identified, which is a first evidence of the good film quality, without other secondary phases nor misoriented LSMO grains.

The surface of LSMO films was evaluated by acquiring topological phase-contrast AFM images, which are shown in Fig. 5.5 (a). The substrate surface is observed to be perfectly covered in all cases, even in the thinnest one, thus confirming the continuity of the films. The thinnest film has an averages roughness value of 1 nm.

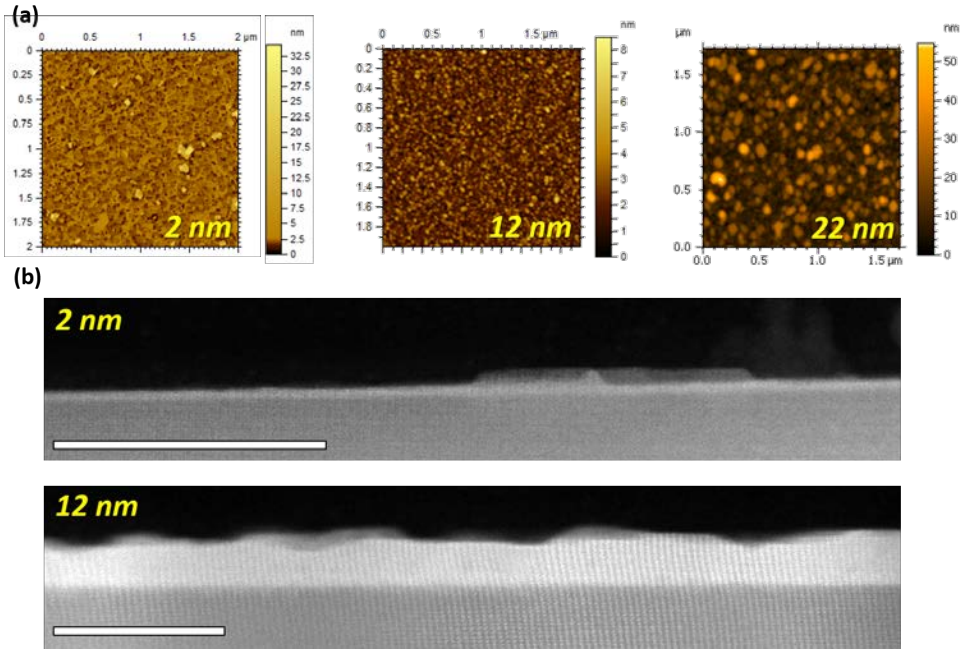

Figure 5.5: (a) From left to rigth: Topological phase-contrast AFM images showing a 2x2 μm^2 film surface region of the 2, 12 and 22 nm-thick LSMO films. (b) Low-magnification cross-sectional Z-contrast images of the 2 and 12 nm-thick LSMO films. Scale bars: 50 nm

The microstructure of the 2 and 12 nm-thick films were further investigated

by acquiring low magnification Z-contrast cross-sectional images, see Fig. 5.5 (b). We have not performed a microstructural analysis of the 22 nm-thick film since we expect that it has a similar microstructure than the 12 nm-thick film because, as it will be shown in the following section, both films present very similar physical properties. In the Z-contrast images of Fig. 5.5 (b), the LSMO films appear brighter than the STO substrate as the image brightness barely scales with Z^2 [14]. A homogeneous contrast is observed within both LSMO films, which confirms that no pores, secondary phases nor misoriented grains are present. Some faceted terraces are formed in both film surfaces. However, we do not expect any significant influence from them on the physical properties of the films.

5.4 Physical properties

In this section, we report the transport and magnetic properties of the fabricated LSMO thin films. Fig. 5.6 (a) shows the magnetization as a function of the external magnetic field cycles of all the studied films at 5 K. All films exhibit similar ferromagnetic-like hysteresis loops at this temperature, even the thinnest one. The magnetization of the 12 and 22 nm-thick films saturates at very similar values, being 575 KA/m and 581 KA/m at 0.3 T, respectively. However, this value decreases down to 420 KA/m in the ultrathin film, which might be ascribed to the larger surface effects. Similar coercive values (around 0.02 T) are identified in all films.

Fig. 5.6 (b) displays the evolution of the magnetization (measured at 0.5 T) with temperature for the three LSMO films. The dashed line indicates the magnetization value of a bulk LSMO crystal at 5K. As in the hysteresis loops of Fig. 5.6 (a), the 12 and 22 nm-thick films exhibit similar magnetization values, for all the measured range of temperatures. However, the maximum magnetization value at 5 K, the one exhibited by bulk LSMO crystals, is only reached in the thickest film. From these curves, we can extract an approximate value of the T_C associated to each film, from the temperature value where the minima appearing in the dM/dT curves are centered. Values of 328, 340 and 300 K are obtained for the 22, 12 and 2 nm-thick films, respectively. All the given values are lower than the T_C value measured in bulk LSMO single crystals (369K) [10].

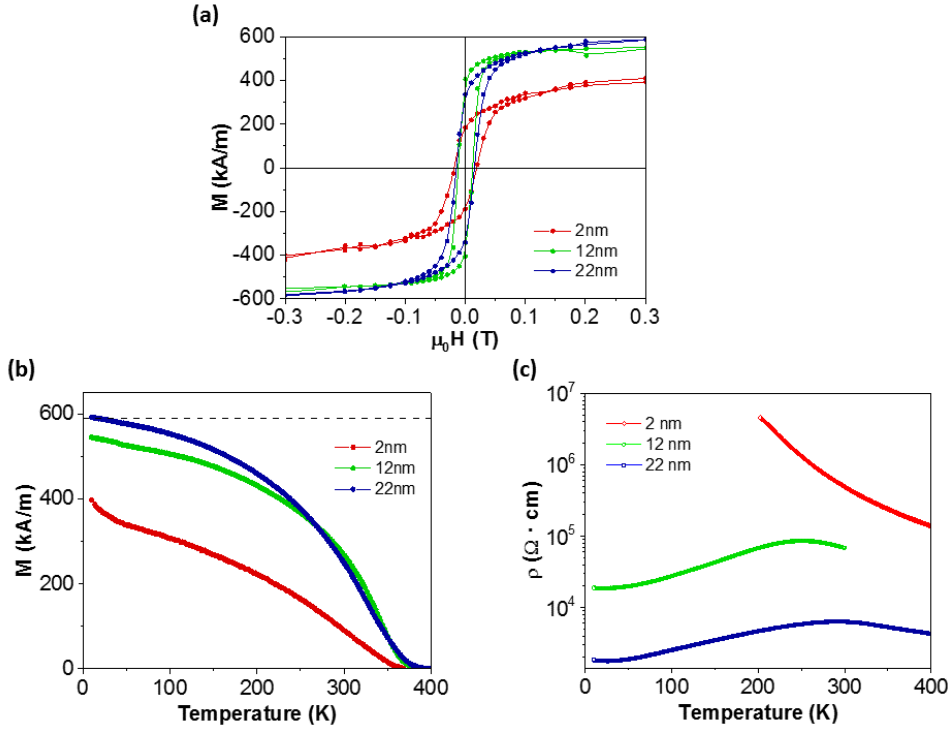

Figure 5.6: Electric and magnetic properties of the studied LSMO thin films. (a) Magnetic moment as a function of the applied magnetic field at 5K. (b) Evolution of the magnetic moment, measured at 0.5 T, as a function of the temperature. (c) Film resistivity as a function of the temperature. The red, green and blue lines correspond to the 2nm-, 12nm- and 22nm-thick LSMO films in (a), (b) and (c).

Fig. 5.6 (c) shows the film resistivity (ρ) as a function of the temperature from the three studied heterostructures. Each film resistivity is measured using a Van der Pauw configuration where four electrodes are placed at the corner positions of the films' surface. The resistivity of the films is observed to increases when the film thickness is reduced. Besides, differently than in LSMO bulk crystals, the 22 and 12 nm-thick films transit from a metallic to an insulating behavior at temperatures close to the T_C, being the metal-insulating temperature shifted from 300 to 250 K when the film thickness is diminished.

Interestingly, the ultrathin film is insulating for all the measured range of temperatures (from 200 to 400 K).

All of these changes might be associated to structural or chemical modifications of the LSMO crystal structure, which should affect its electronic configuration. It is worth remembering that bulk LSMO crystals are always metallic, in both the ferromagnetic and paramagnetic phases [10], and that the appearance of a ferromagnetic-insulating phase contradicts the DE mechanism expected in this compound. This is not the first time that an insulating behavior has been reported [127–129, 153, 154], which has been typically associated to the presence of a dead layer, as both the ferromagnetic moment and the metallic behavior has been observed to almost disappear [127, 155–157]. However, other studies related the emergence of this insulating LSMO phase to the segregation of non-magnetic and insulating phases at the LSMO/substrate interface [132, 153], to orbital reconstruction effects [128, 133] or to the formation of oxygen vacancies [154, 158]. The fact that our CSD-derived ultrathin LSMO film is still ferromagnetic evidences that a different scenario is occurring in our case.

In the following sections, we will show the characterization of the LSMO electronic configuration (by studying the Mn oxidation state), the chemistry (by evaluating the chemical composition) and the atomic structure (by acquiring high magnification Z-contrast and ABF images) of the 12 and 2 nm-thick films. This study will deliver additional clues that might help to understand the appearance of the insulating regime in the ultrathin film case.

5.5 Nuclear magnetic resonance spectroscopy

First, we have investigated the Mn valence of both films by means of nuclear magnetic resonance (NMR) spectroscopy. The NMR spectroscopy allows to probe, at the micrometer length scale, the magnetoelectronic states of the ^{55}Mn cations [131, 132, 159]. The experiment consists of shining the LSMO samples with electromagnetic radiation, for a fixed external magnetic field and temperature conditions, which is absorbed and re-emitted by the ^{55}Mn nuclei at specific resonant frequencies, which give information about their magneto-

electronic states. NMR experiments were carried out at 4.2 K with the use of a coherent broadband spin-echo spectrometer. The spectra were acquired with a driving field applied in plane, without dc magnetic field (H=0). The spin-echo intensity of each spectrum is normalized at the maximum signal value. We have measured the NMR signal from the 22 nm-thick film instead of the 12 nm-thick, as better signal-to-noise ratio was obtained from this sample. However, both films should have analogous spectra as they exhibit very similar magnetic properties. Fig. 5.7 shows the NMR spectra obtained from the 2 (red line) and 22 nm-thick (green line) LSMO films.

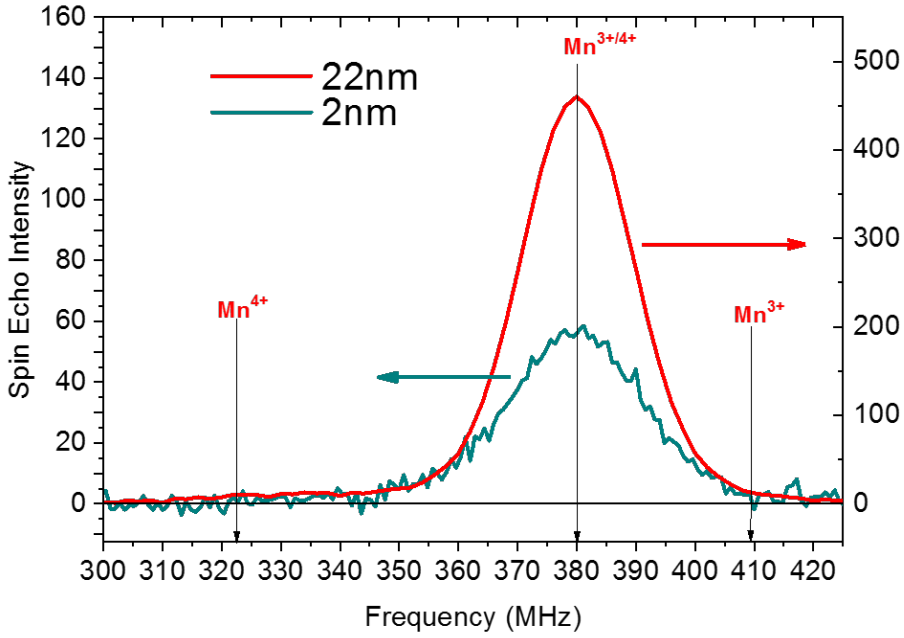

Figure 5.7: ^{55}Mn NMR spectra recorded at 4.2 K from the 2 (green line) and 22 nm-thick (red line) LSMO films. As both films exhibit very different intensity signals, we have used different vertical scale axis, being the left/right-axis corresponding to the 2/22 nm-thick film. The arrows point to the frequency values where the peaks associated to the presence of Mn^{+4}, $Mn^{+3/+4}$ and Mn^{+3} peaks should appear.

Although much less signal is obtained from the ultrathin film, both samples

exhibit analogous spectra. They are composed by a unique Gaussian peak centered at 380 Hz, which is typically ascribed to the presence of mixed $Mn^{+3/+4}$ cations [131, 132]. In the spectrum, we have also indicated the frequency values associated to the presence of Mn^{+4} (320-330 Hz) and Mn^{+3} (410 Hz) clusters [159]. Differently than in previously reported samples, where the Mn^{+4} peak is identified [131, 132], we do not observe any signal from these regions, thus confirming that both LSMO films are only composed by mixed-valence Mn cations, with an intermediate value between +3 and +4. Besides, this Gaussian peak is centered at the same spectral position in both spectra, which signals that the Mn oxidation state is similar in both films.

These results are of great relevance as some of the previous studies ascribe the insulating behavior observed in the thinnest films to the presence of non-metallic Mn^{+4} clusters localized at the substrate/film interface [131]. Here, we have confirmed that this explanation is not valid in our samples, which macroscopically posses mixed Mn valence without Mn^{+4} clusters.

5.6 STEM-EELS characterization

This section is devoted to the structural and chemical characterization of the 2 and 12 nm-thick LSMO films by means of STEM-EELS. First, we have evaluated the microstructure of both films by acquiring the Z-contrast images that are displayed in Fig. 5.8. The 2 nm-thick film is viewed along the <100> zone-axis, see Fig. 5.8, whereas the 12 nm-thick is imaged along the <110> zone-axis, see Fig. 5.8 (b). The nominal thickness of 2 (4-5 unit cells) and 12 nm ($\approx$ 30 unit cells) is confirmed in each film from these images. As previously commented, some faceted terraces are observed onto the surface of the thickest film. Besides, no pores, secondary phases or misoriented grains are observed in any case, resulting in a *c*-axis textured LSMO crystal in both films, following a cube-on-cube relationship with the STO crystal.

As before, the STO/LSMO interfaces (orange arrows) are identified at the position where the image contrast changes, which are observed to be coherent without misfit dislocations. Differently than in the ultrathin film, where the STO/LSMO interface is observed to be sharp, a progressively contrast en-

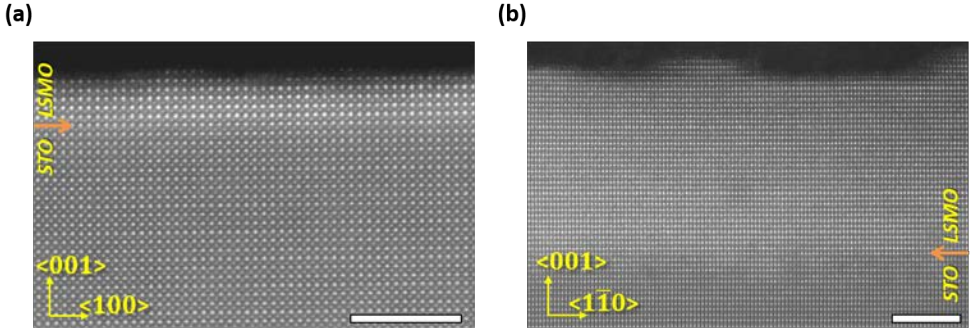

Figure 5.8: Z-contrast images of the (a) 2 and (b) 12 nm-thick LSMO films. (a) and (b) are viewed along the <100> and <110> zone axes, respectively. Orange arrows point to the STO/LSMO interfaces. Scale bars: 5nm.

hancement is identified when crossing from the STO crystal substrate to the 12 nm-thick LSMO film. This contrast gradient might be generated by some cation intermixing at this interface. This have been further studied by acquiring EELS-SI compositional maps.

EELS characterization

The chemical composition of the LSMO films and STO/LSMO interfaces have been evaluated by acquiring atomically-resolved EELS-SI compositional maps, which are shown in Fig. 5.9 (a) and (b) for the 2 and 12 nm-thick films, respectively. From left to right each set of images is composed by a Z-contrast image, the ADF simultaneous image and the corresponding Ti, La and Mn EELS compositional maps. The Sr maps are not shown because we could not get enough signal-to-noise ratio from the Sr L edge, as this spectral feature is placed at much higher energies than the other peaks.

Notice that the brightest columns of the ADF images correspond to the La and Sr cations, whereas the darker ones correspond to the Mn/Ti cations, which have a lower Z value. The sample area from where each EELS-SI has been acquired is marked with a green rectangle in the corresponding Z-contrast image. Each La, Mn and Ti pixel intensity is calculated by integrating the area beneath the La $M_{4,5}$, Mn $L_{2,3}$ or Ti $L_{2,3}$ peaks, respectively. In all cases, the

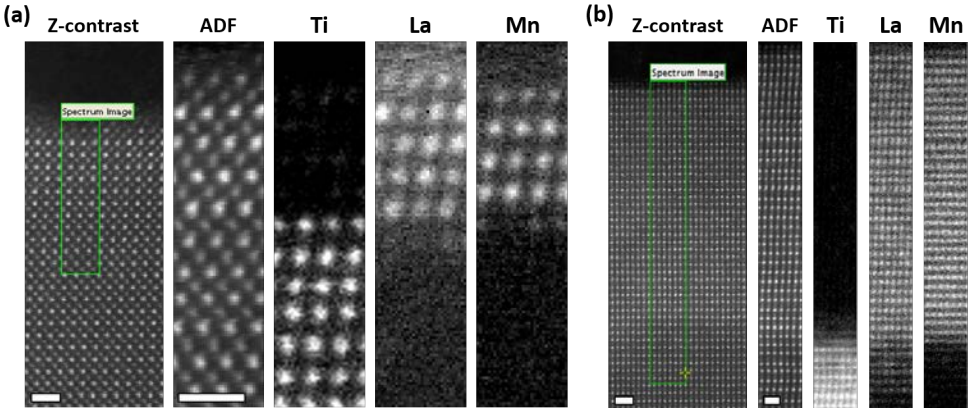

Figure 5.9: From left to right: Z-contrast and Ti, La and Mn EELS-SI compositional maps, obtained from the (a) 2 and (b) 12nm-thick STO/LSMO heterostrucutres. The EEL spectra were acquired from the area delimited by the green squares.

background signal was subtracted by fitting a power law dependency the EEL spectrum before each particular edge. The La and Mn signals are observed to be homogeneous within the films, regardless of their thickness. However, some La diffusion from the LSMO film to the STO substrate is identified in the 12 nm-thick film, which explains the contrast gradient observed at the STO/LSMO interface in the Z-contrast images. We can anticipate here that this La diffusion may emerge as a compensation mechanism to the polar discontinuity generated at the substrate/film interface. However, this will be discussed in more detail in the following pages. However, no Ti diffusion is identified in any film. Accordingly, the STO/LSMO interface is observed to be sharp (as it was revealed by the Z-contrast images) in the ultrathin film, which is composed by a TiO/LaO layer.

The fine-structure of the EEL spectral edges also contains information about the electronic configuration of the crystal. For instance, it is possible to estimate the Mn oxidation state from the spectral features appearing in the O K and Cu L edges [96, 160]. Even though we have previously proved that both films have a similar mixed Mn valence by means of NMR spectroscopy, we have also used EEL spectroscopy to locally probe and compare the oxidation state value of Mn cations within and between the films. It is well known that the Mn

oxidation state value scales with the Mn L_3/L_2 (L_{23}) ratio, being the L_3 and L_2 the integrated area beneath the Mn L_3 and L_2 peaks [96, 160]. Taking this in mind, we have mapped the L_{23} ratio in the ultrathin film. Fig. 5.10 (a) shows a Z-contrast image of the film with the area (green square) from where the EELS-SI was acquired .

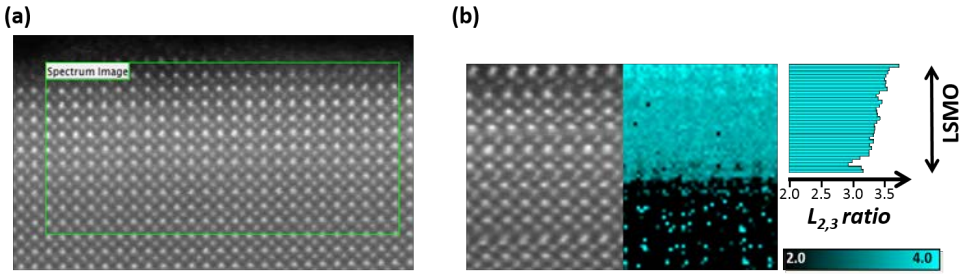

Figure 5.10: (a) Z-contrast image showing the region (green square) of the ultrathin film from where the EELS-SI was recorded. (b) Z-contrast and L_{23} ratio map. The L_{23} ratio depth profile is displayed at the right-side of the color map.

Fig. 5.10 (b) shows the obtained ADF simultaneous image (left-side) and the estimated L_{23} ratio map (right-side), where each pixel intensity scales with the L_{23} ratio value. The L_3 and L_2 values have been estimated following the 2nd derivative approach, which consists of multiplying the amplitude by the full-width at half-maximum of the corresponding peaks extracted from the dI^2_{EELS}/d^2E function [160]. The averaged L_{23} values per each row of pixels is also displayed as a depth-profile histogram. A homogeneous contrast is observed within the map region associated to the film core, with an averaged L_{23} ratio of 3.3 ± 0.2.

A similar analysis has been carried out in the 12 nm-thick film. Fig. 5.11 (a) shows a Z-contrast image of this film with the green squared area from where the EELS-SI has been acquired. The corresponding ADF simultaneous image, L_{23} map and its averaged L_{23} depth-profile are displayed in Fig. 5.11 (b). The L_{23} ratio remains approximately constant when moving along the c-axis direction, with an averaged value of 3.2 ± 0.2. The observed fluctuations are ascribed to the statistical noise. Similar L_{23} mean values have been obtained from both films, thus confirming that they are composed by Mn cations with

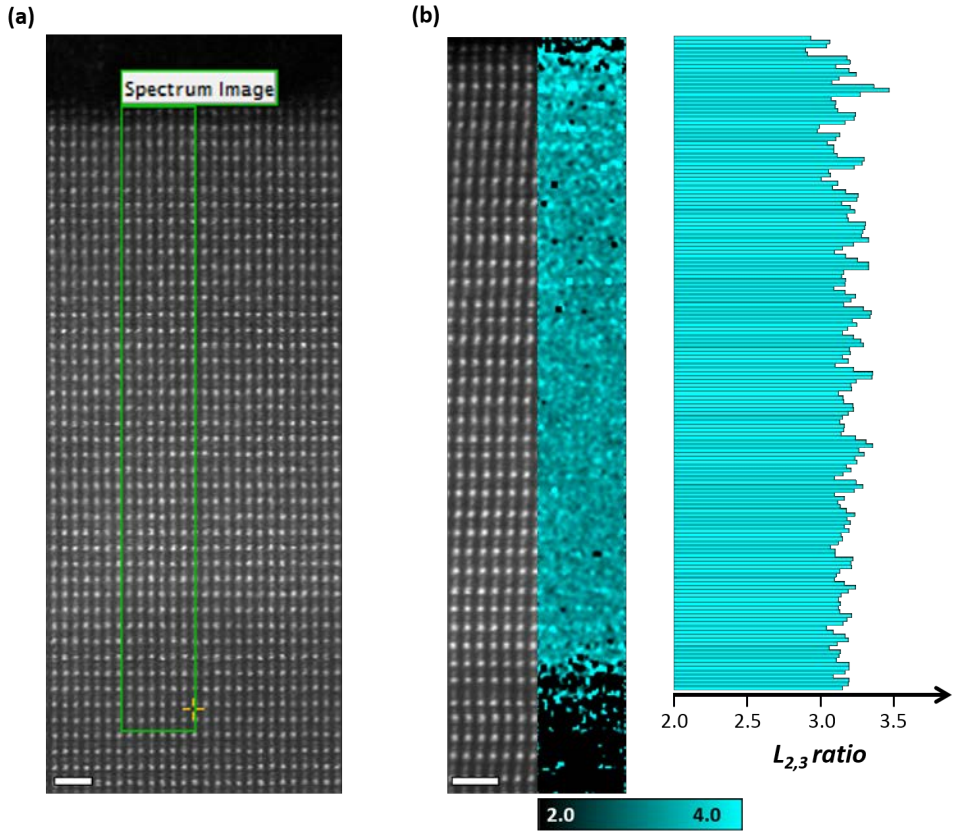

Figure 5.11: (a) Z-contrast image showing the region (green square) of the 12nm-thick film where the Mn oxidation state have been studied by acquiring an EELS-SI. (b) The variation of L_{23} ratio at each position of the image is displayed as a color map. The mean value of each pixel row is also displayed as a vertical profile.

similar mixed-valence.

Unfortunately, the calculated L_{23} ratios cannot be directly correlated with the real Mn oxidation state because we lack the correlation between the 2nd derivative L_{23} ratios with their associated Mn valence state values from the full series of $La_{1-x}Sr_xMnO_3$ bulk compounds to compare with. In order to estimate the real oxidation state value, we have alternatively used the

methodology described by *M. Varela et al.* in Ref. [96]. We have obtained an L_{23} value of 2.6 ± 0.2 when this approach is used, which relates to a Mn oxidation state of 3.28, being this value very close to the expected nominal value (+3.3). The same value is obtained from the 2 nm-thick sample.

Study of the cell parameters

The biaxial tensile strain imposed by the STO substrate, with a mismatch value of 0.7%, may induce deformations on the LSMO unit cell structure. This is investigated by acquiring high resolution Z-contrast images of the 2 and 12 nm-thick LSMO films, which are displayed in Fig. 5.12 (a) and (b), respectively. Notice that the LSMO crystal is viewed along the <100> zone-axis in Fig. 5.12 (a) and along the <110> zone-axis in Fig. 5.12 (b). This is the reason why Mn atoms are placed just below the La/Sr columns in the thickest film. The STO/LSMO interfaces are identified at the vertical position where the image contrast changes, which are indicated with blue dashed lines. From these images, we can directly map the central position of all the viewed atomic columns by using a center-of-mass refinement process, as explained in Chapter 2. The pseudocubic in-plane and out-of-plane LSMO cell parameters are calculated at each unit cell from the La-La interatomic spacings, along both directions, which are estimated from the La/Sr set of coordinates. Instead of showing the obtained maps, in Fig. 5.12 (a) and (b) we have displayed the corresponding averaged in-plane (red triangles) and out-of-plane (blue circles) depth-profiles. Notice that the values obtained from the thickest film, the one viewed along the <110> zone-axis, correspond to the a_{110} parameter, which has been multiplied by $\sqrt{2}$ in order to get the a_{100} parameter that is displayed. We use the substrate STO cells that are located as far as possible from the STO/LSMO interface to calibrate the obtained values.

Both LSMO layers adopt the in-plane parameter of the STO crystal, which is kept constant up to the surface of the films. This indicates that the LSMO unit cell is enlarged along the basal direction due to the imposed tensile strain. Otherwise, the out-of-plane parameter is observed to be lower than the LSMO bulk value, which is indicated with a dashed line ($a_{LSMO} = 3.871$Å). In

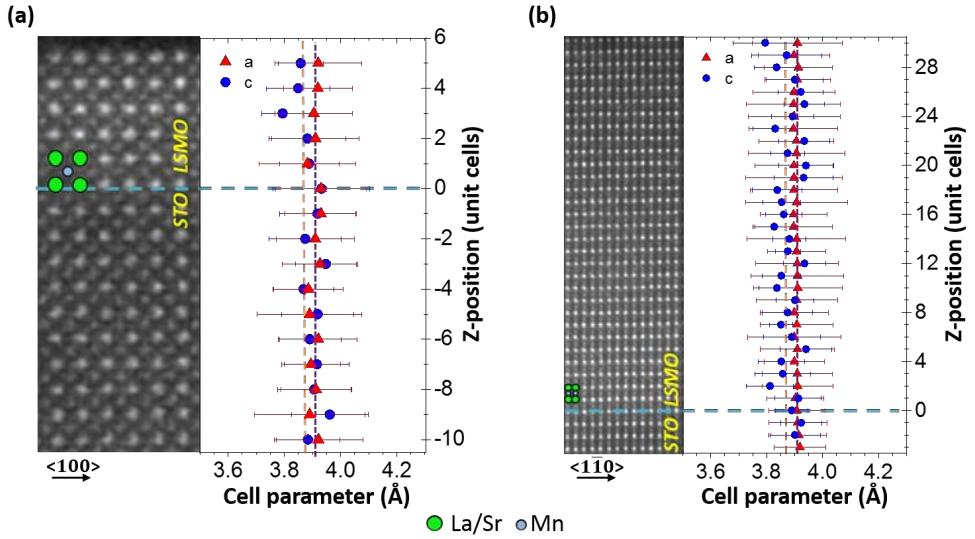

Figure 5.12: In-plane (red triangles) and out-of-plane (blue circles) cell parameters as a function of the Z-position measured in the (a) 2 and (b) 12nm-thick LSMO films. The blue dashed lines represent the STO/LSMO interface. The STO and LSMO cell parameters are indicated as red and orange dashed lines, respectively.

the 2 nm-thick film, the averaged out-of-plane value is found to be 3.854 Å, which evidences an out-of-plane shrinkage of the LSMO unit cell following a Poisson-like deformation. On the other hand, in the thickest LSMO film, the out-of-plane parameter is observed to randomly oscillate between a mean value of 3.846 Å, which is also lower than the LSMO bulk parameter.

ABF characterization

We will now focus our attention into the characterization of the octahedral MnO_6 units. It is mandatory to study how the octahedral units are arranged in the LSMO structure of both films as the LSMO physical properties are strongly influenced by the Mn-O bond length and angle. It is worth remarking that the octahedral network has a discontinuity at the STO/LSMO interface, as they are tilted along the $a^-a^-a^-$ axes in the LSMO structure and no

octahedral rotations are present in the STO lattice. The investigation that was carried out in Ref. [147] constitutes an example of how the LSMO physical properties are influenced by the modification of the octahedral tilts. In this work, the authors report a deterioration of the ferromagnetic moment of the LSMO crystal as a result of the octahedral modifications occurring in LSMO/STO superlattices. Besides, the octahedral response might also depend on the LSMO film thickness because the spatial confinement might also play a role, as reported by J. Gázquez et al. [151] for the LAO/STO heterostructure. Here, we have accessed to the oxygen sub-lattice by acquiring series of annular bright-field (ABF) and Z-contrast images, which permits to directly image the heavier and oxygen atomic columns at the same time.

Fig. 5.13 (a) shows two simultaneously acquired ABF and a Z-contrast images of the 12 nm-thick LSMO film, which is viewed along the <110> zone-axis. The STO/LSMO interface is identified from the Z-contrast image at the vertical position where the image contrast start to decrease (orange arrow). Notice that the ABF images have the opposite contrast than the Z-contrast ones, being the atomic columns dark spots surrounded by a bright environment. The ABF image reveals those oxygen anions (red circles) that are placed between neighboring Mn cations.

As the octahedral rotations, also referred to as antiferrodistortive (AFD) tilts, turns along the $a^-a^-a^-$ axes in the LSMO crystal, we have to orient the LSMO crystal along the <110> zone-axis to easily visualize the tilts. The reason why we have to use this particular orientation is sketched in Fig. 5.13 (b), where it is illustrated a representative picture of the LSMO crystal viewed along both the <110> and <100> zone-axes. In the first case, the projection of all the oxygen atoms lying at the same atomic column is placed at the same image position, as the oxygen octahedra rotate in phase along the viewing axis. On the contrary, when the LSMO is viewed along the <100> zone-axis, the adjacent oxygen octahedra rotate in opposite directions and hence the projection of all the oxygen atoms belonging to the same atomic column results in an elongated rod. Fig. 5.13 (c) corresponds to a contrast-inverted ABF image of a central region of the 12 nm-thick LSMO film (yellow square in Fig. 5.13 (a)), which has been amplified. When the crystal is viewed along

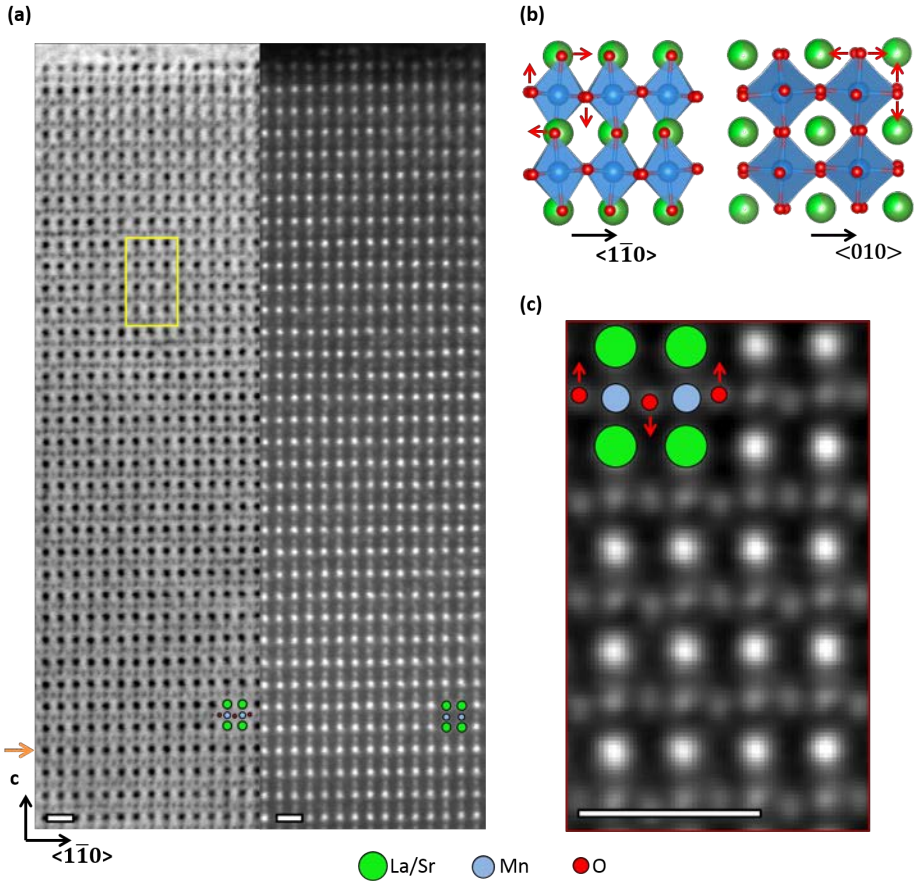

Figure 5.13: (a) ABF and Z-contrast images of the 12 nm-thick LSMO film viewed along the <110> zone-axis. The ABF region within the yellow square is magnified in (c) with the contrast inverted. Scale bars: 1 nm (c) Sketch of the MnO_6 octahedral units when they are viewed along the <110> or <100> zone-axis. .

the <110> zone-axis, the Mn columns (blue circles) are placed just above and below the La/Sr cations (green circles). Notice that the oxygen columns are perfectly viewed between Mn cations, being them shifted upwards and downwards when moving along the basal direction. As sketched in Fig. 5.13 (b), this rippling pattern corresponds to the projection of the AFD tilts along the <1$\bar{1}$0> axis. Hence, the MnO_6 units of the 12 nm-thick LSMO film

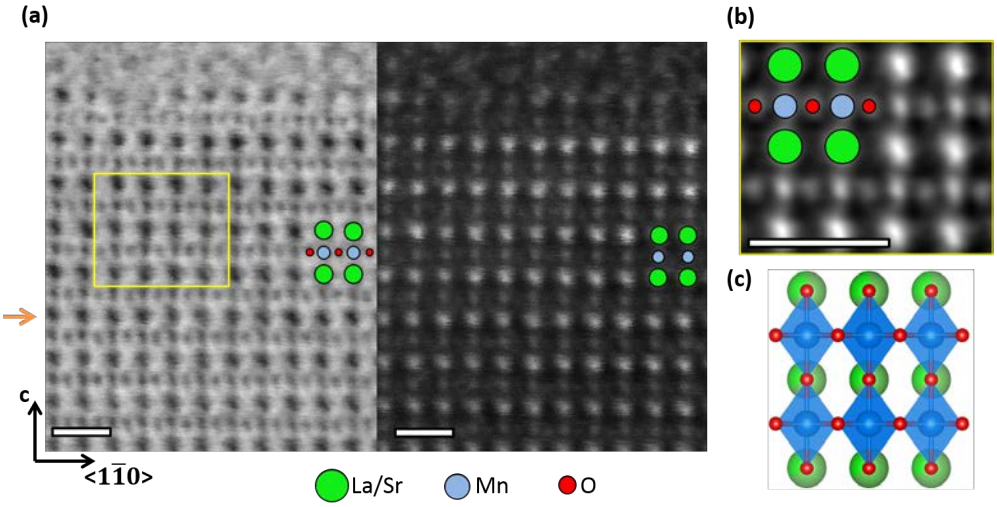

Figure 5.14: (a) ABF and Z-contrast images of the 2 nm-thick LSMO film viewed along the <110> zone-axis. The orange arrow points to the STO/LSMO interface. The image area marked with a yellow square is magnified in (b) with the contrast inverted. (c) Sketch of the MnO_6 octahedral unit that is viewed in (b). Scale bars: 1 nm.

present similar rotations than the ones observed in bulk LSMO crystals.

Fig. 5.14 (a) shows an ABF and Z-contrast images of the ultrathin LSMO film. As before, we have oriented the crystal along the <110> zone-axis in order to better identify the AFD tilts. The STO/LSMO interface is indicated with an orange arrow. The image area delimited by the yellow square is amplified with the contrast inverted in Fig. 5.14 (b). The characteristic rippling pattern displayed by the oxygen columns (red circles) disappears in this film, being the oxygen atoms placed in the same basal plane than the Mn cations (blue circles). This means that the AFD tilts are suppressed in the 2 nm-thick LSMO film, as it is sketched in Fig. 5.14 (c).

We have further evaluated the presence of AFD tilts by identifying the central position of all the distinct atomic columns that are present in the previous ABF images. We have used the same iterative process than before,

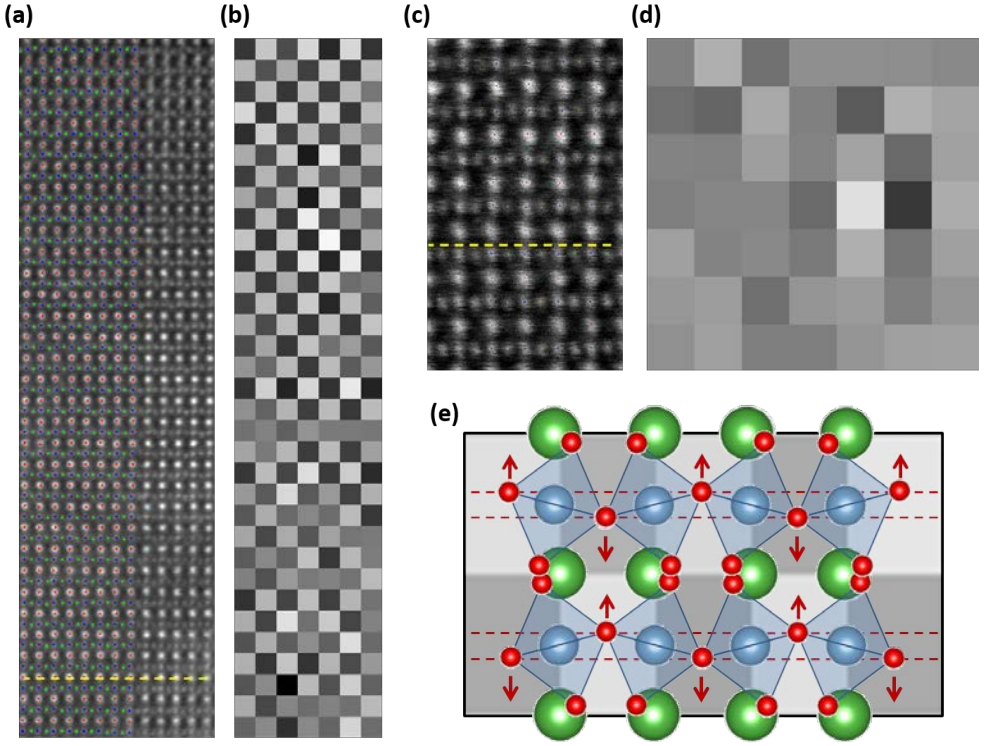

Figure 5.15: Contrast-inverted ABF images of the (a) 2nm- and (c) 12nm-thick LSMO filmm. (b,d) Relative vertical displacement between adjacent oxygen atoms calculated from the ABF images shown in (a) and (b), respectively. (e) Illustration of the octahedral configuration with AFD rotations that generate the observed chessboard-like pattern in (d). The yellow dashed lines indicate the STO/LSMO interfaces.

getting a set of coordinates for all the viewed atomic sub-lattices. The obtained La (red crosses), Mn (blue crosses) and O (green crosses) positions from the 12 nm-thick film are superimposed onto the contrast-inverted ABF image shown in Fig. 5.15 (a). From the oxygen set of coordinates, we study the presence of AFD tilts by calculating the relative vertical shifts between the neighboring oxygen atoms that are located at the same basal plane. The resulting diagram is displayed in Fig. 5.15 (b), where each square represents one oxygen atom whose intensity scales with the relative out-of-plane shift respect its right-sided oxygen, as sketched in Fig. 5.15 (e). Dark/bright

contrast relates to negative/positive shift whereas gray color indicates that both oxygens are confined at the same plane. The obtained pattern resembles a chessboard in the whole film. This type of arrangement arises when oxygens are successively shifted upwards and downwards following the rippling pattern that has been previously observed in Fig. 5.13 (c), which further confirms the presence of AFD tilts in the thickest LSMO film. Besides, the difference in contrast between adjacent squares seems to be more pronounced close to the surface of the film than near the STO/LSMO interface, indicating that larger shifts are present within the film surface areas. Unexpectedly, the octahedral tilts do not disappear at the STO/LSMO interface, being them transfered towards the STO substrate, where a similar chessboard-like pattern is also identified. Fig. 5.15 (c) is a high magnification contrast-inverted ABF image of the ultrathin film, with the superimposed La (red crosses), Mn (blue crosses) and O (green crosses) positions. The same kind of diagram, regarding the estimation of the vertical oxygen shifts, is shown in Fig. 5.15 (d). In this sample, we do not observe the chessboard-like pattern, thus confirming that all oxygen atoms are confined at the same basal plane.

The penetration depth of the AFD tilts within the STO substrate in the thickest LSMO film is further evaluated by acquiring another high resolution ABF image, where more substrate cells are included in detriment of the upper LSMO cells, which is shown with the contrast inverted in Fig. 5.16 (a). The red dashed-line indicates the STO/LSMO interface. As before, we have identified the La (red crosses), Mn (blue crosses) and O (green crosses) atomic set of coordinates, which are superimposed onto the contrast-inverted ABF image of Fig. 5.16 (b). From the oxygen set of coordinates, we calculate the diagram associated to the relative oxygen shifts, which is shown in Fig. 5.16 (c). As expected, we obtain a similar chessboard-like diagram than the one shown in Fig. 5.15 (d), thus denoting the presence of AFD tilts. As previously observed, the octahedral rotations do no vanish at the STO/LSMO interface, but they are transferred to the uppermost substrate cells. This chessboard pattern disappears after approximately four unit cells below the interface, where the STO crystal recovers its canonic structure (without AFD tilts).

From the oxygen set of coordinates, we can also estimate the Mn-O-Mn

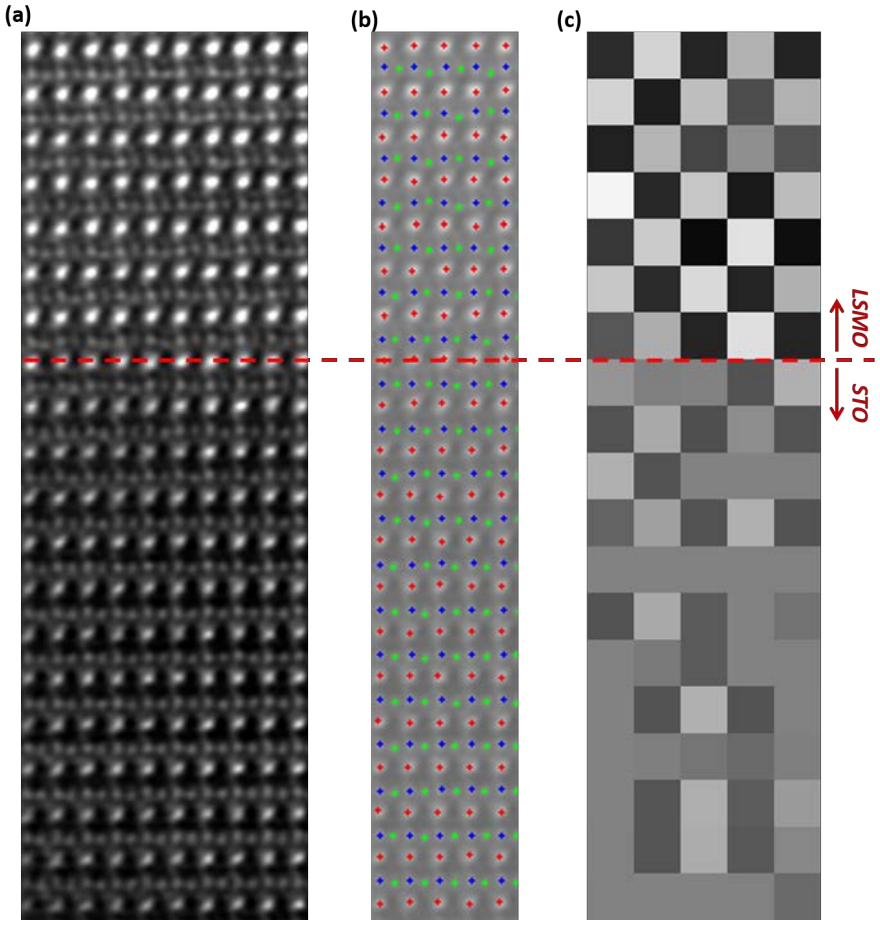

Figure 5.16: (a) Contrast-inverted ABF image showing the STO/LSMO interface from the 12 nm-thick LSMO film. (b) Contrast-inverted ABF image where the central positions of the La, Mn, and O atomic columns are indicated with red, blue and green crosses. (c) Relative vertical oxygen shifts measured from the contrast-inverted ABF image shown in (a)

angle (θ), which affects the electronic configuration of the LSMO compound [7, 147, 161]. As a first approximation, we can estimate the θ angle from the α angle, defined as the angle formed by the octahedral base line and the $[1\bar{1}0]$ direction, as sketched in Fig. 5.17 (a). Assuming that the Mn cations

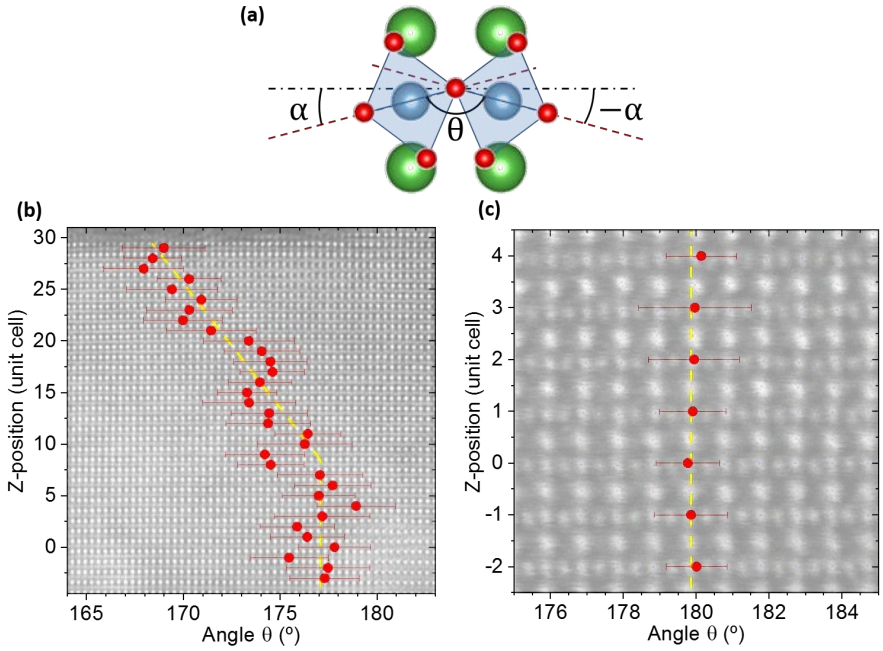

Figure 5.17: (a) Illustration of the LSMO unit cell viewed along the <110> zone-axis, where the α and θ angles are represented. Depth-profiles of the measured θ angle in the (b) 12 and (c) 2 nm-thick LSMO films. The dashed yellow lines are a visual help for the eye.

are placed at the central positions of the octahedra, the θ parameter can be easily obtained by subtracting from 180° the two measured absolute α values (the positive and the negative ones). In Fig. 5.17 (b), we directly plot the depth-profile of the θ angle that has been measured in the 12 nm-thick film. The largest θ value is found at the STO/LSMO interface with a value of (177 ± 2)°, being it lower than the 180° expected from the STO structure. This θ value is kept constant until approximately 7 unit cells far from the STO/LSMO interfarce, where it starts to linearly decrease until the film surface is reached, where a value of 168 ± 2° is measured. This θ value is very close to that from the relaxed bulk structure (166.3°). Therefore, the system needs approximately 30 u.c. to recover the AFD tilts that are present in the bulk structure [145].

Fig. 5.17 (c) shows the depth-profile of the θ angle from the ultrathin film. A constant θ value of 180° is obtained in the whole film, *i.e.* no octahedral tilts are identified within this ultrathin LSMO film. We can therefore conclude that the LSMO unit cell is strongly distorted in this ultrathin film, where the LSMO structure adopts both the in-plane parameter and the octahedral arrangement of the underlying STO crystal.

As the polar discontinuity generated at the STO/LSMO interface might induce additional polar distortions within the LSMO structure, we have investigated the presence of atomic shifts in both films which, except some exceptions (e.g. $BiFeO_3$), tend to compete with the occurrence of AFD tilts in most perovskite oxides [162]. In particular, we have measured the off-centering Mn (δ_{Mn}) and O (δ_{Mn}) vertical shifts, respect the central position of the unit cell calculated from the La positions. The obtained δ_{Mn} (blue) and δ_O (red)

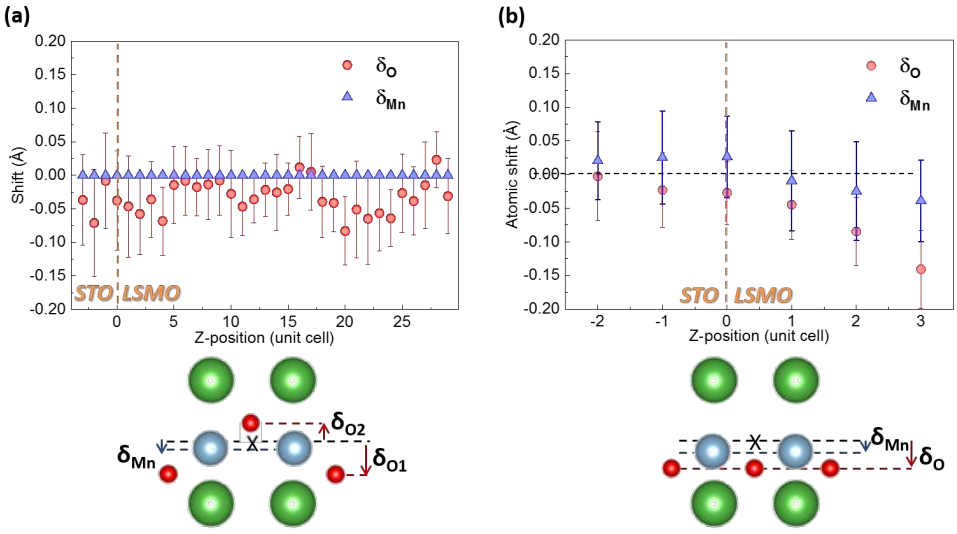

Figure 5.18: Measured relative displacement of the Manganese columns (blue triangles) and Oxygen columns (red circles) respective the center of mass of each unit cell. A polar distortion pointing towards the STO/LSMO interface is only observed in the thinner case.

depth-profiles of the thickest film are plotted in Fig. 5.18 (a).

The Mn cations are perfectly placed at the central position of the LSMO unit cell ($\delta_{Mn} = 0$). On the contrary, the oxygen atoms are slightly shifted downwards at the interfaces of the film, where the polar/non-polar interfaces are placed (STO/LSMO and LSMO/void). This kind of octahedral shift has been recently reported by *S. Koohfar et al.* for a similar STO/LSMO heterostructure, where a Sr content of 0.2 and an LSMO layer thickness of 10 unit cells are used[163]. The authors pointed out that the octahedral units shift to compensate the polar discontinuity. Concomitantly to this shift, the authors also identify chemical intermixing of La, as we do. They also attributed this effect to a polar compensation mechanism [163, 164].

The presence of polar modes are also investigated in the ultrathin film. The measured δ_{Mn} (blue) and δ_O (red) depth-profiles are plotted in Fig. 5.18 (b). In this film, both the oxygen and manganese atoms are also progressively shifted downwards as we move along the *c*-axis direction far from the interface. It is worth remembering that no La intermixing is identified in this thinner heterostructure, being these atomic shifts the unique appearing mechanism that compensates the polar discontinuities emerging at the interfaces of the LSMO film, as observed in the LAO/STO interfaces [151].

It is clear that the spatial confinement and the presence of an internal electric field due to the polar discontinuity modifies the tilt pattern of the LSMO film, however, this result does not still clarify why this film is insulating while it is ferromagnetic.

5.7 Discussion and summary

In this chapter we have investigated the physical and structural properties of two biaxially textured LSMO films, grown by CSD onto STO single crystal substrates with thicknesses ranging between 2-22 nm. While the LSMO bulk properties (ferromagnetic and metallic) are preserved in the thickest films (12 and 22 nm), the ultrathin film (2nm) is insulating for all the measured range of temperatures although keeping a similar ferromagnetic behavior,

which contradicts the DE mechanism expected for this compound. We have confirmed, by means of NMR and EEL spectroscopy, that all the studied samples have a similar Mn mixed oxidation state value close to the nominal +3.3 value, thus discarding the possibility of having non-metallic Mn^{+4} aggregations. Regarding the structural characterization, we have observed that the tensile strain imposed by the STO substrate enlarges the LSMO unit cell structure along both basal directions, inducing a compression along the out-of-plane direction.

The more noticeable difference that has been identified between both films is their distinct octahedral behavior. While the AFD tilts are still present in the thickest film, they are suppressed in the ultrathin film case. Even though one might think that this AFD suppression should increase the conductivity, because of the Mn-O bond length narrowing resulting in a larger shell overlapping, the real scenario behind this phenomenology is more complex. Besides, one have to take into account that the oxygen octahedra might be distorted as the AFD tilts are suppressed and the LSMO structure is expanded along the in-plane direction. Although this kind of distortion should favors the population of the in-plane $d_{x^2-y^2}$ orbitals [146], promoting the electronic delocalization, it is mandatory to simulate the density of states of the distorted LSMO unit cell structure that is here described to understand why it transits towards an insulating behavior.

Finally, we have also observed the emergence of polar distortions, which appear to compensate the non-polar/polar interfaces located at the film edges (STO/LSMO/void) in both films. Besides, we have also identified an intermixing of La at the LSMO/STO interface of the thickest film, which constitutes a second mechanism that help to compensate the polar discontinuity.

Chapter 6

Summary and general conclusions

The continuous development of novel and complex devices for fulfilling the market demands is becoming more complex over time because of the wholly exploitation of the available bulk materials. One possibility to accomplish novel devices possessing new functionalities is by engineering epitaxial heterostrucutres, in the nanometric scale, where the properties of the used compounds can be modified because of their mutual interaction. When these heterostructures are made of perovskite oxides, the strong interplay between the lattice, spin, orbit and charge degrees of freedom lead to a huge range of fascinating properties that can be tailored by the subtle structural modifications induced by strains. In order to understand the underlying physics behind these phenomena, it is crucial to know the real structure of the emerging lattice defects or distortions within these kind of structures. For this reason, new techniques capable of analyzing these systems, in the real space with atomic resolution, are required.

The development of the aberration-corrected STEM-EELS marked a notable breakthrough as it permits to directly see, without the need of simulations, the real structure of complex non-periodical structures, such as defects or interfaces, in real space with sub-atomic resolution. In this work, we address three paradigmatic examples of strain-driven structural distortion appearing in one of the most studied family of functional oxides materials, this is the perovskite oxides. In particular, we investigate the generated distortions within the YBCO, LSMO and RNO lattices induced by the presence of crystalline defects, the substrate mismatch or spatial confinement effects.

Experimental results

The main conclusions that are derived from this work are summarized below:

The challenging YBCO microstructure

We have studied the YBCO microstructure of spontaneously segregated NC (ss-NC) films, where randomly oriented NPs are trapped within the YBCO host matrix. The incoherent interface between the NPs and the YBCO matrix promotes the formation of the Y124 intergrowth defect. The partial dislocation located at the perimeter of this planar defect strains its surrounding YBCO unit cells, acting as a novel pinning mechanism for the magnetic vortices. We have further evaluated the microstructure of mixed ss-NC films where two kind of NPs are introduced within the same YBCO ss-NC film. No significant microstructural and electrical differences were observed compared to single ss-NC films. Besides, we have estimated the density and length of the most abundant defect, the Y124 intergrowth, that is present in all the studied films. A linear correlation between the density of strained areas, localized around the Y124 intergrowth edges, and the B* parameter was observed, thus confirming that these areas act as a novel pinning mechanism for the magnetic vortices. Finally, we have investigated the microstructure of preformed nanoparticle NC (pn-NC) films, where a precursor colloidal solution is used that contain both the YBCO precursor phases and the previously synthesized oxide-based NPs. We have successfully achieved similar structural and superconducting properties than in the ss-NC films, but with an enhanced control on the NP properties. This allowed to increase the film thicknesses up to 1 μm and to develop the flash heating approach, which permitted to accelerate the YBCO growth rate.

We have further analyzed in detail the real structure of the Y124 intergrowth defect. We have observed that the Y123 stoichiometry is preserved in the YBCO NC films despite the presence of abundant Cu-O double chain layers. This is accomplished by the formation of pairs of Cu vacancies that are buried into the very same Y124 intergrowth defect. In addition, we have observed the presence of a periodic and uneven array of oxygen vacancies within the BaO planes at those Y123 unit cells surrounding the Y124 intergrowths. DFT-calculations

have predicted that similar formation energies are needed to introduce one V_O either within the Cu-O single chain layer or BaO plane positions. Besides, the relaxed structure containing V_O vacancies within the BaO planes was observed to be more compressed along the c-axis direction than the one containing V_O within the Cu-O single chain layer. This result suggested that the appearance of V_O within the BaO planes compensates the structural expansion occurring at the Cu-O double chain layer. We have also observed that the presence of these V_O within the BaO planes induces additional structural distortions within the Y123 unit cell structure. In particular, we have identified a narrowing of the spacings between the superconducting planes and between the upper Ba cation and its nearest Y atom. Regarding the oxygen sub-lattice, we have identified an increase of the superconducting-apical spacing and an enlargement of the superconducting buckling angle. Although it still remains unclear how these distortions influence the physical properties of the YBCO, they might induce changes on the YBCO electronic configuration, and hence on the YBCO superconducting properties, as subtle differences are observed at both the O K and Cu L EELS fine-structures.

Strain accommodation mechanisms in epitaxial $LaNiO_3$ and $NdNiO_3$ thin films

We have investigated the defect landscape of RNO films that are grown onto LSAT and LAO single crystal substrates, which induce either a tensile or compressive-strain, respectively. We have observed the appearance of misfit dislocations when both film and substrate share the same crystallographic structure (rhombohedral), whereas Ruddlesden-Popper faluts (RPF) are generated in the other scenarios. We have found that the density of these faults increases with the substrate mismatch value, being a relaxation mechanism of the epitaxial strain induced by the substrate mismatch. Besides, the remaining Ni excess resulting form the formation of RPFs leads to the generation of NiO aggregates that are pushed up to the films' surface. We have also identified the presence of concomitant structural distortions at those unit cells adjoining the RPFs, being these cells compressed along the perpendicular direction of the fault and their Ni cations shifted far from the unit cell central positions towards the fault. We have also measured the transport properties of the fabricated films. A shift of the MIT onset towards lower temperatures was observed

when films were compressively strained. The presence of RPFs was observed to be detrimental for the electrical conduction as an increase of the film resistivity was identified when the RPF density was enhanced.

Structural and physical properties of LSMO ultrathin films

Finally, we have evaluated the effects of the spatial confinement in epitaxial LSMO films that are grown onto a STO single crystal substrates. A transition from a metallic-ferromagnetic to an insulating-ferromagnetic phase was observed when the LSMO film thickness was reduced from 12 to 2 nm, which contradicts the double-exchange mechanism expected for this compound. Differently than in previous reports, NMR and EELS spectroscopy have confirmed that all the studied films had a similar mixed Mn valence, without the presence of non-metallic Mn^{+4} clusters. The study of their atomic-structure by STEM-EELS have revealed significant structural differences between them. While the oxygen octahedra were tilted along the $a^-a^-a^-$ axes in the 12 nm-thick film, showing a Mn-O-Mn angle gradient from 176° (LSMO/STO interface) to 168° (film surface), no octahedral tilts were identified in the 2 nm-thick film. We have also observed the presence of polar distortions in both films, which were ascribed to appear in order to compensate the polar discontinuity generated at the interface between the non-polar STO and the polar LSMO compound. Besides, some La inter-diffusion from the LSMO film to the STO substrate was identified in the 12 nm-thick film, which was also ascribed to appear to compensate the STO/LSMO polar discontinuity. Even though further investigations are needed to understand the observed decoupling between the ferromagnetism and conductivity in the 2 nm-thick film, the structural differences between the 2 and 12 nm-thick films that are described in this chapter provide new perspectives to understand this complex and still unsolved phenomenology.

Bibliography

[1] P. A. Cox. *Transition Metal Oxides: An Introduction to their Electronic Structure and Properties*. OUP Oxford, 2010.

[2] M. Imada, A. Fujimori, and Y. Tokura. Metal-insulator transitions. *Rev. Mod. Phys.*, 70(4):1039–1263, 1998.

[3] Y. Tokura and N. Nagaosa. Orbital Physics in Transition Metal Oxides. *Science*, 288(5465):462–468, 2000.

[4] E. Dagotto. Complexity in Strongly Correlated Electronic Systems. *Science*, 309(5732):257–262, 2005.

[5] E. Dagotto and Y. Tokura. Strongly Correlated Electronic Materials: Present and Future. *MRS Bulletin*, 33(11):1037–1045, 2008.

[6] M. K. Wu, J. R. Ashburn, C. J. Torng, P. H. Hor, R. L. Meng, L. Gao, Z. J. Huang, Y. Q. Wang, and C. W. Chu. Superconductivity at 93 K in a new mixed-phase Y-Ba-Cu-O compound system at ambient pressure. *Phys. Rev. Lett.*, 58(9):908–910, 1987.

[7] E. Dagotto, T. Hotta, and A. Moreo. Colossal magnetoresistant materials: the key role of phase separation. *Physics Reports*, 344(1):1–153, 2001.

[8] Y Tokura and Y Tomioka. Colossal magnetoresistive manganites. *Journal of Magnetism and Magnetic Materials*, 200(1):1 – 23, 1999.

[9] A. Von Hippel. Ferroelectricity, domain structure, and phase transitions of barium titanate. *Reviews of Modern Physics*, 22(3):221–237, 1950.

[10] A. Urushibara, Y. Moritomo, T. Arima, A. Asamitsu, G. Kido, and Y. Tokura. Insulator-metal transition and giant magnetoresistance in $La_{1-x}Sr_xMnO_3$. *Phys. Rev. B*, 51(20):14103–14109, 1995.

[11] S. Catalano, M. Gibert, J. Fowlie, J. Iñiguez, J. M. Triscone, and J. Kreisel. Rare-earth nickelates $RNiO_3$: Thin films and heterostructures. *Reports on Progress in Physics*, 81(4):046501–046528, 2018.

[12] M. Varela, A.R. Lupini, K. Van Benthem, A.Y. Borisevich, M. F. Chisholm, N. Shibata, E. Abe, and S. J. Pennycook. Materials Characterization in the Aberration-Corrected Scanning Transmission Electron Microscope. *Annual Review of Materials Research*, 35(1):539–569, 2005.

[13] D. B. Williams and C. B. Carter. *Transmission Electron Microscopy: A Textbook for Materials Science.* Springer, 2nd edition, 2009.

[14] S. J. Pennycook and P. D. Nellist. *Scanning transmission electron microscopy: Imaging and Analysis.* Springer-verlag gmbh edition, 2011.

[15] R. Egerton. *Electron Energy-Loss Spectroscopy in the Electron Microscope.* Springer edition, 2011.

[16] W. Sigle. Analytical Transmission Electron Microscopy. *Annual Review of Materials Research*, 35(1):239–314, 2005.

[17] O. L. Krivanek, N. Dellby, and A. R. Lupini. Towards sub-Å electron beams. *Ultramicroscopy*, 78(1):1–11, 1999.

[18] O. L. Krivanek, P. D. Nellist, N. Dellby, M. F. Murfitt, and Z. Szilagyi. Towards sub-0.5 angstrom electron beams. *Ultramicroscopy*, 96(3-4):229–237, 2003.

[19] D. A. Muller, N. Nakagawa, A. Ohtomo, J. L. Grazul, and H. Y. Hwang. Atomic-scale imaging of nanoengineered oxygen vacancy profiles in $SrTiO_3$. *Nature*, 430(7000):657–661, 2004.

[20] V. Grillo and F. Rossi. A new insight on crystalline strain and defect features by STEM-ADF imaging. *Journal of Crystal Growth*, 318(1):1151–1156, 2011.

[21] P. J. Phillips, M. De Graef, L. Kovarik, A. Agrawal, W. Windl, and M. J. Mills. Atomic-resolution defect contrast in low angle annular dark-field STEM. *Ultramicroscopy*, 116:47–55, 2012.

[22] R. Guzman, J. Gázquez, B. Mundet, M. Coll, X. Obradors, and T. Puig. Probing localized strain in solution-derived $YBa_2Cu_3O_{7-\delta}$ nanocomposite thin films. *Phys. Rev. Materials*, 1(2):024801–024807, 2017.

[23] E. Okunishi, I. Ishikawa, H. Sawada, F. Hosokawa, M. Hori, and Y. Kondo. Visualization of light elements at ultrahigh resolution by STEM annular bright field microscopy. *Microscopy and Microanalysis*, 15(S2):164–165, 2009.

[24] R. Ishikawa, E. Okunishi, H. Sawada, Y. Kondo, F. Hosokawa, and E. Abe. Direct imaging of hydrogen-atom columns in a crystal by annular bright-field electron microscopy. *Nature Materials*, 10(4):278–281, 2011.

[25] Pennycook T. PhD thesis: Density functional theory and scanning transmission electron microscopy: synergistic tools for materials investigation. *Vanderbilt University*, 2012.

[26] M. Bosman, M. Watanabe, D.T.L. Alexander, and V.J. Keast. Mapping chemical and bonding information using multivariate analysis of electron energy-loss spectrum images. *Ultramicroscopy*, 106(11-12):1024–1032, 2006.

[27] I. T. Jolliffe. *Principal component analysis*. Springer, 2nd edition, 2002.

[28] D. Pesquera. PhD thesis: Strain and interface-induced charge, orbital and spin orderings in transition-metal oxide perovskites. *Universitat Autónoma de Barcelona (UAB)*, 2014.

[29] P. Hohenberg and W. Kohn. Inhomogeneous Electron Gas. *Phys. Rev. B*, 136(3B):B864–B871, 1964.

[30] P. E. Blöchl. Projector augmented-wave method. *Physical Review B*, 50(24):17953–17979, 1994.

[31] J. P. Perdew, K. Burke, and M. Ernzerhof. Generalized gradient approximation made simple. *Physical Review Letters*, 77(18):3865–3868, 1996.

[32] G. Kresse and J. Hafner. Ab initio molecular dynamics for open-shell transition metals. *Phys. Rev. B*, 48(17):13115–13118, 1993.

[33] G. Kresse and J. Furthmüller. Efficient iterative schemes for ab-initio total-energy calculations using a plane-wave basis set. *Physical Review B*, 54(16):11169–11186, 1996.

[34] G. Kresse and D. Joubert. From ultrasoft pseudopotentials to the projector augmented-wave method. *Physical Review B*, 59(3):1758–1775, 1999.

[35] S. L. Dudarev, G. A. Botton, S.Y. Savrasov, C.J. Humphreys, and A.P. Sutton. Electron-energy-loss spectra and the structural stability of nickel oxide: An LSDA + U study. *Physical Review B*, 57(3):1505–1509, 1998.

[36] J. Bardeen, L. N. Cooper, and J. R. Schrieffer. Theory of superconductivity. *Physical Review*, 108(5):1175–1204, 1957.

[37] M. Tinkham. *Introduction to Superconductivity.* Robert E. Krieger Publishing Co., 1975.

[38] D. Larbalestier, A. Gurevich, D. M. Feldmann, and A. Polyanskii. High-T_c superconducting materials for electric power applications. *Nature*, 414(6861):368–377, 2001.

[39] J. D. Jorgensen, B. W. Veal, A. P. Paulikas, L. J. Nowicki, G. W. Crabtree, H. Claus, and W. K. Kwok. Structural properties of oxygen-deficient $YBa_2Cu_3O_{7-x}$. *Physical Review B*, 41(4):1863–1877, 1990.

[40] J. P. Attfield. Chemistry and high temperature superconductivity. *Journal of Materials Chemistry*, 21(13):4756–4764, 2011.

[41] S. N. Putilin, E. V. Antipov, O. Chmaissem, and M. Marezio. Superconductivity at 94 K in $HgBa_2CuO_{4+\delta}$. *Nature*, 362(6417):226–228, 1993.

[42] N. Nücker, H. Romberg, X. X. Xi, J. Fink, B. Gegenheimer, and Z. X. Zhao. Symmetry of holes in high-T_c superconductors. *Phys. Rev. B*, 39(10):6619–6629, 1989.

[43] N. Nücker, E. Pellegrin, P. Schweiss, J. Fink, S. L. Molodtsov, C. T. Simmons, G. Kaindl, W. Frentrup, A. Erb, and G. Müller-Vogt. Site-specific and doping-dependent electronic structure of $YBa_2Cu_3O_x$ probed by O 1s and Cu 2p x-ray-absorption spectroscopy. *Phys. Rev. B*, 51(13):8529–8542, 1995.

[44] G. Van Tendeloo, H. W. Zandbergen, and S. Amelinckx. Electron diffraction and electron-microscopic study of Ba-Y-Cu-O superconducting materials. *Solid State Communications*, 63(5):389–393, 1987.

[45] G. Van Tendeloo and S. Amelinckx. Defect structure of superconducting $YBa_2Cu_3O_7$. *Journal of Electron Microscopy Technique*, 8(3):285–295, 1988.

[46] J. C. Barry. Oxygen ordering and twinning in $YBa_2Cu_3O_{7-x}$. *Journal of Electron Microscopy Technique*, 8(3):325–337, 1988.

[47] Y. M. Zhu, M. Suenaga, and Y. W. Xu. Tem studies on twin boundary in $YBa_2Cu_3O_7$ and $YBa_2(Cu_{0.98}Zn_{0.02})_3O_7$. *Journal of Materials Research*, 5(7):1380–1387, 1990.

[48] R. Guzman, J. Gazquez, V. Rouco, A. Palau, C. Magen, M. Varela, J. Arbiol, X. Obradors, and T. Puig. Strain-driven broken twin boundary coherence in $YBa_2Cu_3O_{7-\delta}$ nanocomposite thin films. *Applied Physics Letters*, 102(8):81906, 2013.

[49] L. S. Chumbley, J. D. Verhoeven, M. R. Kim, A. L. Cornelius, and M. J. Kramer. Measurement and correlation of optical and TEM twins in $YBa_2Cu_3O_{7-x}$. *IEEE Transactions on Magnetics*, 25(2):2337–2340, 1989.

[50] S. K. Streiffer, E. M. Zielinski, B. M. Lairson, and J. C. Bravman. Thickness dependence of the twin density in $YBa_2Cu_3O_{7-x}$ thin-films sputtered onto MgO substrates. *Applied Physics Letters*, 58(19):2171–2173, 1991.

[51] J. Gutiérrez, A. Llordés, J. Gázquez, M. Gibert, N. Romá, S. Ricart, A. Pomar, F. Sandiumenge, N. Mestres, T. Puig, and X. Obradors. Strong isotropic flux pinning in solution-derived $YBa_2Cu_3O_{7-x}$ nanocomposite superconductor films. *Nature Materials*, 6(5):367–373, 2007.

[52] A. Llordés, A. Palau, J. Gázquez, M. Coll, R. Vlad, A. Pomar, J. Arbiol, R. Guzmán, S. Ye, V. Rouco, F. Sandiumenge, S. Ricart, T. Puig, M. Varela, D. Chateigner, J. Vanacken, J. Gutiérrez, V. Moshchalkov, G. Deutscher, C. Magen, and X. Obradors. Nanoscale strain-induced pair suppression as a vortex-pinning mechanism in high-temperature superconductors. *Nature Materials*, 11(4):329–336, 2012.

[53] A. Palau, F. Valles, V. Rouco, M. Coll, Z. Li, C. Pop, B. Mundet, J. Gazquez, R. Guzman, J. Gutierrez, X. Obradors, and T. Puig. Dis-

entangling vortex pinning landscape in chemical solution deposited superconducting $YBa_2Cu_3O_{7-x}$ films and nanocomposites. *Superconductor Science and Technology*, 31(3), 2018.

[54] V. M. Pan, A. L. Kasatkin, V. L. Svetchnikov, and H. W. Zandbergen. Dislocation model of superconducting transport properties of YBCO thin films and single crystals. *Cryogenics*, 33(1):21–27, 1993.

[55] J. Mannhart, D. Anselmetti, J. G. Bednorz, Ch. Gerber, K. A. Muller, and D. G. Schlom. Pinning centres in $YBa_2Cu_3O_{7-\delta}$ films. *Superconductor Science and Technology*, 5(1S):S125, 1992.

[56] B. Dam, J. M. Huijbregtse, F. C. Klaassen, R. C F Van der Geest, G. Doornbos, J. H. Rector, A. M. Testa, S. Freisem, J. C. Martinez, B. Stáuble-Púmpin, and R. Griessen. Origin of high critical currents in $YBa_2Cu_3O_{7-\delta}$ superconducting thin films. *Nature*, 399(6375):439–442, 1999.

[57] L. Civale, A. D. Marwick, T. K. Worthington, M. A. Kirk, J. R. Thompson, L. Krusin-Elbaum, Y. Sun, J. R. Clem, and F. Holtzberg. Vortex confinement by columnar defects in $YBa_2Cu_3O_7$ crystals: Enhanced pinning at high fields and temperatures. *Phys. Rev. Lett.*, 67(5):648–651, 1991.

[58] Y. S. Jeong, S. Y. Lee, H. Kyoung Jang, I. Yang, S. Moon, and B. Oh. Surface modification of laser ablated YBCO target. *Applied Surface Science*, 109-110:424–427, 1997.

[59] J. M. Huijbregtse, B. Dam, R. C. F. van der Geest, F. C. Klaassen, R. Elberse, J. H. Rector, and R. Griessen. Natural strong pinning sites in laser-ablated $YBa_2Cu_3O_{7-\delta}$ thin films. *Phys. Rev. B*, 62(2):1338–1349, 2000.

[60] P. Abellán, F. Sandiumenge, M. J. Casanove, M. Gibert, A. Palau, T. Puig, and X. Obradors. Interaction between solution derived $BaZrO_3$ nanodot interfacial templates and $YBa_2Cu_3O_7$ films leading to enhanced critical currents. *Acta Materialia*, 59(5):2075–2082, 2011.

[61] M. Coll, R. Guzman, P. Garcés, J. Gázquez, V. Rouco, A. Palau, S. Ye, C. Magén, H. Suo, H. Castro, T. Puig, and X. Obradors. Size-controlled spontaneously segregated Ba_2YTaO_6 nanoparticles in $YBa_2Cu_3O_7$ nanocomposites obtained by chemical solution deposition. *Superconductor Science and Technology*, 27(4):44008, 2014.

[62] P. Cayado, K. De Keukeleere, A. Garzón, L. Perez-Mirabet, A. Meledin, J. De Roo, F. Vallés, B. Mundet, H. Rijckaert, G. Pollefeyt, M. Coll, S. Ricart, A. Palau, J. Gázquez, J. Ros, G. Van Tendeloo, I. Van Driessche, T. Puig, and X. Obradors. Epitaxial $YBa_2Cu_3O_{7-x}$ nanocomposite thin films from colloidal solutions. *Superconductor Science and Technology*, 28(12):124007, 2015.

[63] S. Engel, T. Thersleff, R. Hühne, L. Schultz, and B. Holzapfel. Enhanced flux pinning in $YBa_2Cu_3O_7$ layers by the formation of nanosized $BaHfO_3$ precipitates using the chemical deposition method. *Applied Physics Letters*, 90(10):102505, 2007.

[64] M. Miura, M. Yoshizumi, T. Izumi, and Y. Shiohara. Formation mechanism of $BaZrO_3$ nanoparticles in $Y_{1-x}Sm_xBa_2Cu_3O_y$-coated conductors derived from trifluoroacetate metal-organic deposition. *Superconductor Science and Technology*, 23(1):014013, 2010.

[65] M. Coll, S. Ye, V. Rouco, A. Palau, R. Guzman, J. Gazquez, J. Arbiol, H. Suo, T. Puig, and X. Obradors. Solution-derived $YBa_2Cu_3O_7$ nanocomposite films with a Ba_2YTaO_6 secondary phase for improved superconducting properties. *Superconductor Science and Technology*, 26(1), 2012.

[66] P. Cayado, M. Erbe, S. Kauffmann-Weiss, C. Bühler, A. Jung, J. Hänisch, and B. Holzapfel. Large critical current densities and pinning forces in CSD-grown superconducting $GdBa_2Cu_3O_{7-x}$-$BaHfO_3$ nanocomposite films. *Superconductor Science and Technology*, 30(9):94007, 2017.

[67] K. De Keukeleere, P. Cayado, A. Meledin, J. Valles, F.and De Roo, H. Rijckaert, G. Pollefeyt, E. Bruneel, A. Palau, M. Coll, S. Ricart, G. Van Tendeloo, T. Puig, X. Obradors, and I. Van Driessche. Superconducting $YBa_2Cu_3O_7$ Nanocomposites Using Preformed ZrO_2 Nanocrys-

tals: Growth Mechanisms and Vortex Pinning Properties. *Advanced Electronic Materials*, 2(10):1–9, 2016.

[68] E. Bartolomé, P. Cayado, E. Solano, C. Mocuta, S. Ricart, B. Mundet, J. Coll, M.and Gázquez, A. Meledin, G. Van Tendeloo, S. M. Valvidares, J. Herrero-Martín, P. Gargiani, E. Pellegrin, C. Magén, T. Puig, and X. Obradors. Hybrid $YBa_2Cu_3O_7$ Superconducting-Ferromagnetic Nanocomposite Thin Films Prepared from Colloidal Chemical Solutions. *Advanced Electronic Materials*, 3(7):1700037, 2017.

[69] X. Obradors, T. Puig, Z. Li, C. Pop, B. Mundet, N. Chamorro, F. Vallés, M. Coll, S. Ricart, B. Vallejo, F. Pino, A. Palau, J. Gázquez, J. Ros, and A. Usoskin. Epitaxial $YBa_2Cu_3O_{7-x}$ nanocomposite films and coated conductors from $BaMO_3$ ($M = Zr, Hf$) colloidal solutions. *Superconductor Science and Technology*, 31(4):044001, 2018.

[70] A. Gupta, R. Jagannathan, E. I Cooper, E. A. Giess, J. I. Landman, and B. W. Hussey. Superconducting oxide films with high transition temperature prepared from metal trifluoroacetate precursors. *Applied Physics Letters*, 52(24):2077–2079, 1988.

[71] F. F. Lange. Chemical Solution Routes to Single-Crystal Thin Films. *Science*, 273(5277):903–909, 1996.

[72] J. Gázquez, F. Sandiumenge, M. Coll, A. Pomar, N. Mestres, T. Puig, X. Obradors, Y. Kihn, M. J. Casanove, and C. Ballesteros. Precursor evolution and nucleation mechanism of $YBa_2Cu_3O_x$ films by TFA metal-organic decomposition. *Chemistry of Materials*, 18(26):6211–6219, 2006.

[73] X. Obradors, T. Puig, S. Ricart, M. Coll, J. Gázquez, A. Palau, and X. Granados. Growth, nanostructure and vortex pinning in superconducting $YBa_2Cu_3O_7$ thin films based on trifluoroacetate solutions. *Superconductor Science and Technology*, 25(12):123001, 2012.

[74] X. Obradors, T. Puig, A. Pomar, F. Sandiumenge, N. Mestres, M. Coll, A. Cavallaro, N. Romà, J. Gázquez, J. C. González, O. Castaño, J. Gutierrez, A. Palau, K. Zalamova, S. Morlens, A. Hassini, M. Gibert, S. Ricart, J. M. Moretó, S. Piñol, D. Isfort, and J. Bock. Progress towards

all-chemical superconducting $YBa_2Cu_3O_7$ coated conductors. *Superconductor Science and Technology*, 19(3):S13–S26, 2006.

[75] N. Roma, S. Morlens, S. Ricart, K. Zalamova, J. M. Moreto, A. Pomar, T. Puig, and X. Obradors. Acid anhydrides: A simple route to highly pure organometallic solutions for superconducting films. *Superconductor Science and Technology*, 19(6):521–527, 2006.

[76] I. Van Driessche, J. Feys, S. C. Hopkins, P. Lommens, X. Granados, B. A. Glowacki, S. Ricart, B. Holzapfel, M. Vilardell, A. Kirchner, and M. Bäcker. Chemical solution deposition using ink-jet printing for YBCO coated conductors. *Superconductor Science and Technology*, 25(6):065017, 2012.

[77] M. Vilardell, X. Granados, S. Ricart, I. Van Driessche, A. Palau, T. Puig, and X. Obradors. Flexible manufacturing of functional ceramic coatings by inkjet printing. *Thin Solid Films*, 548:489–497, 2013.

[78] A. Llordés. PhD thesis: Superconducting nanocomposite films grown by chemical solution deposition: synthesis, microstructure and properties. *Universitat Autónoma de Barcelona (UAB)*, 2010.

[79] N. F. Heinig, R. D. Redwing, J. E. Nordman, and D. C. Larbalestier. Strong to weak coupling transition in low misorientation angle thin film $YBa_2Cu_3O_{7-x}$ bicrystals. *Physical Review B - Condensed Matter and Materials Physics*, 60(2):1409–1417, 1999.

[80] G. Deutscher. Origin of weak-link behavior of grain boundaries in superconducting cuprates and pnictides. *Applied Physics Letters*, 96(12):122502, 2010.

[81] L. Opherden, M. Sieger, P. Pahlke, R. Huhne, L. Schultz, A. Meledin, G. Van Tendeloo, R. Nast, B. Holzapfel, M. Bianchetti, J. L. MacManus-Driscoll, and J. Hanisch. Large pinning forces and matching effects in $YBa_2Cu_3O_{7-\delta}$ thin films with $Ba_2Y(Nb/Ta)O_6$ nano-precipitates. *Scientific Reports*, 6:21188, 2016.

[82] P. Mele, R. Guzman, J. Gazquez, T. Puig, X. Obradors, S. Shrikant, Y. Yoshida, M. Mukaida, A. Ichinose, K. Matsumoto, and M. I. Adam.

High pinning performance of $YBa_2Cu_3O_{7-x}$ films added with Y_2O_3 nanoparticulate defects. *Supercond. Sci. Technol.*, 28(2):024002, 2105.

[83] R. Gazquez, J.and Guzman, R. Mishra, E. Bartolomé, J. Salafranca, C. Magén, M. Varela, M. Coll, A. Palau, S. M. Valvidares, P. Gargiani, E. Pellegrin, Javier H. M., S. J. Pennycook, S. T. Pantelides, T. Puig, and X. Obradors. Emerging Diluted Ferromagnetism in High-T_C Superconductors Driven by Point Defect Clusters. *Advanced Science*, 3(6):150029, 2016.

[84] G. Deutscher and P. Degennes. A spatial interpretation of emerging superconductivity in lightly doped cuprates. *Comptes Rendus Physique*, 8(7-8):937–941, 2007.

[85] V. Rouco, A. Palau, R. Guzman, J. Gazquez, M. Coll, X. Obradors, and T. Puig. Role of twin boundaries on vortex pinning of CSD YBCO nanocomposites. *Superconductor Science and Technology*, 27(12):125009, 2014.

[86] To be published.

[87] A. Meledin, S. Turner, P. Cayado, B. Mundet, E. Solano, S. Ricart, J. Ros, T. Puig, X. Obradors, and G. Van Tendeloo. Unique nanostructural features in Fe, Mn-doped YBCO thin films. *Superconductor Science and Technology*, 29(12):125009, 2016.

[88] S. R. Foltyn, L. Civale, J. L. Macmanus-Driscoll, Q. X. Jia, B. Maiorov, H. Wang, and M. Maley. Materials science challenges for high-temperature superconducting wire. *Nature Materials*, 6(9):631–642, 2007.

[89] J. D. Jorgensen, B. W. Veal, W. K. Kwok, G. W. Crabtree, A. Umezawa, L. J. Nowicki, and A. P. Paulikas. Structural and superconducting properties of orthorhombic and tetragonal $YBa_2Cu_3O_{7-x}$: The effect of oxygen stoichiometry and ordering on superconductivity. *Phys. Rev. B*, 36(10):5731–5734, 1987.

[90] J. M. Tranquada, S. M. Heald, A. R. Moodenbaugh, and Youwen Xu. Mixed valency, hole concentration, and T_C in $YBa_2Cu_3O_{6+x}$. *Physical Review B*, 38(13):8893–8899, 1988.

[91] J. D. Jorgensen, H. Shaked, D. G. Hinks, B. Dabrowski, B. W. Veal, A. P. Paulikas, L. J. Nowicki, G. W. Crabtree, W. K. Kwok, L. H. Nunez, and H. Claus. Oxygen vacancy ordering and superconductivity in $YBa_2Cu_3O_{7-x}$. *Physica C: Superconductivity*, 153-155(1):578–581, 1988.

[92] M. F. Chisholm, M. P. Luo, W.and Oxley, S. T. Pantelides, and H. N. Lee. Atomic-scale compensation phenomena at polar interfaces. *Phys. Rev. Lett.*, 105(19):197602, 2010.

[93] A. Schilling, M. Cantoni, J. D. Guo, and H. R. Ott. Superconductivity above 130 K in the Hg-Ba-Ca-Cu-O system. *Nature*, 363(6424):56, 1993.

[94] N. Gauquelin, D. G. Hawthorn, G. A. Sawatzky, R. X. Liang, D. A. Bonn, W. N. Hardy, and G. A. Botton. Atomic scale real-space mapping of holes in $YBa_2Cu_3O_{6+\delta}$. *Nature Communications*, 5:4275, 2014.

[95] N. D. Browning, J. Yuan, and L. M. Brown. Determination of the local oxygen stoichiometry in $YBa_2Cu_3O_{7-\delta}$ by electron energy loss spectroscopy in the scanning transmission electron microscope. *Physica C:Superconductivity*, 202(1-2):12–18, 1992.

[96] M. Varela, M. P. Oxley, W. Luo, J. Tao, M. Watanabe, A. R. Lupini, S. T. Pantelides, and S. J. Pennycook. Atomic-resolution imaging of oxidation states in manganites. *Phys. Rev. B*, 79(8):085117, 2009.

[97] M. Grioni, J. F. Van Acker, M. T. Czyayk, and J. C. Fuggle. Unoccupied electronic structure and core-hole effects in the x-ray-absorption spectra of Cu_2O. *Physical Review B*, 45(7):3309–3318, 1992.

[98] D. G. Hawthorn, K. M. Shen, J. Geck, D. C. Peets, H. Wadati, J. Okamoto, S. W. Huang, D. J. Huang, H. J. Lin, J. D. Denlinger, Ruixing Liang, D. A. Bonn, W. N. Hardy, and G. A. Sawatzky. Resonant elastic soft x-ray scattering in oxygen-ordered $YBa_2Cu_3O_{6+x}$. *Physical Review B*, 84(7):075125, 2011.

[99] M. L. Medarde. Structural, magnetic and electronic properties of perovskites (R = rare earth) Structural, magnetic and electronic properties

of $RNiO_3$ perovskites (R = rare earth). *J. Phys.: Condens. Matter*, 9(997):1679–1707, 1997.

[100] G. Catalan, R. M. Bowman, and J. M. Gregg. Metal-insulator transitions in $NdNiO_3$ thin films. *Physical Review B - Condensed Matter and Materials Physics*, 62(12):7892–7900, 2000.

[101] S. Catalano, M. Gibert, V. Bisogni, O. E. Peil, F. He, R. Sutarto, M. Viret, P. Zubko, R. Scherwitzl, A. Georges, G. A. Sawatzky, T. Schmitt, and J. M. Triscone. Electronic transitions in strained $SmNiO_3$ thin films. *APL Materials*, 2(11):116110, 2014.

[102] E. Breckenfeld, Z. Chen, A. R. Damodaran, and L. W. Martin. Effects of nonequilibrium growth, nonstoichiometry, and film orientation on the metal-to-insulator transition in $NdNiO_3$ thin films. *ACS Applied Materials and Interfaces*, 6(24):22436–22444, 2014.

[103] S. Catalano, M. Gibert, V. Bisogni, F. He, R. Sutarto, M. Viret, P. Zubko, R. Scherwitzl, G. A. Sawatzky, and J. Triscone. Tailoring the electronic transitions of $NdNiO_3$ films through $(111)_{pc}$ oriented interfaces. *APL Materials*, 3(6):062506, 2015.

[104] G. Catalan. Progress in perovskite nickelate research. *Phase Transitions*, 81(7-8):729–749, 2008.

[105] Z. Yang, C. Ko, and S. Ramanathan. Oxide Electronics Utilizing Ultrafast Metal-Insulator Transitions. *Annual Review of Materials Research*, 41(1):337–367, 2011.

[106] S. D. Ha and S. Ramanathan. Adaptive oxide electronics: A review. *Journal of Applied Physics*, 110(7):71101, 2011.

[107] S. D. Ha, U. Vetter, J. Shi, and S. Ramanathan. Electrostatic gating of metallic and insulating phases in $SmNiO_3$ ultrathin films. *Applied Physics Letters*, 102(18):183102, 2013.

[108] F. Conchon, A. Boulle, R. Guinebretiere, C. Girardot, S. Pignard, J. Kreisel, F. Weiss, E. Dooryheé, and J.-L. Hodeau. Effect of tensile

and compressive strains on the transport properties of $SmNiO_3$ layers epitaxially grown on (001) $SrTiO_3$ and $LaAlO_3$ substrates. *Applied Physics Letters*, 91(19):192110, 2007.

[109] A. S. Disa, D. P. Kumah, J. H. Ngai, E. D. Specht, D. A. Arena, F. J. Walker, and C. H. Ahn. Phase diagram of compressively strained nickelate thin films. *APL Materials*, 1(3):032110, 2013.

[110] X. Obradors, L. M. Paulius, M. B. Maple, J. B. Torrance, A. I. Nazzal, J. Fontcuberta, and X. Granados. Pressure dependence of the metal-insulator transition in the charge-transfer oxides $RNiO_3$ (R=Pr,Nd,$Nd_{0.7}La_{0.3}$). *Physical Review B*, 47(18):12353–12356, 1993.

[111] P. C. Canfield, J. D. Thompson, S. W. Cheong, and L. W. Rupp. Extraordinary pressure dependence of the metal-to-insulator transition in the charge-transfer compounds $NdNiO_3$ and $PrNiO_3$. *Physical Review B*, 47(18):12357–12360, 1993.

[112] J. L. García-Muñoz, J. Rodríguez-Carvajal, P. Lacorre, and J. B. Torrance. Neutron-diffraction study of $RNiO_3$ (R=La,Pr,Nd,Sm): Electronically induced structural changes across the metal-insulator transition. *Physical Review B*, 46(8):4414–4425, 1992.

[113] J. L. García-Muñoz, M. A.G. Aranda, J. A. Alonso, and M. J. Martínez-Lope. Structure and charge order in the antiferromagnetic band-insulating phase of NdNiO3. *Physical Review B - Condensed Matter and Materials Physics*, 79(13):134432, 2009.

[114] J W Matthews and A E Blakeslee. Defects in epitaxial multilayers: I. Misfit dislocations. *Journal of Crystal Growth*, 27:118–125, 1974.

[115] J W Matthews. Defects associated with the accommodation of misfit between crystals. *Journal of Vacuum Science and Technology*, 12(1):126–133, 1975.

[116] E. Detemple, Q. M. Ramasse, W. Sigle, G. Cristiani, H. U. Habermeier, B. Keimer, and P. A. Van Aken. Ruddlesden-Popper faults in $LaNiO_3/LaAlO_3$ superlattices. *Journal of Applied Physics*, 112(1):1–6, 2012.

[117] L. López-Conesa, J. M. Rebled, D. Pesquera, N. Dix, F. Sánchez, G. Herranz, J. Fontcuberta, C. Magén, M. J. Casanove, S. Estradé, F. Peiró, J. Kreisel, and M. Greenblatt. Evidence of a minority monoclinic $LaNiO_{2.5}$ phase in lanthanum nickelate thin films. *Phys. Chem. Chem. Phys.*, 19(13):9137–9142, 2017.

[118] F. Wrobel, A. F. Mark, G. Christiani, W. Sigle, H. U. Habermeier, P. A. van Aken, G. Logvenov, B. Keimer, and E. Benckiser. Comparative study of $LaNiO_3/LaAlO_3$ heterostructures grown by pulsed laser deposition and oxide molecular beam epitaxy. *Applied Physics Letters*, 110(4):041606, 2017.

[119] D.P. Kumah, A. Malashevich, A.S. Disa, D.A. Arena, F.J. Walker, S. Ismail-Beigi, and C.H. Ahn. Effect of surface termination on the electronic properties of $LaNiO_3$ films. *Physical Review Applied*, 2(5):054004, 2014.

[120] J. P. Ruf, P. D. C. King, V. B. Nascimento, D. G. Schlom, and K. M. Shen. Surface atomic structure of epitaxial $LaNiO_3$ thin films studied by in situ LEED-I(V). *Physical Review B*, 95(11):115418, 2017.

[121] G. Stone, C. Ophus, T. Birol, J. Ciston, C.-H. Lee, K. Wang, C. J. Fennie, D. G. Schlom, N. Alem, and V. Gopalan. Atomic scale imaging of competing polar states in a Ruddlesden-Popper layered oxide. *Nature Communications*, 7:12572, 2016.

[122] J. Ruppen, J. Teyssier, O. E. Peil, S. Catalano, M. Gibert, J. Mravlje, J. M. Triscone, A. Georges, and D. Van Der Marel. Optical spectroscopy and the nature of the insulating state of rare-earth nickelates. *Physical Review B*, 92(15):155145, 2015.

[123] J. Y. Zhang, H. Kim, E. Mikheev, A. J. Hauser, and S. Stemmer. Key role of lattice symmetry in the metal-insulator transition of $NdNiO_3$ films. *Scientific Reports*, 6:23652, 2016.

[124] D. P. Kumah, A. S. Disa, J. H. Ngai, H. Chen, A. Malashevich, J. W. Reiner, S. Ismail-Beigi, F. J. Walker, and C. H. Ahn. Tuning the structure of nickelates to achieve two-dimensional electron conduction. *Advanced Materials*, 26(12):1935–1940, 2014.

[125] J. Son, P. Moetakef, J. M. Lebeau, D. Ouellette, L. Balents, S. J. Allen, and S. Stemmer. Low-dimensional Mott material: Transport in ultrathin epitaxial $LaNiO_3$ films. *Applied Physics Letters*, 96(6):062114, 2010.

[126] A. J. Hauser, E. Mikheev, N. E. Moreno, J. Hwang, J. Y. Zhang, and S. Stemmer. Correlation between stoichiometry, strain, and metal-insulator transitions of $NdNiO_3$ films. *Applied Physics Letters*, 106(9):092104, 2015.

[127] J. Z. Sun, D. W. Abraham, R. A. Rao, and C. B. Eom. Thickness-dependent magnetotransport in ultrathin manganite films. *Applied Physics Letters*, 74(20):3017–3019, 1999.

[128] A. Tebano, C. Aruta, S. Sanna, P. G. Medaglia, G. Balestrino, A. A. Sidorenko, R. De Renzi, G. Ghiringhelli, L. Braicovich, V. Bisogni, and N. B. Brookes. Evidence of Orbital Reconstruction at Interfaces in Ultrathin $La_{0.67}Sr_{0.33}MnO_3$ Films. *Phys. Rev. Lett.*, 100(13):137401, 2008.

[129] M. Huijben, L. W. Martin, Y.-H. Chu, M. B. Holcomb, P. Yu, G. Rijnders, D. H. A. Blank, and R. Ramesh. Critical thickness and orbital ordering in ultrathin $La_{0.7}Sr_{0.3}MnO_3$ films. *Phys. Rev. B*, 78(9):094413, 2008.

[130] F. Sandiumenge, J. Santiso, Ll. Balcells, Z. Konstantinovic, J. Roqueta, A. Pomar, J. P. Espinós, and B. Martínez. Competing misfit relaxation mechanisms in epitaxial correlated oxides. *Physical Review Letters*, 110(10):107206, 2013.

[131] M. Bibes, Ll. Balcells, S. Valencia, J. Fontcuberta, M. Wojcik, E. Jedryka, and S. Nadolski. Nanoscale Multiphase Separation at $La_{2/3}Ca_{1/3}MnO_3/SrTiO_3$ Interfaces. *Phys. Rev. Lett.*, 87(6):067210, 2001.

[132] D. Pesquera, A. Barla, M. Wojcik, E. Jedryka, E. Bondino, F. Magnano, S. Nappini, D. Gutiérrez, G. Radaelli, G. Herranz, F. Sánchez, and J. Fontcuberta. Strain-Driven Orbital and Magnetic Orders and Phase Separation in Epitaxial Half-Doped Manganite Films for Tunneling Devices. *Physical Review Applied*, 6(3):034004, 2016.

[133] J. Garcia-Barriocanal, J. C. Cezar, F. Y. Bruno, P Thakur, N. B. Brookes, C. Utfeld, A. Rivera-Calzada, S. R. Giblin, J. W. Taylor, J. A. Duffy, S. B. Dugdale, T. Nakamura, K. Kodama, C. Leon, S. Okamoto, and J. Santamaria. Spin and orbital Ti magnetism at $LaMnO_3/SrTiO_3$ interfaces. *Nature Communications*, 1:82, 2010.

[134] A P Ramirez. Colossal magnetoresistance. *Journal of Physics: Condensed Matter*, 9(39):8171, 1997.

[135] G.H. Jonker and J.H. Van Santen. Ferromagnetic compounds of manganese with perovskite structure. *Physica*, 16(3):337 – 349, 1950.

[136] R. von Helmolt, J. Wecker, B. Holzapfel, L. Schultz, and K. Samwer. Giant negative magnetoresistance in perovskitelike $La_{2/3}Ba_{1/3}MnO_x$ ferromagnetic films. *Phys. Rev. Lett.*, 71(14):2331–2333, 1993.

[137] R. M. Kusters, J. Singleton, D. A. Keen, R. McGreevy, and W. Hayes. Magnetoresistance measurements on the magnetic semiconductor $Nd_{0.5}Pb_{0.5}MnO_3$. *Physica B: Physics of Condensed Matter*, 155(1-3):362–365, 1989.

[138] A. Szewczyk, M. Gutowska, and B. Dabrowski. Specific heat and phase diagram of heavily doped $La_{1-x}Sr_xMnO_3$ ($0.45 \leqslant x \leqslant 1.0$). *Phys. Rev. B*, 72(22):224429, 2005.

[139] J. Nogués and I. K. Schuller. Exchange bias. *Journal of Magnetism and Magnetic Materials*, 192(2):203–232, 1999.

[140] J.-L. Maurice, F. Pailloux, A. Barthélémy, O. Durand, D. Imhoff, R. Lyonnet, A. Rocher, and J.-P. Contour. Strain relaxation in the epitaxy of $La_2/3Sr_1/3MnO_3$ grown by pulsed-laser deposition on $SrTiO_3(001)$. *Philosophical Magazine*, 83(28):3201–3224, 2003.

[141] C. Zener. Interaction between the *d*-shells in the transition metals. ii. ferromagnetic compounds of manganese with perovskite structure. *Phys. Rev.*, 82(3):403–405, 1951.

[142] P. W. Anderson and H. Hasegawa. Considerations on double exchange. *Phys. Rev.*, 100(2):675–681, 1955.

[143] A. M. Glazer. The classification of tilted octahedra in perovskites. *Acta Cryst.*, 28(11):3384–3392, 1972.

[144] P. M. Woodward. Octahedral Tilting in Perovskites. *Acta Cryst. B*, 53(1):32–43, 1997.

[145] P. G. Radaelli, G. Iannone, M. Marezio, H. Y. Hwang, S. W. Cheong, J. D. Jorgensen, and D. N. Argyriou. Structural effects on the magnetic and transport properties of perovskite $A_{(1-x)}A_{(x)'}MnO_3$ (x=0.25, 0.30). *Physical Review B*, 56(13):8265–8276, 1997.

[146] D. Pesquera, G. Herranz, A. Barla, E. Pellegrin, F. Bondino, E. Magnano, F. Sánchez, and J. Fontcuberta. Surface symmetry-breaking and strain effects on orbital occupancy in transition metal perovskite epitaxial films. *Nature Communications*, 3:1189, 2012.

[147] X. Li, I. Lindfors-Vrejoiu, M. Ziese, and P. A. Gloter, A.and van Aken. Impact of interfacial coupling of oxygen octahedra on ferromagnetic order in $La_{0.7}Sr_{0.3}MnO_3/SrTiO_3$ heterostructures. *Scientific Reports*, 7:40068, 2017.

[148] P. R. Willmott, S. A. Pauli, R. Herger, C. M. Schlepütz, D. Martoccia, B. D. Patterson, B. Delley, R. Clarke, D. Kumah, C. Cionca, and Y. Yacoby. Structural basis for the conducting interface between $LaAlO_3$ and $SrTiO_3$. *Physical Review Letters*, 99(15):155502, 2007.

[149] R. Pentcheva and W. E. Pickett. Avoiding the polarization catastrophe in $LaAlO_3$ overlayers on $SrTiO_3(001)$ through polar distortion. *Physical Review Letters*, 102(10):107602, 2009.

[150] C. Cantoni, J. Gazquez, F. Miletto Granozio, M. P. Oxley, M. Varela, A. R. Lupini, S. J. Pennycook, C. Aruta, U. S. Di Uccio, P. Perna, and D. MacCariello. Electron transfer and ionic displacements at the origin of the 2D electron gas at the LAO/STO interface: Direct measurements with atomic-column spatial resolution. *Advanced Materials*, 24(29):3952–3957, 2012.

[151] J. Gazquez, M. Stengel, R. Mishra, M. Scigaj, M. Varela, M. A. Roldan, J. Fontcuberta, F. Sánchez, and G. Herranz. Competition between polar

and nonpolar lattice distortions in oxide quantum wells: New critical thickness at polar interfaces. *Phys. Rev. Lett.*, 119(10):106102, 2017.

[152] J. Zabaleta. PhD thesis: Growth and advanced characterization of solution-derived nanoscale $La_{0.7}Sr_{0.3}MnO_3$ heteroepitaxial systems. *Universitat Autónoma de Barcelona (UAB)*, 2012.

[153] M. Bibes, S. Valencia, Ll. Balcells, B. Martínez, J. Fontcuberta, M. Wojcik, S. Nadolski, and E. Jedryka. Charge trapping in optimally doped epitaxial manganite thin films. *Phys. Rev. B*, 66(13):134416, 2002.

[154] R. Peng, H. C. Xu, M. Xia, J. F. Zhao, X. Xie, D. F. Xu, B. P. Xie, and D. L. Feng. Tuning the dead-layer behavior of $La_{0.67}Sr_{0.33}MnO_3/SrTiO_3$ via interfacial engineering. *Applied Physics Letters*, 104(8):81606, 2014.

[155] V. Garcia, M. Bibes, A. Barthélémy, M. Bowen, E. Jacquet, J.-P. Contour, and A. Fert. Temperature dependence of the interfacial spin polarization of $La_{2/3}Sr_{1/3}MnO_3$. *Phys. Rev. B*, 69(5):052403, 2004.

[156] M. Bowen, M. Bibes, A. Barthélémy, J. P. Contour, A. Anane, Y. Lemaître, and A. Fert. Nearly total spin polarization in $La_2/3Sr_1/3MnO_3$ from tunneling experiments. *Applied Physics Letters*, 82(2):233–235, 2003.

[157] J. J. Kavich, M. P. Warusawithana, J. W. Freeland, P. Ryan, X. Zhai, R. H. Kodama, and J. N. Eckstein. Nanoscale suppression of magnetization at atomically assembled manganite interfaces: XMCD and XRMS measurements. *Phys. Rev. B*, 76(1):014410, 2007.

[158] Y. Feng, K. J. Jin, L. Gu, X. He, C. Ge, Q. Hua Zhang, M. He, Q. Lin Guo, Q. Wan, M. He, H. B. Lu, and G. Yang. Insulating phase at low temperature in ultrathin $La_{0.8}Sr_{0.2}MnO_3$ films. *Scientific Reports*, 6:22382, 2016.

[159] G. Matsumoto. Study of $(La_{1-x}Ca_x)MnO_3$. I. Magnetic structure of $LaMnO_3$. *Journal of the Physical Society of Japan*, 29(3):606–615, 1970.

[160] G. A. Botton, G. L'espérance, C. E. Gallerneault, and M. D. Ball. Volume fraction measurement of dispersoids in a thin foil by parallel energy-loss

spectroscopy: development and assessment of the technique. *Journal of Microscopy*, 180(3):217–229, 1995.

[161] E. J. Moon, P. V. Balachandran, B. J. Kirby, D. J. Keavney, R. J. Sichel-Tissot, C. M. Schlepütz, E. Karapetrova, X. M. Cheng, J. M. Rondinelli, and S. J. May. Effect of interfacial octahedral behavior in ultrathin manganite films. *Nano Letters*, 14(5):2509–2514, 2014.

[162] U. Aschauer and N. A. Spaldin. Competition and cooperation between antiferrodistortive and ferroelectric instabilities in the model perovskite $SrTiO_3$. *Journal of Physics: Condensed Matter*, 26(12):122203, 2014.

[163] S. Koohfar, A. S. Disa, M. S.J. Marshall, F. J. Walker, C. H. Ahn, and D. P. Kumah. Structural distortions at polar manganite interfaces. *Physical Review B*, 96(2):024108, 2017.

[164] H. Boschker, J. Verbeeck, R. Egoavil, S. Bals, G. Van Tendeloo, M. Huijben, E. P. Houwman, G. Koster, D. H A Blank, and G. Rijnders. Preventing the reconstruction of the polar discontinuity at oxide heterointerfaces. *Advanced Functional Materials*, 22(11):2235–2240, 2012.

Appendix A

Calculations of the density of strained areas

In chapter 2, we have shown how the density of strained areas, localized around the edges of the Y124 intergrowth defect, influence some of the superconducting parameters of YBCO. This annex contains a detailed explanation of how this parameter is calculated:

From the Z-contrast images of YBCO NC films, see Fig. A.1 (a-e), the partial dislocations surrounding the Y124 intergrowth defects can be approximated to the shape of a cylindrical disk, as shown in Fig. A.1 (f-g). Therefore, the volume of each dislocation V_i can be estimated from:

$$V_i = \pi \left(R_i + \delta/2\right)^2 \delta - \pi \left(R_i - \delta/2\right)^2 \delta = 2\pi R_i \delta^2 \tag{A.1}$$

where R_i is the radius of the Y124 intergrowth, which are considered to be centered at the image plane for simplification, and δ is the length of the strained region caused by the dislocation, which is roughly 0.8 nm as shown in Fig. A.1 (f). The volume density is calculated by dividing the volume of the total amount of n dislocations that are found in the Z-contrast image and the total volume of the YBCO seen in the image, which is calculated by multiplying the viewed YBCO area (Δ_x and Δ_y) by the observation depth (Δ_z), estimated to be around 20nm.

$$\rho_{dis} = \frac{\sum_i^n V_i}{\Delta_x \Delta_y \Delta_z} \tag{A.2}$$

In some cases, namely $\frac{(\Delta_z+\delta)}{2} > R > \frac{(\Delta_z-\delta)}{2}$ and $R > \frac{(\Delta_z+\delta)}{2}$, part of the dislocation is out of the observation range. Accordingly, this exterior part have to be subtracted from the dislocation volume. The exterior part can be estimated by using some trigonometric relations, see Fig.A.2 (a).

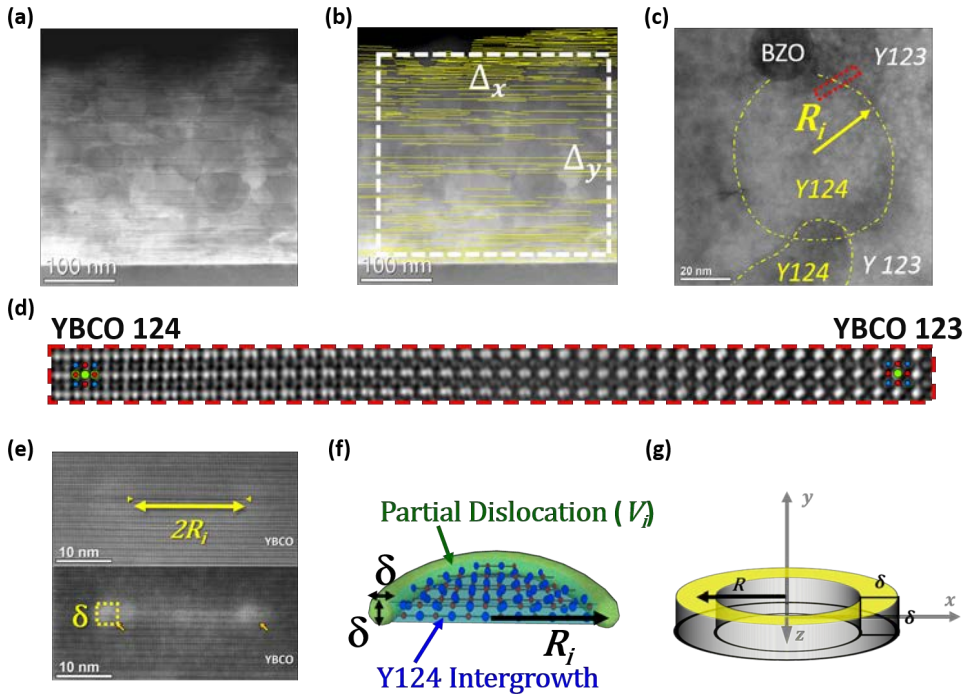

Figure A.1: (a) and (b) Cross-sectional LAADF images of a YBCO NC film. The Y124 intergrowths are marked with yellow stripes in (b) and the observed YBCO area ($\Delta_x \Delta_y$) is delimited with a white square. (c) Planar-view Z-contrast image of a YBCO NC film. The Y124 intergrowths' perimeter are highlighted in yellow. The red region is shown amplified in (d). The Y124 and Y123 phases are illustrated at each side of the boundary. (e) Z-contrast (above) and LAADF (below) images of an isolated 25 nm-long Y124 intergrowth. The yellow crosses and orange arrows point to the edge of the Y124 intergrowth defect. (f) GPA e_{yy} (above) and e_{xx} (below) deformation maps obtained from the Z-contrast image shown in (e). The strain field along the basal direction has a finite length-size of around $\delta = 0.8nm$. (g) Schematic view of the partial dislocation surrounding the Y124 intergrowth and its associated strain field geometry.

From Fig. A.2 (c), we obtain:

$$\cos\theta = \frac{\Delta_z}{2R} \tag{A.3}$$

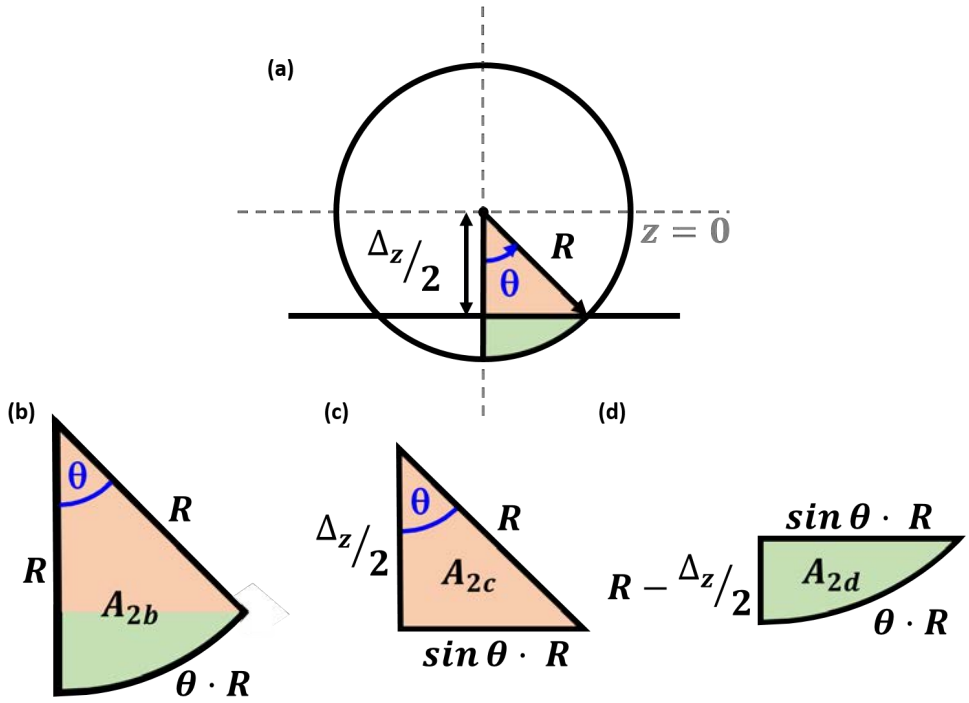

Figure A.2: Trigonometric relations given by the overlapping between a circle of radius R and the line $z = \Delta_z$. (a) Schematic planar-view. (b) Circular sector with radius R, angle θ and area A_{2b}. (c) Right triangle with angle θ and area A_{2c}. (d) Area A_{2d} resulting from the subtraction of A_{2c} from A_{2b}.

$$\sin\theta = \sin(\arccos(\Delta_z/2R) = \sqrt{1-(\Delta_z/2R)^2} \tag{A.4}$$

Now, using the equation A.4 in the calculation of the areas A_{2b}, A_{2c}, and A_{2d} of the geometric shapes shown in Fig. A.2 (b-d):

$$A_{2b}(\boldsymbol{R}) = \frac{\theta R^2}{2} = \frac{\arccos(\Delta_z/2R)R^2}{2} \tag{A.5}$$

$$A_{2c}(\boldsymbol{R}) = \frac{\sin(\theta)R\Delta_z/2}{2} = \frac{\sqrt{1-(\Delta_z/2R)^2}R\Delta_z}{4} \tag{A.6}$$

$$A_{2d}(\boldsymbol{R}) = A_{2b}(\boldsymbol{R}) - A_{2c}(\boldsymbol{R}) = \frac{\arccos(\Delta_z/2R)R^2}{2} - \frac{\sqrt{1-(\Delta_z/2R)^2}R\Delta_z}{4} \tag{A.7}$$

With these areas, we are able to calculate the volume of a dislocation V_i in each case.

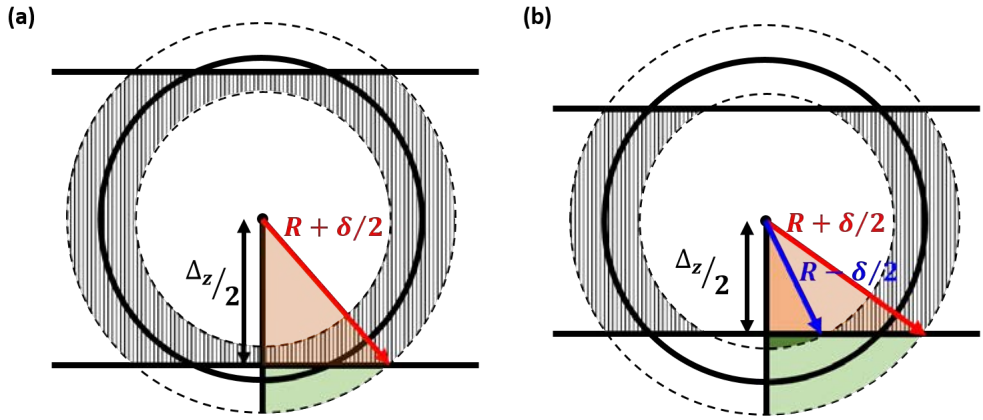

Figure A.3: Schematic planar-view of the circular partial dislocation and the observation depth limit (Δ_z), for the case of (a) $\frac{(\Delta_z+\delta)}{2} > R > \frac{(\Delta_z-\delta)}{2}$ and (b) $R > \frac{(\Delta_z+\delta)}{2}$.

For $\frac{(\Delta_z+\delta)}{2} > R > \frac{(\Delta_z-\delta)}{2}$ (see Fig.A.3 (a)), the volume of the striped region is:

$$\begin{aligned} V_i &= 2\pi R_i\delta^2 - 4\delta A_{2d}(\boldsymbol{R_i + \delta/2}) = \\ &= 2\pi R_i\delta^2 - \delta\left(R_i+\delta/2\right) \\ &\left[\left(R_i+\delta/2\right)2\arccos\left(\Delta_z/2(R_i+\delta/2)\right) - \Delta_z\sqrt{1-\left(\Delta_z/2(R_i+\delta/2)\right)^2}\right] \end{aligned} \tag{A.8}$$

For $R > \frac{(\Delta_z+\delta)}{2}$, see Fig. A.3 (b), the volume of the striped region is:

$$V_i = 2\pi R_i \delta^2 - 4\delta A_{2d}(\boldsymbol{R_i + \delta/2}) + 4\delta A_{2d}(\boldsymbol{R_i - \delta/2}) = \\ = 2\pi R_i \delta^2 - \delta\left(R_i + \delta/2\right) \\ \left[\left(R_i + \delta/2\right) 2\arccos\left(\Delta_z / 2(R_i + \delta/2)\right) - \Delta_z \sqrt{1 - \left(\Delta_z / 2(R_i + \delta/2)\right)^2}\right] + \delta\left(R_i - \delta/2\right) \\ \left[\left(R_i - \delta/2\right) 2\arccos\left(\Delta_z / 2(R_i - \delta/2)\right) - \Delta_z \sqrt{1 - \left(\Delta_z / 2(R_i - \delta/2)\right)^2}\right] \tag{A.9}$$

In summary:

$$V_i(R_i) = \\ = \begin{cases} 2\pi R_i \delta^2 & \text{for } R_i < \frac{(\Delta_z-\delta)}{2} \\ 2\pi R_i \delta^2 - \delta\left(R_i + \frac{\delta}{2}\right) \\ \left[\left(R_i + \frac{\delta}{2}\right) 2\arccos\left(\frac{\Delta_z}{2(R_i + \frac{\delta}{2})}\right) - \Delta_z \sqrt{1 - \left(\frac{\Delta_z}{2(R_i + \frac{\delta}{2})}\right)^2}\right] & \text{for } \frac{(\Delta_z+\delta)}{2} > R_i > \frac{(\Delta_z-\delta)}{2} \\ 2\pi R_i \delta^2 - \delta\left(R_i + \frac{\delta}{2}\right) \\ \left[\left(R_i + \frac{\delta}{2}\right) 2\arccos\left(\frac{\Delta_z}{2(R_i + \frac{\delta}{2})}\right) - \Delta_z \sqrt{1 - \left(\frac{\Delta_z}{2(R_i + \frac{\delta}{2})}\right)^2}\right] + \\ +\delta\left(R_i - \frac{\delta}{2}\right) \\ \left[\left(R_i - \frac{\delta}{2}\right) 2\arccos\left(\frac{\Delta_z}{2(R_i - \frac{\delta}{2})}\right) - \Delta_z \sqrt{1 - \left(\frac{\Delta_z}{2(R_i - \frac{\delta}{2})}\right)^2}\right] & \text{for } R_i > \frac{(\Delta_z+\delta)}{2} \end{cases} \tag{A.10}$$

The $V_i(\boldsymbol{R_i})$ dependence is plotted in Fig. A.4 for the three different ranges of R_i. Finally, the expression used for the calculation of ρ_{dis} is:

$$\rho_{dis} = \frac{\sum_i^{R_i < \frac{(\Delta_z-\delta)}{2}} V_i + \sum_i^{\frac{(\Delta_z+\delta)}{2} > R_i > \frac{(\Delta_z-\delta)}{2}} V_i + \sum_i^{R_i > \frac{(\Delta_z+\delta)}{2}} V_i}{\Delta_x \Delta_y \Delta_z} \tag{A.11}$$

where V_i corresponds to each case developed in equation (A.10).

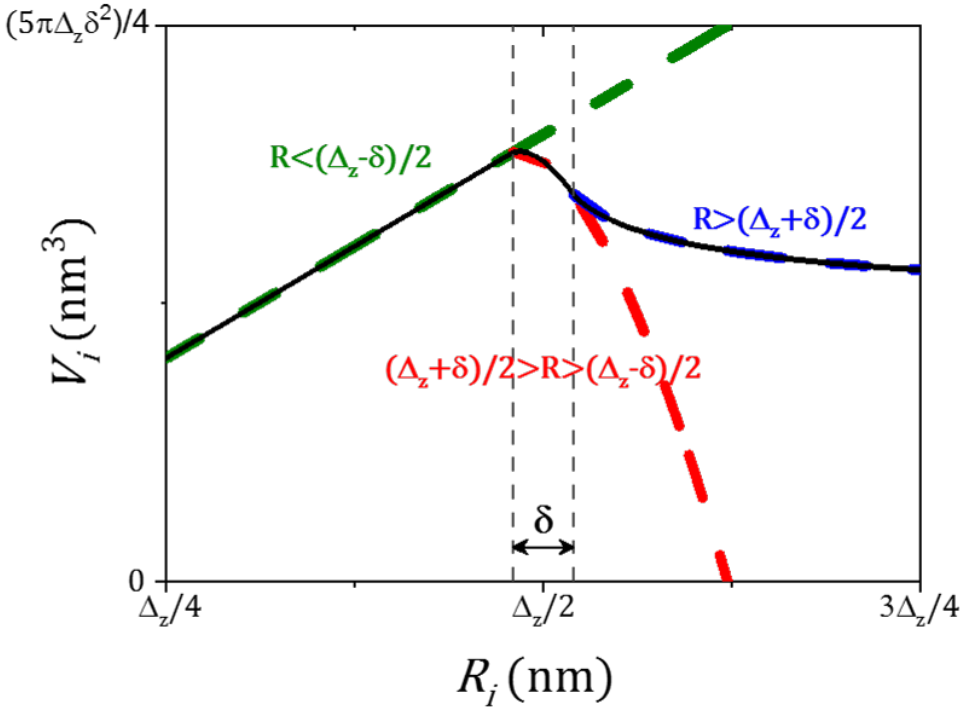

Figure A.4: Volume V_i as a function of the Y124 intergrowth radius R_i. Each dashed colored line correspond to the V_i, calculated by each different equation of A.10. The solid line corresponds to the real estimated V_i as a function of R_i.

Appendix B

List of Publications

Journal articles

- *"New insights onto the Y124 intergrowth"*. In preparation.
- *"Structural and physical properties of LSMO ultrathin films"*. In preparation.
- Z. Li, M. Coll, B. Mundet, N. Chamorro, F. Vallès, A. Palau, J. Gázquez, S. Ricart, T. Puig, X. Obradors. *"Control of nanostructure and pinning properties by fast processing solution deposited YBCO nanocomposite with preformed perovskite nanoparticles"*. Scientific Reports, submitted.
- B. Mundet, J. Jareño, J. Gázquez, M. Varela, X. Obradors and T. Puig. *"Defect landscape and electrical properties in solution-derived $LaNiO_3$ and $NdNiO_3$ epitaxial thin films"*. Phys. Rev. Materials, 2(6):063607, 2018.
- F. Vallès, A. Palau, V. Rouco, B. Mundet, X. Obradors and T. Puig. *"Angular flux creep contributions in $YBa_2Cu_3O_{7-\delta}$ nanocomposites from electrical transport measurements"*. Scientific Reports, 8(1):5924, 2018.
- X. Obradors, T. Puig, Z. Li, C. Pop, B. Mundet, N. Chamorro, F. Vallès, M. Coll, S. Ricart, B. Villarejo, F. Pino, A. Palau, J. Gázquez, J. Ros, and A. Usoskin. *"Epitaxial $YBa_2Cu_3O_{7-x}$ nanocomposite films and coated conductors from $BaMO_3$ (M=Zr,Hf) colloidal solutions"*. Superconductor science and technology, 31(4):044001, 2018
- A. Palau, F. Vallès, V. Rouco, M. Coll, Z. Li, C. Pop, B. Mundet, J. Gázquez, R. Guzman, J. Gutierrez, X. Obradors and T. Puig. *"Disentangling vortex pinning landscape in chemical solution deposition superconducting $YBa_2Cu_3O_{7-x}$ films and nanocomposites"*. Superconductor science and technology, 31(3):034004, 2018.

- R. Guzman, J. Gázquez, B. Mundet, M. Coll, X. Obradors, and T. Puig. *"Probing localized strain in solution-derived $YBa_2Cu_3O_{7-\delta}$ nanocomposite thin films"*. Phys. Rev. Materials, 1(2):024801, 2017.

- P. Cayado, B. Mundet, H. Eloussifi, F. Vallès, M. Coll, S. Ricart, J. Gázquez, A. Palau, P. Roura, J. Fargas, T. Puig and X. Obradors. *"Epitaxial superconducting $GdBa_2Cu_3O_{7-\delta}/Gd_2O_3$ nanocomposite thin fims from advanced low-fluorine solutions"*. Superconductor science and technology, 30(12):125010, 2017.

- E. Bartolomé, P. Cayado, E. Solano, C. Mocuta, S. Ricart, B. Mundet, M. Coll, J. Gázquez, A. Meledin, van Tendeloo, S. M. Valvidares, J. Herrero-MartÃn, P. Gargiani, E. Pellegrini, C. Magén, T. Puig, X. Obradors. *"Hybrid YBCO–MFe_2O_4 nanocomposite thin films prepared by Chemical Solution Deposition"*. Adv. Electron. Mater., 3(7):170037, 2017

- A. Meledin, S. Turner, P. Cayado, J. Gázquez, B. Mundet, T. Puig, X. Obradors and G. Van Tendeloo. *"Unique nanostructural features in Fe,Mn-doped YBCO thin films."*. Superconductor science and technology, 29(12):125009, 2016.

- E. Bartolomé, P. Cayado, E. Solano, S. Ricart, J. Gázquez, B. Mundet, M. Coll, T. Puig, X. Obradors, M. Valvidares, J. Herrero-MartÃn, P. Gargianid and E. Pellegrini. *"Magnetic stability against calcining of microwave synthesized $CoFe_2O_4$ nanoparticles"*. New Journal of Chem., 40(8):6890, 2016.

- P. Cayado, K. De Keukeleere, A. Garzón, L. Perez-Mirabet, A. Meledin, J. De Roo, F. Vallès, B. Mundet, H. Rijckaert, G. Pollefeyt, M. Coll, S. Ricart, A. Palau, J. Gázquez, J. Ros, G. Van Tendeloo, I. Van Driessche, T. Puig and X. Obradors. *"Epitaxial $YBa_2Cu_3O_{7-x}$ nanocomposite thin films from colloidal solutions"*. Superconductor science and technology, 28(12):124007, 2015.

Conference contributions

Oral presentations

- **Title:** *Characterization of strained $LaNiO_3$ and $NdNiO_3$ thin films by STEM*
  Authors: B. Mundet, J. Gázquez, M. Varela, Jareño, X. Obradors and T. Puig
  Name of the conference: European Material Research Society (e-MRS2018)
  City: Strasbourg, France
  Date: June 2018.

- **Title:** *Characterization of strained $LaNiO_3$ and $NdNiO_3$ thin films by STEM*
  Authors: B. Mundet, J. Gázquez, M. Varela, J. Jareño, X. Obradors and T. Puig
  Name of the conference: Material Research Society (MRS2018)
  City: Phoenix, Arizona, United States of America
  Date: April 2018.

- **Title:** *Atomic-scale probing of oxygen vacancies and associated distortions in YBCO*
  Authors: B. Mundet, J. Gázquez, R. Guzman, S. Hartman, G. Luo, R. Mishra, E. Bartolomé, M. Coll, A. Palau, T. Puig, X. Obradors
  Name of the conference: Material Research Society (MRS2018)
  City: Phoenix, Arizona, United States of America
  Date: April 2018.

- **Title:** *Probing oxygen vacancies and their associated distortions in $YBa_2Cu_3O_7$*
  Authors: B. Mundet, J. Gázquez, R. Guzman, R. Mishra, P.Cayado, Z. Li, M. Coll, T. Puig and X. Obradors
  Name of the conference: Microscopy at the Frontiers of Science (MFS2017)
  City: Zaragoza, Spain
  Date: September 2017

- **Title:** *The challenging pinning landscape in $YBa_2Cu_3O_7$ thin films*
  Authors: B. Mundet, J. Gázquez, R. Guzman, R. Mishra, P.Cayado, Z. Li, M. Coll, T. Puig and X. Obradors
  Name of the conference: European Conference on Applied Superconductivity (EUCAS 2017)
  City: Geneva, Switzerland
  Date: September 2017

Poster presentations

- **Title:** *Deep investigation of antiphase-boundary defects in rare-earth nickelates*
  Authors: B. Mundet, J. Jareño, J.Gázquez, J.C. González-Rosillo, X. Obradors and T. Puig
  Name of the conference: European Microscopy Congress (EMC2016)
  City: Lyon, France
  Date: September 2016

Workshops & Summer schools

- **Event**: Workshop Consolider-Nanoselect
  Type of contribution: Oral presentation **Title:** *Probing oxygen vacancies and their associated distortions in real space by means of STEM*
  Authors: B. Mundet, J. Gázquez, R. Guzman, R. Mishra, P.Cayado, Z. Li, M. Coll, T. Puig and X. Obradors
  Institution: ICMAB-CSIC
  City: Sant Feliu de Guíxols, Spain
  Date: July 2017

- **Event**: Workshop on vortex physics of strained nanocomposite films
  Type of contribution: Oral presentation **Title:** *Probing oxygen vacancies and their associated distortions in real space by means of STEM*
  Authors: B. Mundet, J. Gázquez, R. Guzman, R. Mishra, J. Salafranca, P. Cayado, Z. Li, M. Coll, F. Vallès, A. Palau, C. Magée, M. Varela, S.T. Pantelides, S.J. Pennycook, T. Puig and X. Obradors
  Institution: ICMAB-CSIC
  City: Bellaterra, Spain
  Date: September, 2018

- **Event**: Workshop Consolider-Nanoselect
  Type of contribution: Poster presentation
  Title: *Deep investigation of antiphase-boundary defects in rare-earth nickelates*
  Authors: B. Mundet, J. Jareño, J.Gázquez, J.C. González-Rosillo, X. Obradors and T. Puig
  Institution: ICMAB-CSIC
  City: Sant Feliu de Guíxols, Spain
  Date: July 2016

- **Event:** CCEM Summer School on Aberration-corrected Electron Microscopy
  Institution: McMaster University, Canadian Centre for Electron Microscopy
  City: Hamilton, Canada
  Dates: 1-5 June, 2015

- **Event:** Transmission electron Microscopy of nanomaterials (TEM-UCA)
  Institution: Universidad de Cádiz
  City: Puerto Real, Spain
  Dates: 14-18 July, 2014